UNIVERSITY OF SOUTHAMPTON

FACULTY OF ENGINEERING, SCIENCE AND MATHEMATICS
SCHOOL OF OCEAN AND EARTH SCIENCE

DEVELOPMENT AND DEPLOYMENT OF AN IN SITU SENSOR FOR SEAWATER pH BASED ON THE SPECTROPHOTOMETRIC METHOD

by

Victoire Rérolle

Thesis for the degree of Doctor of Philosophy

March 2013

A Grand Papa qui m'a fait partager,

parmi tant d'autres choses,

sa curiosité scientifique et sa passion de la mer.

UNIVERSITY OF SOUTHAMPTON

ABSTRACT

FACULTY OF ENGINEERING, SCIENCE AND MATHEMATICS
SCHOOL OF OCEAN AND EARTH SCIENCE

Doctor of Philosophy

DEVELOPMENT AND DEPLOYMENT OF AN IN SITU SENSOR FOR SEAWATER pH BASED ON THE SPECTROPHOTOMETRIC METHOD

by Victoire Rérolle

The uptake of anthropogenic CO_2 by the oceans since the on-set of the industrial revolution is considered to be a serious challenge to marine ecosystems due to ensuing carbonate chemistry changes (ocean acidification). Furthermore, the CO_2 uptake is reducing the ocean's capacity to absorb future CO_2 emissions. In order to follow the changes in the ocean's carbonate system, high-quality analytical measurements with good spatial and temporal resolution are necessary. The spectrophotometric pH technique is now widely used and capable of the required high-quality measurements. Smaller and more rugged instruments are nevertheless required for a more widespread *in situ* application to allow routine high resolution measurements even in the most remote regions. In this thesis, a simple micro-fluidic design integrated in a shipboard instrument featuring high accuracy and precision is presented as a key step toward a targeted pH micro-sensor system. The system is particularly adapted to shipboard deployment: high quality data was obtained over a period of more than a month during a shipboard deployment in northwest European shelf waters, and less than 30 mL of indicator was consumed. The system featured a short term precision of 0.001 pH (n=20) and an accuracy within the range of a certified Tris buffer (0.004 pH). The quality of the pH system measurements have been checked using various approaches: measurements of certified Tris buffer, measurement of certified seawater for DIC and TA, comparison of measured pH against calculated pH from pCO_2, DIC and TA during the cruise in northwest European shelf waters. All showed that our measurements were of high quality. The optical set up was robust and relatively small due to the use of an USB mini-spectrometer, a custom made polymeric flow cell and an LED light source. Finally, the pH data measured in the North West European Shelf Seas in summer 2011 is used to study the carbonate chemistry dynamics of the Shelf Seas surface water. A statistical approach is used to investigate which processes affect pH and their relative importance in explaining the observed pH variance along the ship's transect. The study highlighted the impact of temperature, biological activity and riverine inputs on the carbonate chemistry dynamics of the shelf sea surface water.

Table of Contents

List of figures 12

List of tables 14

Declaration of authorship 15

Acknowledgements 17

Chapter 1: Introduction 19

1.1. Atmospheric CO_2 levels 20

1.2. Marine carbonate chemistry 21

1.3. Factors influencing the carbonate system: 23

1.4. Impacts of atmospheric CO_2 emissions 25

1.5. Monitoring of the carbonate chemistry 27

1.6. Miniaturization of the spectrophotometric pH system 29

1.7. Thesis objectives 30

1.8. Thesis outline 31

Chapter 2: Methods 39

2.1. Chemical preparation 40

2.1.1. Indicator solutions 40

2.1.2. Acid buffers and basic solutions 40

2.2. Microfluidic flow cell: Fabrication method 41

2.3. Thermistors calibration 44

2.4. Replacement of the spectrophotometer with a photodiode 46

2.5. System control (LabVIEW program) 46

2.5.1. Control of the systems with the spectrophotometer 46

2.5.2. Control of the system with the photodiode 47

2.6. Indicator solution characterization 47

2.6.1 Determination of the extinction coefficients of the Thymol Blue indicator 47

2.6.2. Characterization of the meta-Cresol Purple indicator 48

2.7. Cruise deployment 48
2.7.1. RRS Discovery Cruise D366 48
2.7.2. RRS James Clark Ross Cruise JR271 48
2.8. Data processing and error analysis 49
2.8.1. Data processing of the measurement made with the spectrophotometer 49
2.8.2. Data processing of the measurement made with a photodiode 58
References 58
Chapter 3: Seawater pH measurements for ocean acidification observations: current approaches and future developments 59
3.1. Introduction 60
3.1.1. Impacts of atmospheric CO_2 emissions 60
3.1.2. Marine carbonate chemistry variables 60
3.2. Analytical techniques for seawater pH measurements 61
3.2.1. Definition of pH and pH scales 61
3.2.2. Potentiometric method 62
3.2.3. Luminescence method 64
3.2.4. Spectrophotometric method 64
3.3. Spectrophotometric pH systems 65
3.3.1. pH systems 65
3.3.2. Fluid propulsion 67
3.3.3. The absorption cell 68
3.3.4. Mixing of indicator with seawater sample 69
3.3.5. Light Source 69
3.3.6. The signal detector 70
3.3.7. Temperature 71
3.4. Sulphonephtalein indicator 71
3.5. Corrections 74
3.5.1. Baseline correction 74

3.5.2. Transparency correction 74
3.5.3. Corrections of pH to *in situ* conditions 74
3.5.4. Correction for indicator-induced pH perturbation: 74
3.6. Precision and accuracy 75
3.6.1. Precision 75
3.6.2. Accuracy 75
3.7. Microfluidic pH system 77
3.8. Conclusion and future directions 79
Acknowledgements 80
References 80
Chapter 4: Miniaturization of a spectrophotometric pH system 85
4.1. Introduction 86
4.2. Development of a colorimetric microfluidic pH sensor for autonomous seawater measurements 86
4.2.1. Instrument design 86
4.2.2. Thymol Blue indicator characterization 96
4.2.3. Correction for indicator induced pH perturbation 99
4.2.4. Deviations of absorbance behaviour from Beer's law 101
4.2.5. System precision and accuracy 104
4.2.6. Cruise data 105
4.3. Extension to mCP indicator: Results from the discrete sample pH system 106
4.3.1. Use of the mCP indicator with the same LEDs as Thymol Blue 106
4.3.2. mCP indicator characterization 109
4.3.3. Discrete system precision and accuracy 109
4.4. Replacement of the spectrometer with a photodiode 110
4.4.1. Quasi-simultaneous measurements at three wavelengths with a single photodiode 110
4.4.2. Precision of the photodiode set up 112
4.5. Conclusion 114

References 115
Chapter 5: Controls on pH in surface waters of Northwest European shelf seas 119
5.1. Introduction 120
5.2. Method 122
5.2.1. Cruise 122
5.2.2. Hydrography of the Northwest European Shelf seas 122
5.2.3 Data 124
5.2.4. Study regions (determination of the sub-regions) 126
5.2.5. Statistical approach 126
5.3. Results and discussion 127
5.3.1. Non-carbonate data distributions 127
5.3.2. Distribution and Quality of the carbonate data 129
5.3.3. Statistical results 134
5.3.4. pH dynamics 137
5.4. Conclusion 142
References 143
Chapter 6: Conclusion and Future work 147
6.1. Fluidics 149
6.1.1. Design of the static mixer 149
6.1.2. Thermistors in the flow cell 149
6.1.3. Implementation of the group pump 149
6.2. Optics 150
6.3. Inter-calibration (Bergen, Seattle) 151
References 151
Appendix 153
Appendix 1: Electronics 154
A1a. Valves driver circuit 154
A1b. Thermistors driver circuit 155

A1c. LED constant current driver circuit 156
Appendix 2: CAD Drawings 157
A2a. Underway Sampling Chamber 157
A2b. Valves Pot 160
A2c. Temperature Control Chamber.....163

List of figures

Figure 1.1: Schematic representation of the overall perturbation of the global carbon cycle caused by anthropogenic activities, averaged globally for the decade 2002–2011. 21

Figure 1.2: The concentrations of the dissolved carbonate species as a function of pH 23

Figure 1.3: Effect of various processes on DIC and TA (arrows). 25

Figure 1.4: Changes in the surface ocean carbonate system in response to an atmospheric CO_2 increase according to the IS92a scenario of the IPCC report 1995 26

Figure 1.5: Time series of atmospheric CO_2 at Mauna Loa 27

Figure 1.6: Positions of the floats that have delivered data within 30 days before the 04/07/2013. 29

Figure 2.1: Schematic of the pH system's microfluidic chip designed in Draftsight® (bottom view). 43

Figure 2.2: Calibration of the three thermistor against the ASL F250 thermometer in a temperature controlled water bath 45

Figure 3.1: Schematic diagram of an automated spectrophotometric pH system. 66

Figure 3.2 : Schematic of the microfluidic pH system. 77

Figure 3.3: Map of surface pH determined during the first week of cruise D366 79

Figure 4.1: A. Schematic of the pH system. 88

Figure 4.2: Taylor dispersion. 91

Figure 4.3: Simulation of the axial dispersion of the indicator slug 92

Figure 4.4: Thymol blue indicator and light source spectra. 93

Figure 4.5: Underway sampling chamber. 94

Figure 4.6: Temperature control chamber. 96

Figure 4.7: Correction for indicator induced pH perturbation. 100

Figure 4.8: Sensitivity analysis. 102

Figure 4.9: meta-Cresol Purple indicator and light source spectra. 106

Figure 4.10: Sensitivity analysis. 108

Figure 4.11: pH of a water column profile (CTD cast 42) measured during JR271. 110

Figure 4.12: Processing steps to obtain the three signals simultaneously from a single photodiode voltage output. 113

Figure 5.1: Map of the ship track during the cruise D366. 123

Figure 5.2: Bottom topography of the northwest European continental shelf. 124

Figure 5.3: The 11 study regions defined on geographical and water mass (T-S) characteristics. 126

Figure 5.4: $pH_{Tinsitu}$-$pH_{Tmeasurement}$ versus T_{insitu}-$T_{measurement}$. 129

Figure 5.5: Map of surface water pH_{tot} in European shelf waters determined during research cruise D366. 130
Figure 5.6: Sea surface pCO_2 and pH determined during the cruise D366.....130
Figure 5.7: A. Impact of different modelled processes on the pH-pCO_2 relationship and B. pH versus pCO_2 data from the D366 research cruise (blue dots) plotted over data from (Cullison-Gray et al., 2011) collected in Monterey Bay on the MBARI M0 buoy in summer 2007 (black dots). ...133
Figure 5.8: Two areas where pH and pCO_2 did not show an anti-correlation. 134
Figure 5.9: Impact of temperature on sea surface pH distribution. 138
Figure 5.10: Sea surface pH and chlorophyll concentration measured during the cruise D366....139
Figure 5.11: Impact of storm mixing on sea surface pH. 141
Figure 5.12: Impact of tide shelf mixing on sea surface pH.....142

List of tables

Table 1.1: Estimates of the analytical precision and accuracy of measurements of pH, TA, DIC and fCO_2. 28

Table 1.2: Estimated probable errors in the calculated parameters of the carbonate system using various input measurements. 28

Table 2.1: Composition of the acidic and basic solutions used for indicator characterization (weights for 1 liter of solution) 41

Table 2.2: Milling tools and settings used for the fabrication of the microfluidic flow cell. 42

Table 3.1: Figures of merit of spectrophotometric pH systems 67

Table 3.2: Equations for pH calculations (pK and extinction coefficient) reported in literature. 73

Table 4.1: Typical diffusivities for various tracers in water at room temperature 90

Table 4.2: Coefficients derived from multiple linear regression analysis, with results of statistical analysis. 98

Table 4.3: Precision and accuracy of certified Tris buffer measurements 104

Table 4.4: Extinction coefficient ratios of the mCP indicator on the pH system at 25°C and salinity 35. 109

Table 4.5: Precision and accuracy of DIC/TA CRMs measurements 109

Table 4.6: Comparison of the stability of the reference signal (in volt) for different On/Off configurations 111

Table 5.1: Mean values and standard deviations of S, T, TON, SiO_4 and Flc per regions. 128

Table 5.2: Results of the multi-linear regression analysis using S, T and Chl parameters with the underway data divided into 11 regions. 136

Table 5.3: Results of the stepwise multi-linear regression analysis using S, T and Chl, SiO_4 and NO_x parameters with the underway data divided into 11 regions. 136

Table 6.1: Specifications of the pH system. 148

Declaration of authorship

I, Victoire Rérolle, declare that this thesis entitled “Development and deployment of an in situ sensor for seawater pH based on the spectrophotometric method” and the work presented in it are my own, and have been generated by me as the result of my own original research.

I confirm that:

1. This work was done wholly or mainly while in candidature for a research degree at this University.

2. Where any part of this thesis has previously been submitted for a degree or any other qualification at this University or any other institution, this has been clearly stated.

3. Where I have consulted the published work of others, this is always clearly attributed.

4. Where I have quoted from the work of others, the source is always given. With the exception of such quotations, this thesis is entirely my own work.

5. I have acknowledged all main sources of help.

6. Where the thesis is based on work done by myself jointly with others, I have made clear exactly what was done by others and what I have contributed myself.

7. Parts of this work have been published as:

- Rérolle, V. M. C., C. F. A. Floquet, M. C. Mowlem, D. P. Connelly, E. P. Achterberg, and R. R. G. J. Bellerby (2012), Seawater-pH measurements for ocean-acidification observations, TrAC Trends in Analytical Chemistry, 40(0), 146-157.

- Rérolle, V., Floquet, C. F., Harris, A. J., Mowlem, M. C., Bellerby, R. R., and Achterberg, E. P.: Development of a colorimetric microfluidic pH sensor for autonomous seawater measurements, Analytica Chimica Acta, In Press, 2013.

Signed: .....

Date: .....

Graduate School of the National Oceanography Centre, Southampton

This PhD dissertation by *Victoire Rérolle* has been produced under the supervision of the following persons:

Supervisors

Prof. Eric Achterberg

Dr. Richard Bellerby

Dr. Cedric Floquet

Dr. Matt Mowlem

Chair of Advisory Panel

Dr. Richard Sanders

Acknowledgements

Firstly, I would like to thank my supervisors Prof. Eric Achterberg, Dr. Richard Bellerby, Dr. Cedric Floquet and Dr. Matt Mowlem for giving me the opportunity to work on this thesis and for their support and guidance throughout this study. A special thank to Eric, for his advises and permanent availability and to Cedric for encouraging me to take charge of my thesis and to learn new skills.

I am really grateful to Dr. Doug Connelly and Dr. Carla Sands for their great management of the SENSEnet project. This project gave me the chance to participate in many national and international conferences, visit several research leading institutes and meet great people.

Special thanks go to Andy Harris for the design and fabrication of all the electronics control boxes. I would also like to thank Dr. Ed Waugh for his help with software development and Rob Brown for mechanical assistance with the sampling chamber. I thank Dr. Dorothee Bakker and Gareth Lee (DIC, TA and pCO_2), Dr. Vassilis Kitidis and Dr. Iain Brown (pCO_2) and Tingting Shi (DOC) for data from D366. A special thank for the crew of the RRS Discovery and for the crew of the RRS James Clark Ross for their support during the cruises D366 and JR271 respectively.

Merci à Dr. Cynthia Dumousseaud for her help in carbonate chemistry, for teaching me how to prepare Tris buffer and for proof reading this thesis. Thank you to Matthew Humphreys for proof reading this thesis as well.

I would like to thank Dr. Marianna Ribas Ribas and Prof. Toby Tyrell for their help in the analysis of the pH data from the RRS Discovery cruise D366.

Thank you to the NOC Sensor group and to Dr. Emmanuelle Roberto-Reggianni for sharing experience and tips in sensor development.

This work was supported by SENSEnet, a Marie Curie Initial Training Network (ITN) funded by the European Commission Seventh Framework Programme, Contract Number PITN-GA-2009-237868. The Discovery D366 and James Clark Ross JCR271 cruises were funded by the Natural Environment Research Council as part of the UK Ocean Acidification (UKOA) Programme (grant no. NE/H017348/1).

Further acknowledgements go to the WUN Research Mobility Program, the UKOA research program and the Challenger Society for providing extra funds to attend conferences.

Finally I would like thank my amazing family and friends for their support throughout my studies.

Chapter 1: Introduction

1.1. Atmospheric CO_2 levels

Carbon dioxide (CO_2) is the most abundant greenhouse gas after water vapor in the earth's atmosphere. Atmospheric levels of CO_2 have increased from pre-industrial levels of 280 parts per million (ppmv) to nearly 392.53 at the end of 2012 (Dlugokencky and Tans) and are predicted to increase to 800 ppmv by the end of the century under the Intergovernmental Panel on Climate Change (IPCC) business-as-usual emission scenario (IS92a) (Intergovernmental Panel on Climate et al., 2007). This increase is caused by the anthropogenic release of carbon to the atmosphere from fossil fuel combustion, cement production and land use change. Anthropogenic emissions are added to a natural carbon cycle between the atmosphere, ocean, terrestrial biosphere and geologic reservoirs. Natural processes between these reservoirs occur on timescales from days to many millennia and even longer timescales for the geologic reservoirs (Archer et al., 2009).

The increasing concentration of CO_2 in the atmosphere has significant impact on the global climate. One of the most noticeable effects is global warming (NOAA National Climatic Data Center, 2012). However, only 46% of the CO_2 emitted between 1959 and 2011 is still present in the atmosphere, the remainder has been taken up by land vegetation (28%) and the oceans (27%) (Le Quéré et al., 2013) (Figure 1.1). Without these carbon sinks, climate change would likely be more pronounced.

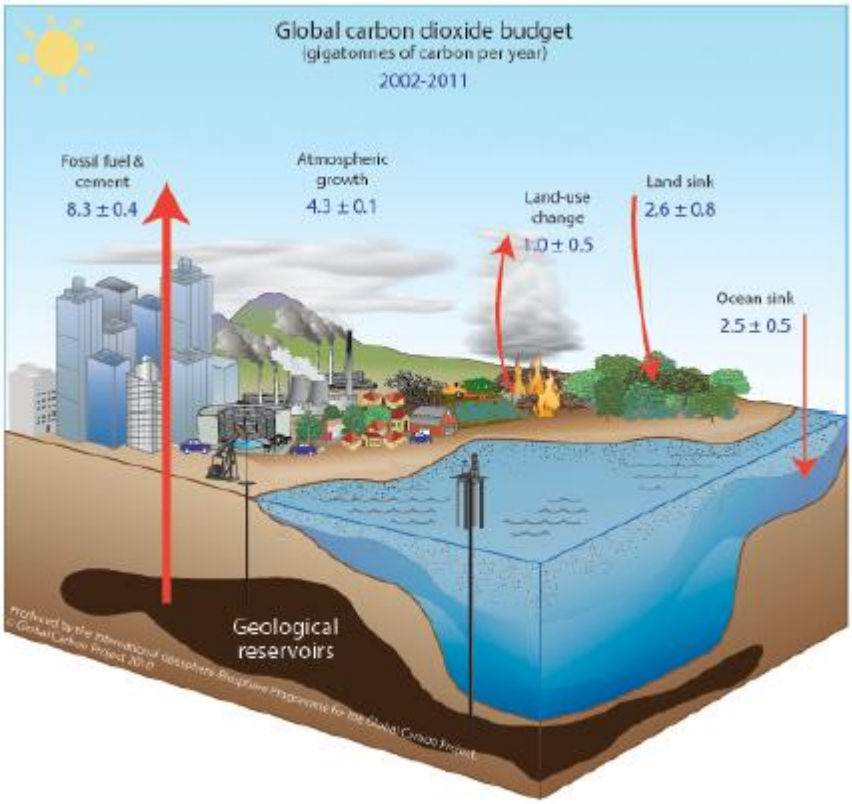

Figure 1.1: Schematic representation of the overall perturbation of the global carbon cycle caused by anthropogenic activities, averaged globally for the decade 2002–2011. The arrows represent emission from fossil fuel burning and cement production; emissions from deforestation and other land-use change; and the carbon sinks from the atmosphere to the ocean and land reservoirs. The annual growth of carbon dioxide in the atmosphere is also shown. All fluxes are in units of PgC yr−1, with uncertainties reported as ±1 sigma (68% confidence that the real value lies within the given interval) as described in the text. This Figure is an update of one prepared by the International Geosphere Biosphere Programme for the GCP, first presented in (Le Quéré, 2009). Taken from (Le Quéré et al., 2013).

The ocean's capacity to sequester CO_2 is dependent on the efficiencies of the biological (soft tissue and carbonate) and solubility carbon pumps (Volk and Hoffert, 1985). The oceanic carbonate system is affected by physical and biological processes leading to seasonal and spatial variations of the marine carbonate species.

1.2. Marine carbonate chemistry

When gaseous CO_2 dissolves in seawater, it becomes hydrated to form aqueous CO_2 (CO_{2aq}) (equation 1.1) which then reacts with water to form carbonic acid (H_2CO_3) (equation 1.2). The latter is difficult to distinguish from CO_{2aq}, therefore, the two species are usually considered as

one expressed here as H_2CO_3*. H_2CO_3* dissociates to HCO_3^- and CO_3^{2-} (equations 1.3 and 1.4). Both carbonate (CO_3^{2-}) and bicarbonate (HCO_3^-) ions can be used by marine organisms to form biogenic $CaCO_3$ (equation 1.5). These reactions and the equilibrium relationships between the concentrations of these various species are summarized as follows:

$CO_2gas \rightleftharpoons CO_2aq$ (1.1)

$CO_2aq+H2O \rightleftharpoons H_2CO_3$* (1.2) $K_1=[H_2CO_3*]/pCO_2$ (1.6)

$H_2CO_3* \rightleftharpoons HCO_3^-+H^+$ (1.3) $K_2=[H^+][HCO_3^-]/[CO_2*]$ (1.7)

$HCO_3^- \rightleftharpoons CO_3^{2-}+H^+$ (1.4) $K_3=[H^+][CO_3^{2-}]/[HCO_3^-]$ (1.8)

$Ca^{2+} + 2HCO_3^- \rightleftharpoons CaCO_3 + CO_2 + H_2O$ (1.5) $K_{sp}^{CaCO3}=[CO_3^{2-}][Ca^{2+}]$ (1.9)

Where pCO_2 is the partial pressure of CO_2 in the air.

When CO_2 dissolves in seawater, less than 1% remains as H_2CO_3*; most dissociate into HCO_3^- and CO_3^{2-}.

Four variables of the marine carbonate system can be directly determined in an accurate manner: total dissolved inorganic carbon (DIC), partial pressure of CO_2 (pCO_2), total alkalinity (TA) and pH.

- Total dissolved inorganic carbon : $DIC=[CO_{2aq}]+[H_2CO_3]+[HCO_3^-]+[CO_3^{2-}]$ (1.10)
- pCO_2 is defined in equation 1.6.
- Total alkalinity of seawater is defined as "the number of moles of hydrogen ions equivalent to the excess of proton acceptors (bases formed from weak acids with a dissociation constant $K \leq 10^{-4.5}$ at 25 °C and zero ionic strength) over proton donors (acids with $K > 10^{-4.5}$) in one kilogram of sample" (Dickson, 1981;Rakestraw, 1949). In seawater, the model of TA is defined as:

$TA= [HCO_3^-] +2[CO_3^{2-}] + [OH^-] - [H^+] + [B(OH)_4^-] + [HPO_4^{2-}] + 2[PO_4^{3-}] + [H_3SiO_4^-] + [NH_3] + [HS^-] - [HSO_4^-] - [HF] - [H_3PO_4]$ (1.11)

- The hydrogen ion concentration in sea water is usually reported as pH:

$pH = - \log [H^+]$ (1.12)

The pH of seawater is a master variable for the description of the thermodynamic state of the acid-base equilibria and is defined by three different scales. The pH definition, scales and measurements are reviewed in chapter 3.

Figure 1.2 shows how the concentration of the three inorganic carbon species varies as a function of pH for fixed DIC.

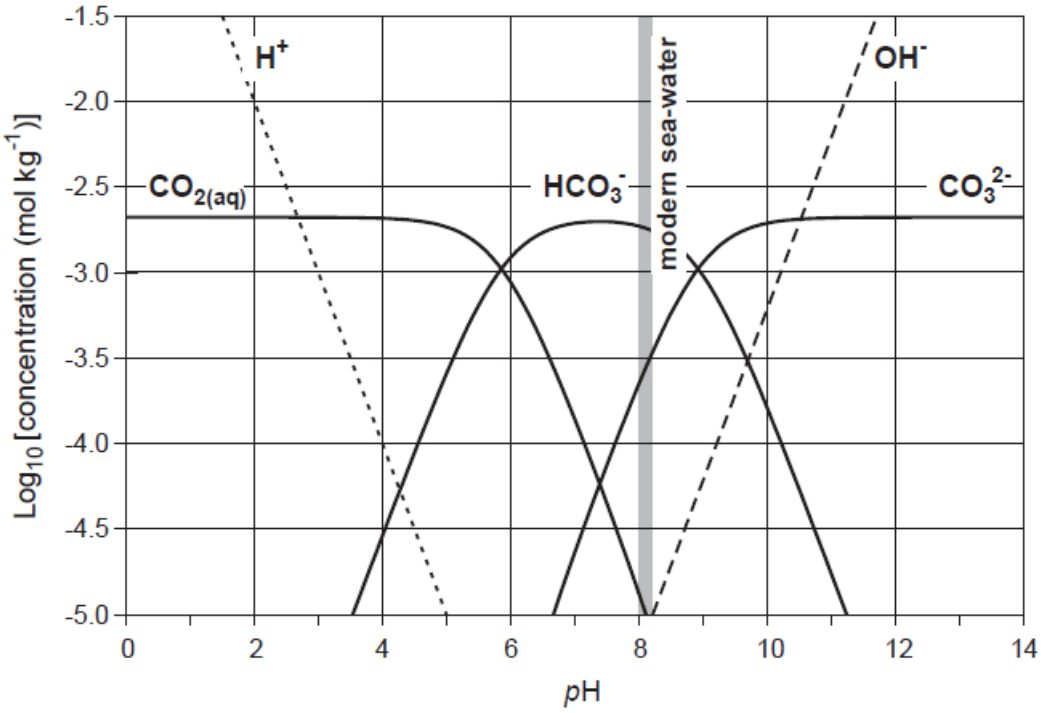

Figure 1.2: The concentrations of the dissolved carbonate species as a function of pH (referred to as the Bjerrum plot, (Zeebe and Wolf-Gladrow, 2001)): Dissolved carbon dioxide (CO_2(aq)), bicarbonate (HCO_3^-), carbonate ion (CO_3^{2-}), hydrogen ion (H^+), and hydroxyl ion (OH^-). At modern seawater pH, most of the dissolved inorganic carbon is in the form of bicarbonate. Note that in seawater, the relative proportions of CO_2, HCO_3^-, and CO_3^{2-} control the pH and not vice versa. Taken from (Ridgwell and Zeebe, 2005).

Mineral calcium carbonate occurs in the form of calcite, aragonite and high magnesium calcite. The degree of saturation (Ω) of calcite or aragonite in seawater is defined as the ion product of the concentrations of calcium and carbonate ion, at in situ temperature, salinity and pressure, divided by the stoichiometric solubility products of calcite or aragonite under in situ conditions. When Ω_{cal} or Ω_{arag}>1, seawater is supersaturated with respect to calcite and aragonite. The depth at which Ω_{cal}=1.0 occurs is called the equilibrium calcite saturation horizon (similar terminology can be applied for aragonite). But just below this, dissolution proceeds only extremely slowly. The depth at which dissolution impacts become noticeable is the calcite lysocline (Broecker, 2003).

1.3. Factors influencing the carbonate system:

Physical and biological processes have various effects on the carbonate system. DIC distribution is affected by photosynthesis, respiration, air-sea gas exchanges, mixing and the formation and dissolution of mineral calcium carbonate. Globally deep waters are enriched by respiration processes while it circulates along the deep conveyor belt from the Atlantic to Indian and Pacific (Broecker, 2003). Deep water upwelling and water masses mixing can thus strongly impact the

surface carbonate chemistry in certain areas. The Northeast Atlantic Ocean, the Nordic Seas (Greenland Sea, Norwegian Sea, and Iceland Sea), as well as the Barents Sea, are active areas for carbon sequestration from the atmosphere as well as for formation of intermediate to deep waters (Thomas et al., 2005). Mixing of water masses plays an important role in determining the properties of seawater in these areas (Holliday, 2003). Additionally, DIC fluctuates seasonally based on variations in primary production (photosynthesis) and respiration (soft tissue pump) but also due to mixing and in-gassing from the atmosphere (physical pump) (Skjelvan et al., 2008). Biomineralization by calcifying organisms such as coccolithophores and foraminifera (carbonate pump) also affects the DIC dynamics (Najjar, 1992). Despite the fact that deep water has 15% more DIC of surface water (Key et al., 2004), it has only about one-third the carbonate ion concentration of surface (Broecker and Peng, 1982). This is due to the fact that alkalinity and DIC are affected by these processes in different ways (see Figure 1.3). For example, remineralization of 1 mole of organic matter results in a $[CO_3^{2-}]$ decrease of 1.14 moles, whereas the dissolution of 1 mole $CaCO_3$ leads to a 1 mole increase in $[CO_3^{2-}]$. Similarly, $CaCO_3$ precipitation changes DIC and TA in a ratio 1:2 and drives an increase in ocean pCO_2. The seasonal succession of phytoplankton can therefore play an important role in determining the cycling of carbon. The interplay of the different processes and their impact on surface pH in coastal seas will be studied in more details in chapter 5.

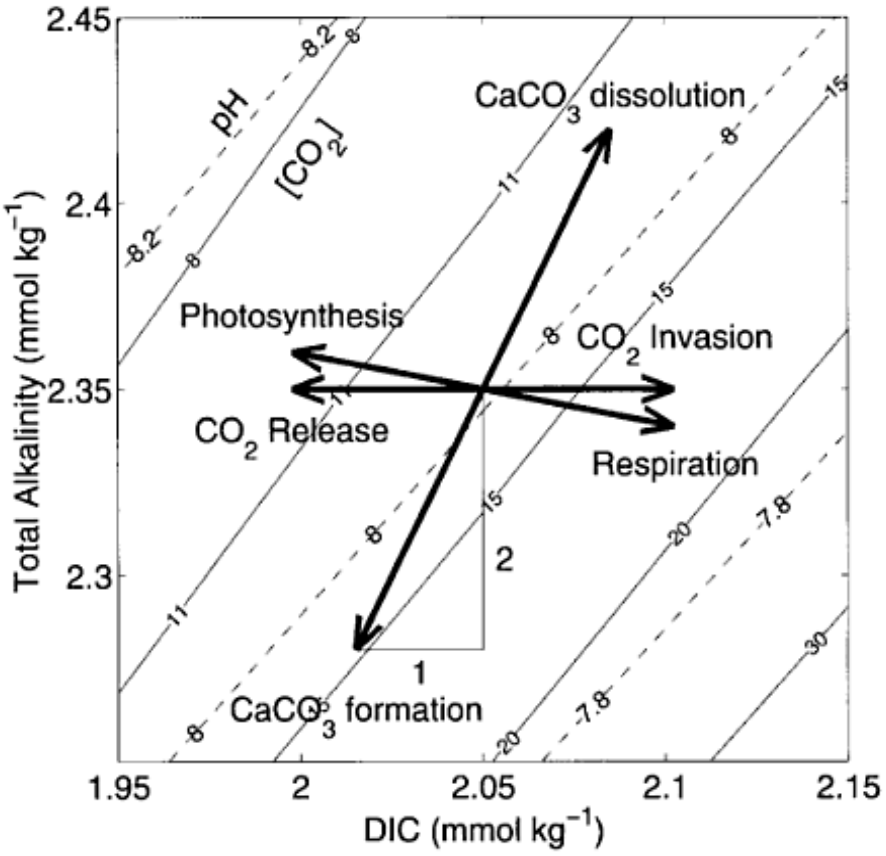

Figure 1.3: Effect of various processes on DIC and TA (arrows). Solid and dashed lines indicate levels of constant dissolved CO_2 (in µmol/kg) and pH, respectively, as a function of DIC and TA. $CaCO_3$ formation, for example, reduces DIC by one and TA by two units, therefore driving the system to higher CO_2 levels and lower pH. Invasion of atmospheric CO_2 into the ocean increases DIC, while release of CO_2 to the atmosphere has the opposite effect. TA stays constant in these two cases. Taken from (Zeebe and Wolf-Gladrow, 2001).

1.4. Impacts of atmospheric CO_2 emissions

In addition to these natural variations, the continuous increase in the anthropogenic CO_2 flux into the ocean since the industrial revolution has resulted in significant shifts of the carbonate system equilibriums, with a reduction in seawater pH (Figure 1.4) (González-Dávila, 2010;Dore et al., 2009;Byrne et al., 2010;Wolf-Gladrow et al., 1999).

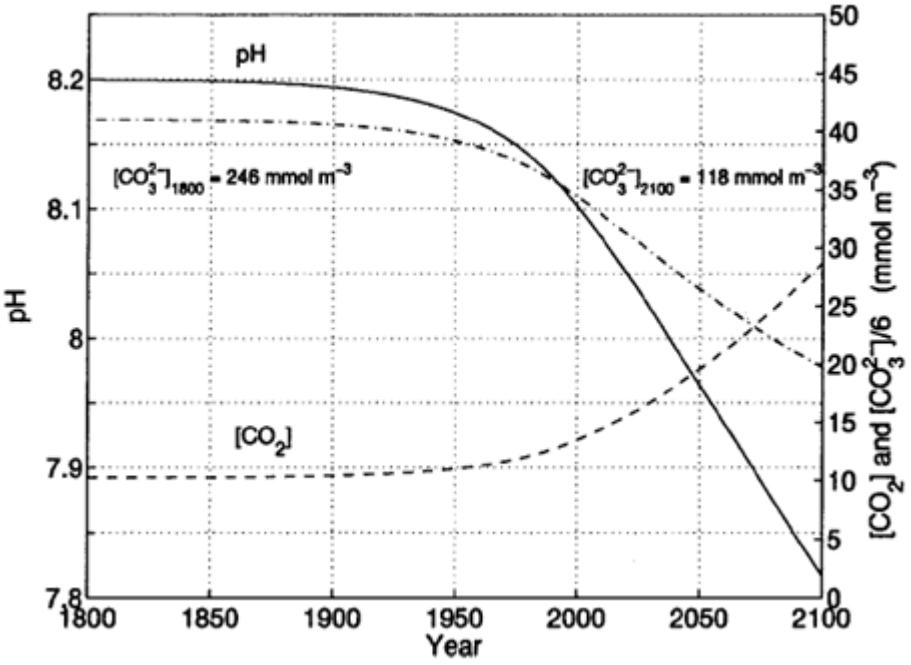

Figure 1.4: Changes in the surface ocean carbonate system in response to an atmospheric CO_2 increase according to the IS92a scenario of the IPCC report 1995 (approximated by a linear increase of CO_2 emissions from 6.3 Gt C yr^{-1} to 20 Gt C yr^{-1} in the year 2100): pH (solid line), CO_2 concentration (dashed line) and CO_3^{2-} concentration (dash dotted line; please note the different scales for $CO_2$and CO_3^{2-}). Taken from (Wolf-Gladrow et al., 1999).

Since the onset of the industrial revolution, average surface ocean pH has decreased by 0.1 pH units (Caldeira and Wickett, 2005), and currently the rate of decrease is 0.002 pH units per year (Figure 1.5) (González-Dávila, 2010;Dore et al., 2009;Byrne et al., 2010). This phenomenon is called ocean acidification and is a major topic in oceanographic research. Significant shifts in the carbonate system are a serious cause for concern for marine biodiversity and ecosystem functioning, and in particular for calcifying organisms (Doney, 2010). Indeed, the acid formed by dissolution of CO_2 lowers pH so that some CO_3^{2-} combines with H^+ to form HCO_3^-. Hence, addition of CO_2 decreases CO_3^{2-}. Ocean acidification is expected to decrease $CaCO_3$ saturation states and increase dissolution rates which will affects shell-forming calcareous marine organisms from plankton to benthic mollusks, echinoderms and corals. Indeed, coral calcification rate has already decreased compared to preindustrial era (Cooper et al., 2008) and many calcifiers exhibit reduced calcification and growth rates in laboratory experiments (Borowitzka and Larkum, 1986;Buddemeier, 2007;Kuffner et al., 2008;Gazeau et al., 2007;Shirayama and Thornton, 2005;Riebesell et al., 2000;Zondervan et al., 2002;Zondervan et al., 2001;Sciandra et al., 2003;Delille et al., 2005;Engel et al., 2005;Fabry et al., 2008;Guinotte and Fabry, 2008). But

calcification response to high CO_2 concentrations may vary between species (Langer et al., 2006;Iglesias-Rodriguez et al., 2008) and potential adaptation of organisms to long-term changes remains poorly understood.

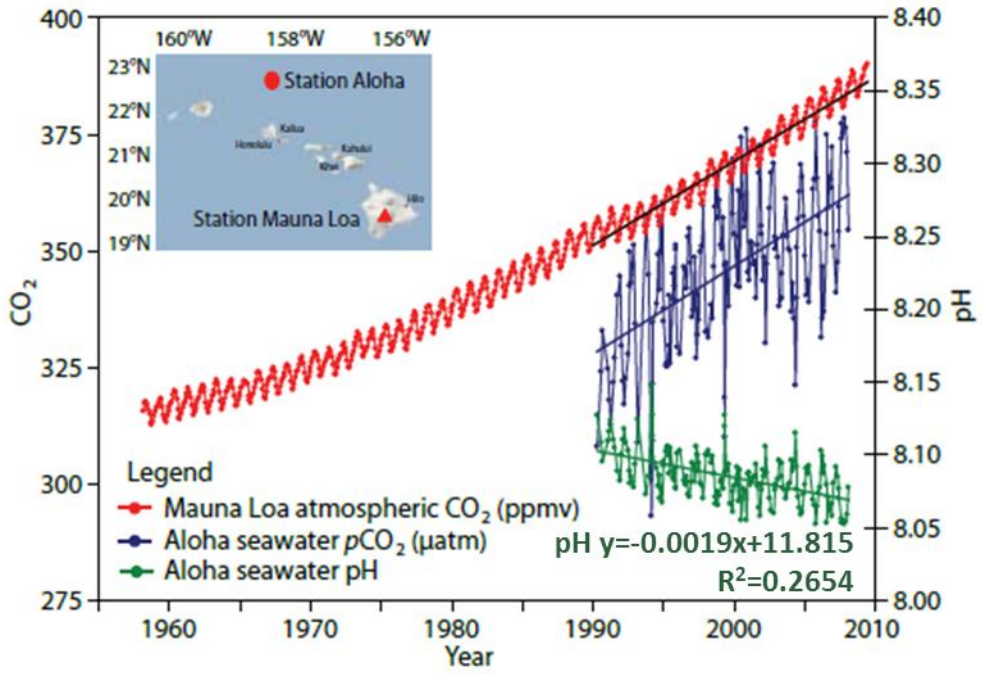

Figure 1.5: Time series of atmospheric CO_2 at Mauna Loa (in parts per million volume, ppmv; red), surface ocean pCO2 (µatm; blue) and surface ocean pH (green) at Ocean Station ALOHA in the subtropical North Pacific Ocean. Figure adapted from (Doney et al., 2009a).

The changes in the marine carbonate system also reduce the ocean's capacity to absorb future atmospheric CO_2 emissions (Sabine et al., 2004). This decline in the efficiency of the oceanic CO_2 sink contributes to an acceleration in the rate of atmospheric CO_2 increase. As a result, climate change due to carbon forcing is occurring faster than forecasted by models (Canadell et al., 2007).

1.5. Monitoring of the carbonate chemistry

High quality carbonate chemistry measurements are required in order to fully understand the dynamics of the oceanic carbonate system (Bellerby et al., 1993). If any two of the four carbonate system variables presented above (DIC, pCO_2, TA and pH) are determined, along with *in situ* temperature, salinity and macronutrients (nitrate, phosphate, silicate), it is possible to calculate the other two. As a result of measurement uncertainties, certain pairings are more accurate for the calculation of the carbonate system than others (Dickson, 2010;Dickson and Riley, 1979;Millero et al., 1993). Table 1.1 and 1.2 detail the uncertainties in the measured (Table 1.1)

and calculated (Table 1.2) parameters of the carbonate system due to experimental errors using various input measurements (Millero, 2007).

Table 1.1: Estimates of the analytical precision and accuracy of measurements of pH, TA, DIC and fCO_2. Taken from (Millero, 2007).

Analysis	Precision	Accuracy
pH (spectrophotometric)	0.0004	0.002
TA (potentiometric)	1 µmol.kg^{-1}	3 µmol.kg^{-1}
DIC (coulometric)	1 µmol.kg^{-1}	2 µmol.kg^{-1}
fCO_2 (infrared)	0.5 µatm	2 µatm

Table 1.2: Estimated probable errors in the calculated parameters of the carbonate system using various input measurements. Taken from (Millero, 2007).

Input	pH	TA (µmol.kg^{-1})	DIC (µmol.kg^{-1})	fCO_2 (µatm)
pH-TA			±3.8	±2.1
pH-DIC		±2.7		±1.8
pH-fCO_2		±21	±18	
fCO_2-DIC	±0.0025	±3.4		
fCO_2-TA	±0.0026		±3.2	
TA-DIC	±0.0062			±5.7

To date the determination of DIC and TA has been preferred due to readily available instrumentation. However, because of uncertainties in the equilibrium constant K_2, the use of the pair DIC & TA results in the largest uncertainties in calculated pH and pCO_2 (Millero, 2007). Additionally, TA can be difficult to interpret in ocean acidification experiments and coastal areas (Dickson, 2010). pH and DIC are therefore now considered to be the optimal pair for the description of the CO_2 system. Nevertheless, inconsistencies have been observed when using different pairs of variables to determine the carbonate system (Hoppe et al., 2012). The sources of these inconsistencies are uncertain but may be due to inaccuracies in the analytical measurements, inaccuracies in the thermodynamic constants used for the calculations, or the presence of dissolved organic acid/base compounds which are not taken into account in the estimation of alkalinity from titration using the Gran method (Kim and Lee, 2009). This highlights the need to measure more than two carbonate chemistry variables. A better accuracy of the carbonate parameters can be obtained by direct measurements than by calculation. The choice of parameters to measure should then reflect the process of interest (Dickson & Riley 1978). For example, the pair of parameters pH & TA is recommended to study calcification processes (Hoppe et al., 2012) since TA is twice as sensitive to changes in the carbonate ion concentration as is DIC (see figure 1.3). DIC on the contrary will be more sensitive to photosynthesis and gas addition

than TA. pCO_2 is generally used to study air-sea gas exchanges: pCO_2 instruments readily measure seawater and atmospheric pCO_2 levels. The pH of a solution indicates the thermodynamic equilibrium of all acid-base species in that solution. pH is therefore used to study the effect of ocean acidification on biogeochemical processes.

With the spectrophotometric pH technique, pH can be measured with a sufficiently high precision and accuracy to allow comparison with the other thermodynamic variables that characterize the oceanic carbonate system (Cullison-Gray et al., 2011). Thanks to recent technological improvements in optical devices (e.g. Mini-spectrophotometers, photodiodes, LEDs), spectrophotometric pH instruments can be easily miniaturized while providing high quality measurements.

The precision of seawater pH measurements needs to be better than 0.002 pH units in order to allow detection of the average annual surface ocean pH decrease (González-Dávila, 2010;Dore et al., 2009;Byrne et al., 2010).

1.6. Miniaturization of the spectrophotometric pH system

The spatial and temporal resolution of oceanic carbonate system measurements is currently still insufficient, despite important efforts to improve analytical methods, develop new instruments and coordinate international monitoring activities (Doney et al., 2009b).

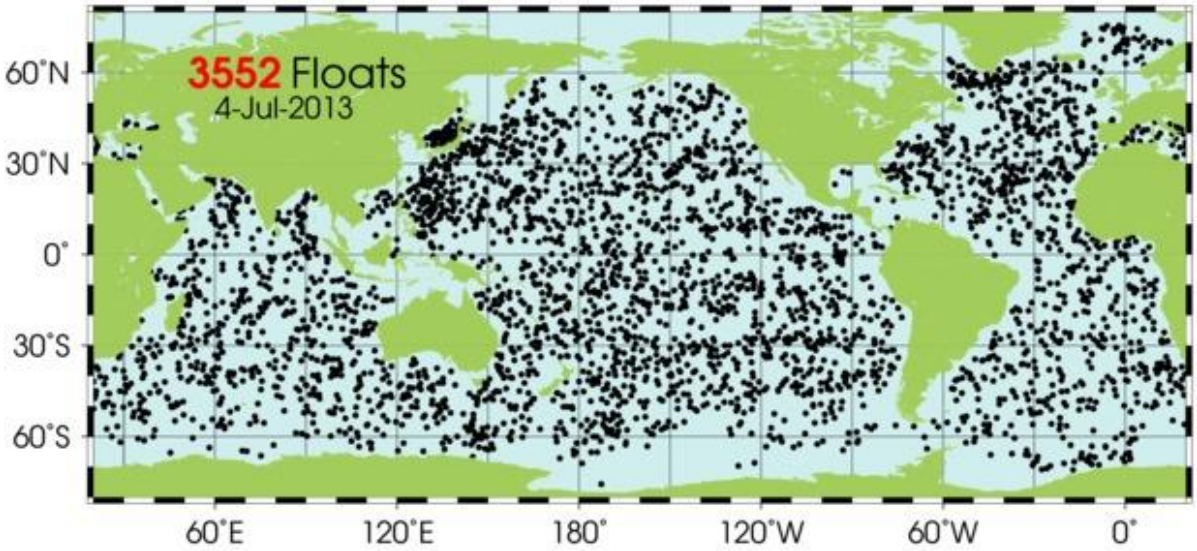

Figure 1.6: Positions of the floats that have delivered data within 30 days before the 04/07/2013. http://www.argo.ucsd.edu/About_Argo.html

Figure 1.6 shows the positions of all Argo floats, free-drifting profiling floats that measure at least the temperature and salinity of the upper 2000 m of the ocean, deployed in September 2012.

Clearly, the deployment of carbonate sensors on such a platform would provide an outstanding global set of near real-time data. However, routine high-resolution oceanic measurements using moorings, drifters, or profiling floats are currently limited to temperature, salinity, oxygen and recently nutrients (Johnson et al., 2009). Instruments measuring carbonate parameters need to be automated, miniaturized and ruggedized to be deployed on these *in situ* platforms. Widespread use, particularly on small platforms as part of a global observing system, will only be possible with low-cost sensors featuring low power and resource (e.g. reagent) consumption. Miniaturized pH systems with high analytical precision and accuracy would be optimal for deployment on oceanic moorings and small vehicles to allow large scale monitoring of ocean acidification.

Miniaturization of analytical systems has yielded a reduction in sample, reagent and power consumption. A key advance in wet chemical sensors has been the implementation of microfluidic Lab-on-Chip platforms. Microfluidic technology has a range of applications in clinical, biological and chemical analysis of small volume samples (Dittrich et al., 2006). The technology is of great interest for environmental monitoring, particularly in aquatic systems (Prien, 2007).

The widely-used spectrophotometric pH technique is capable of the high-quality measurements required to study the changes in the marine carbonate system (Rérolle et al., 2012). High precision and accuracy pH measurements using the spectrophotometric technique have been demonstrated at sea for surface water measurements on research vessels (Assmann et al., 2011;Bellerby et al., 2002;Bellerby et al., 1995;Mosley et al., 2004;DelValls, 1999;Ohline et al., 2007;Tapp et al., 2000;Wang et al., 2007) and more recently, successful *in situ* deployments have been reported (Kaltenbacher et al., 2000;Liu et al., 2006;Martz et al., 2003;Nakano et al., 2006;Seidel et al., 2008). This simple and high precision technique is a prime candidate for miniaturization and would address the urgent need for ruggedized autonomous *in situ* pH instruments. Furthermore, the spectrophotometric method is calibration-free (see section 3.2.4 Spectrophotometric method in Chapter 3), which is ideal for long-term deployments on remote platforms.

1.7. Thesis objectives

The aim of my project was to develop an accurate and precise autonomous *in situ* pH sensor for long term deployments on ships and remote platforms. The system was based on the spectrophotometric approach. The first step of the miniaturization was the implementation of the spectrophotometric method on a simple micro-fluidic platform with low power and reagent consumption. This bench-top system has been thoroughly tested and deployed at sea onboard

research vessels several times. Underway pH data collected during the RRS *Discovery* cruise D366 have been used to study the pH dynamics in surface seawater of the North western European shelf. The second step of the miniaturization was the replacement of the spectrophotometer by a single photodiode. Results obtained in the laboratory proved the feasibility of this key step and the great potential of the approach undertaken.

1.8. Thesis outline

Chapter 2 presents the methods used for chemical preparation, system development and testing. The data processing method and error analysis are also described. This chapter, together with Chapter 4, can be used for knowledge transfer to enable follow on research and development of this technology.

Spectrophotometric pH systems are deployed on ships and *in situ* on remote platforms. Smaller and more rugged instruments are nevertheless required for a more widespread *in situ* application to allow routine high resolution measurements even in the most remote regions. Chapter 3 critically reviews oceanic pH measurements, and focuses on *state-of-the-art* spectrophotometric pH measurement techniques and instrumentation. This chapter was published as a journal article in Trends in Analytical Chemistry (Rérolle et al., 2012).

Chapter 4 presents the results obtained with the system developed for this thesis. The first part reports the initial steps toward the miniaturisation of the colorimetric pH sensor with the successful implementation of a simple microfluidic design with low reagent consumption. The system is particularly adapted to shipboard deployment: high quality data were obtained over a period of more than a month during a shipboard deployment around the UK during which less than 30 mL of indicator was consumed. The system featured a short term precision of 0.001 pH (n=20) and an accuracy within the range of a certified Tris buffer (0.004 pH). The optical set up was robust and relatively small due to the use of an USB mini-spectrometer, a custom made polymeric flow cell and an LED light source. The measurement was made close to *in situ* temperature (+ 0.2 °C) in the sampling chamber which had a continuous flow of the ship's underway seawater supply. A journal article summarising the results and findings is published in Analytica Chimica Acta (Rérolle et al., 2013). The system is adaptable for continuous underway measurements or discrete samples analysis. The use of meta-Cresol Purple indicator has been implemented on the discrete pH system. Two indicators, Thymol Blue and meta-Cresol Purple, can therefore be used on the system with the same level of precision. Finally a smaller and very simple design is possible with the use of a single photodiode instead of the USB

spectrophotometer. A precision of 0.004 pH units has been achieved with the photodiode which should be improved with straightforward amendments of the physical set-up.

Chapter 5 presents the underway pH data collected during the cruise deployment D366 in the North West European Shelf Seas in summer 2011. A paper is in preparation based on this work for a special edition on the data from the cruise D366 in Biogeosciences. This is the first time that pH has been measured at such a high spatial resolution (10 Measurements.h^{-1}) in this shelf sea region. The aim of our paper is to study the carbonate chemistry dynamics of the surface water using pH and ancillary data. The main processes controlling the pH distribution along the ship's transect, and their relative importance, are unraveled using a statistical approach. The study highlights the impact of biological activity, temperature and riverine inputs on the carbonate chemistry dynamics of the shelf sea surface water. For this summer cruise, the biological activity appeared to be the main control of the pH distribution along the cruise transect. Chlorophyll and nutrients variations explained 29% of the pH variance along the whole cruise transect and as much as 68% in the northern part of the transect. On the contrary, in the Skagerrak region, temperature distribution explained about 50% of the pH variation. Riverine inputs were evidenced by high dissolved organic matter levels in the Strait of Moyle and the southern North Sea with consequent remineralisation processes and a reduction in pH. DOC distribution described 15% of the pH variance along the full transect.The effect on surface seawater pH of deep water mixing was observed in two well defined regions where pH and temperature levels were lower than in the surroundings waters whereas DIC and nutrients levels were higher. This study highlights the high spatial variability of the surface water pH in shelf seawaters where a range of processes simultaneously impact the carbonate chemistry.

Chapter 6 summarises briefly the achievements presented in this thesis and suggest several tasks to improve and further miniaturize the pH system.

References

Archer, D., Eby, M., Brovkin, V., Ridgwell, A., Cao, L., Mikolajewicz, U., Caldeira, K., Matsumoto, K., Munhoven, G., and Montenegro, A.: Atmospheric lifetime of fossil fuel carbon dioxide, Annual Review of Earth and Planetary Sciences, 37, 117-134, 2009.

Assmann, S., Frank, C., and Koertzinger, A.: Spectrophotometric high-precision seawater pH determination for use in underway measuring systems, Ocean Science, 7, 597-607, 10.5194/os-7-597-2011, 2011.

Bellerby, R. G. J., Millward, G. E., Turner, D. R., and Worsfold, P. J.: Approaches to the continuous monitoring of seawater pH and its role in the global carbon cycle, TrAC Trends in Analytical Chemistry, 12, ix-ix, 1993.

Bellerby, R. G. J., Turner, D. R., Millward, G. E., and Worsfold, P. J.: Shipboard flow injection determination of sea water pH with spectrophotometric detection, Analytica Chimica Acta, 309, 259-270, 1995.

Bellerby, R. G. J., Olsen, A., Johannessen, T., and Croot, P.: A high precision spectrophotometric method for on-line shipboard seawater pH measurements: The automated marine pH sensor (AMpS), Talanta, 56, 61-69, 2002.

Borowitzka, M. A., and Larkum, A. W. D.: Reef algae, Oceanus, 29, 49-54, 1986.

Broecker, W. S., and Peng, T.: Tracers in the Sea, Lamont-Doherty Geological Observatory, Columbia University, 1982.

Broecker, W. S.: The oceanic CaCO 3 cycle, Treatise on Geochemistry, 6, 529–549, 2003.

Byrne, R. H., Mecking, S., Feely, R. A., and Liu, X.: Direct observations of basin-wide acidification of the North Pacific Ocean, Geophysical Research Letters, 37, L02601, 2010.

Caldeira, K., and Wickett, M. E.: Ocean model predictions of chemistry changes from carbon dioxide emissions to the atmosphere and ocean, J. Geophys. Res, 110, 1-12, 2005.

Canadell, J. G., Le Quéré, C., Raupach, M. R., Field, C. B., Buitenhuis, E. T., Ciais, P., Conway, T. J., Gillett, N. P., Houghton, R., and Marland, G.: Contributions to accelerating atmospheric CO2 growth from economic activity, carbon intensity, and efficiency of natural sinks, Proceedings of the National Academy of Sciences, 104, 18866-18870, 2007.

Cooper, T. F., De'Ath, G., Fabricius, K. E., and Lough, J. M.: Declining coral calcification in massive Porites in two nearshore regions of the northern Great Barrier Reef, Global Change Biology, 14, 529-538, 2008.

Cullison-Gray, S. E., DeGrandpre, M. D., Moore, T. S., Martz, T. R., Friederich, G. E., and Johnson, K. S.: Applications of in situ pH measurements for inorganic carbon calculations, Marine Chemistry, 2011.

DelValls, T. A.: Underway pH measurements in upwelling conditions: The California current, Ciencias Marinas, 25, 345-365, 1999.

Dickson, A., and Riley, J.: The estimation of acid dissociation constants in seawater media from potentionmetric titrations with strong base. I. The ionic product of water--Kw, Marine Chemistry, 7, 89-99, 1979.

Dickson, A.: The carbon dioxide system in seawater: equilibrium chemistry and measurements, Guide to Best Practices for Ocean Acidification Research and Data Reporting, 1, 17–40, 2010.

Dickson, A. G.: An exact definition of total alkalinity and a procedure for the estimation of alkalinity and total inorganic carbon from titration data, Deep-Sea Res, 28, 609–623, 1981.

Dittrich, P. S., Tachikawa, K., and Manz, A.: Micro Total Analysis Systems. Latest Advancements and Trends, Analytical Chemistry, 78, 3887-3908, 10.1021/ac0605602, 2006.

Dlugokencky, E., and Tans, P. P.: NOAA/ESRL,Trends in atmospheric carbon dioxide: http://www.esrl.noaa.gov/gmd/ccgg/trends , last access May 2013.

Doney, S. C., Balch, W. M., Fabry, V. J., and Feely, R. A.: Ocean acidification: A critical emerging problem for the ocean sciences, Oceanography, 22, 16-+, 2009a.

Doney, S. C., Tilbrook, B., Roy, S., Metzl, N., Le Quéré, C., Hood, M., Feely, R. A., and Bakker, D.: Surface-ocean CO2 variability and vulnerability, Deep Sea Research Part II: Topical Studies in Oceanography, 56, 504-511, 10.1016/j.dsr2.2008.12.016, 2009b.

Doney, S. C.: The growing human footprint on coastal and open-ocean biogeochemistry, Science, 328, 1512, 2010.

Dore, J. E., Lukas, R., Sadler, D. W., Church, M. J., and Karl, D. M.: Physical and biogeochemical modulation of ocean acidification in the central North Pacific, Proceedings of the National Academy of Sciences, 106, 12235, 2009.

Engel, A., Zondervan, I., Aerts, K., Beaufort, L., Benthien, A., Chou, L., Delille, B., Gattuso, J. P., Harlay, J., and Heemann, C.: Testing the direct effect of CO 2 concentration on a bloom of the coccolithophorid Emiliania huxleyi in mesocosm experiments, Limnology and oceanography, 493-507, 2005.

Fabry, V. J., Seibel, B. A., Feely, R. A., and Orr, J. C.: Impacts of ocean acidification on marine fauna and ecosystem processes, ICES Journal of Marine Science, 65, 414, 2008.

Gazeau, F., Quiblier, C., Jansen, J. M., Gattuso, J. P., Middelburg, J. J., and Heip, C. H. R.: Impact of elevated CO2 on shellfish calcification, Geophysical Research Letters, 34, L07603, 2007.

González-Dávila, M.: The water column distribution of carbonate system variables at the ESTOC site from 1995 to 2004, Biogeosciences, 7, 1995-2032, 2010.

Guinotte, J. M., and Fabry, V. J.: Ocean acidification and its potential effects on marine ecosystems, Annals of the New York Academy of Sciences, 1134, 320-342, 2008.

Holliday, N.: Air-sea interaction and circulation changes in the northeast Atlantic, Journal of geophysical research, 108, 3259, 2003.

Hoppe, C., Langer, G., Rokitta, S., Wolf-Gladrow, D., and Rost, B.: Implications of observed inconsistencies in carbonate chemistry measurements for ocean acidification studies, Biogeosciences, 2012.

Iglesias-Rodriguez, M. D., Halloran, P. R., Rickaby, R. E. M., Hall, I. R., Colmenero-Hidalgo, E., Gittins, J. R., Green, D. R. H., Tyrrell, T., Gibbs, S. J., and Von Dassow, P.: Phytoplankton calcification in a high-CO2 world, Science, 320, 336, 2008.

Intergovernmental Panel on Climate, C., Team, C. W., Pachauri, R. K., and Reisinger, A. e.: IPCC, 2007: Climate Change 2007: Synthesis Report. Contribution of Working Groups I, II and III to the Fourth Assessment Report of the Intergovernmental Panel on Climate Change, IPCC, Geneva, Switzerland, 104 pp., 2007.

Johnson, K. S., Berelson, W. M., Boss, E. S., Chase, Z., Claustre, H., Emerson, S. R., Gruber, N., Kortzinger, A., Perry, M. J., and Riser, S. C.: Observing biogeochemical cycles at global scales with profiling floats and gliders: Prospects for a global array, Oceanography, 216-225, 2009.

Kaltenbacher, E., Steimle, E., and Byrne, R.: A compact, in-situ, spectrophotometric sensor for aqueous environments: design and applications, 2000, 41-45,

Key, R. M., Kozyr, A., Sabine, C. L., Lee, K., Wanninkhof, R., Bullister, J. L., Feely, R. A., Millero, F. J., Mordy, C., and Peng, T. H.: A global ocean carbon climatology: Results from Global Data Analysis Project (GLODAP), Global Biogeochem. Cycles, 18, 2004.

Kim, H., and Lee, K.: Significant contribution of dissolved organic matter to seawater alkalinity, Geophys. Res. Lett, 36, L20603, 10.1029/2009GL040271, 2009.

Kuffner, I. B., Andersson, A. J., Jokiel, P. L., Rodgers, K. u. S., and Mackenzie, F. T.: Decreased abundance of crustose coralline algae due to ocean acidification, Nature Geosci, 1, 114-117, 2008.

Langer, G., Geisen, M., Baumann, K. H., Klas, J., Riebesell, U., Thoms, S., and Young, J. R.: Species-specific responses of calcifying algae to changing seawater carbonate chemistry, Geochem. Geophys. Geosyst, 7, Q09006, 2006.

Le Quéré, C.: Closing the global budget for CO2, Global Change, 74, 28-31, 2009.

Le Quéré, C., Andres, R., Boden, T., Conway, T., Houghton, R., House, J., Marland, G., Peters, G., van der Werf, G., and Ahlström, A.: The global carbon budget 1959-2011, Earth System Science Data, 5, 165-185, 2013.

Liu, X., Wang, Z. A., Byrne, R. H., Kaltenbacher, E. A., and Bernstein, R. E.: Spectrophotometric measurements of pH in-situ: Laboratory and field evaluations of instrumental performance, Environmental Science and Technology, 40, 5036-5044, 2006.

Martz, T. R., Carr, J. J., French, C. R., and DeGrandpre, M. D.: A submersible autonomous sensor for spectrophotometric pH measurements of natural waters, Analytical Chemistry, 75, 1844-1850, 2003.

Millero, F., ZHANG, J., Lee, K., and Campbell, D.: Titration alkalinity of seawater, Marine Chemistry, 44, 153-165, 1993.

Millero, F. J.: The marine inorganic carbon cycle, Chemical Reviews, 107, 308-341, 2007.

Mosley, L. M., Husheer, S. L. G., and Hunter, K. A.: Spectrophotometric pH measurement in estuaries using thymol blue and m-cresol purple, Marine Chemistry, 91, 175-186, 2004.

Najjar, R. G.: Marine biogeochemistry, Climate system modeling, 241-280, 1992.

Nakano, Y., Kimoto, H., Watanabe, S., Harada, K., and Watanabe, Y. W.: Simultaneous vertical measurements of in situ pH and CO2 in the sea using spectrophotometric profilers, Journal of Oceanography, 62, 71-81, 2006.

NOAA National Climatic Data Center: State of the Climate: Global Analysis for November 2012, published online December 2012, retrieved on January 9, 2013 from http://www.ncdc.noaa.gov/sotc/global/. 2012.

Ohline, S. M., Reid, M. R., Husheer, S. L. G., Currie, K. I., and Hunter, K. A.: Spectrophotometric determination of pH in seawater off Taiaroa Head, Otago, New Zealand: Full-spectrum modelling and prediction of pCO2 levels, Marine Chemistry, 107, 143-155, 2007.

Prien, R. D.: The future of chemical in situ sensors, Marine Chemistry, 107, 422-432, 10.1016/j.marchem.2007.01.014, 2007.

Rakestraw, N.: The conception of alkalinity or excess base in seawater, Journal of Marine Research, 8, 14-20, 1949.

Rérolle, V., Floquet, C. F. A., Mowlem, M. C., Connelly, D. P., Achterberg, E. P., and Bellerby, R. R. G. J.: Seawater-pH measurements for ocean-acidification observations, TrAC Trends in Analytical Chemistry, 40, 146-157, http://dx.doi.org/10.1016/j.trac.2012.07.016, 2012.

Rérolle, V., Floquet, C. F., Harris, A. J., Mowlem, M. C., Bellerby, R. R., and Achterberg, E. P.: Development of a colorimetric microfluidic pH sensor for autonomous seawater measurements, Analytica Chimica Acta, In Press, 2013.

Ridgwell, A., and Zeebe, R. E.: The role of the global carbonate cycle in the regulation and evolution of the Earth system, Earth and Planetary Science Letters, 234, 299-315, 2005.

Riebesell, U., Zondervan, I., Rost, B., Tortell, P. D., Zeebe, R. E., and Morel, F. M. M.: Reduced calcification of marine plankton in response to increased atmospheric CO 2, Nature, 407, 364-367, 2000.

Sabine, C. L., Feely, R. A., Gruber, N., Key, R. M., Lee, K., Bullister, J. L., Wanninkhof, R., Wong, C. S., Wallace, D. W. R., and Tilbrook, B.: The oceanic sink for anthropogenic CO2, Science, 305, 367-371, 2004.

Sciandra, A., Harlay, J., Lefèvre, D., Lemée, R., Rimmelin, P., Denis, M., and Gattuso, J. P.: Response of coccolithophorid Emiliania huxleyi to elevated partial pressure of CO~ 2 under nitrogen limitation, MARINE ECOLOGY-PROGRESS SERIES-, 261, 111-122, 2003.

Seidel, M. P., DeGrandpre, M. D., and Dickson, A. G.: A sensor for in situ indicator-based measurements of seawater pH, Marine Chemistry, 109, 18-28, 2008.

Shirayama, Y., and Thornton, H.: Effect of increased atmospheric CO 2 on shallow water marine benthos, J. Geophys. Res, 110, 2005.

Skjelvan, I., Falck, E., Rey, F., and Kringstad, S.: Inorganic carbon time series at Ocean Weather Station M in the Norwegian Sea, Biogeosciences, 5, 549-560, 2008.

Tapp, M., Hunter, K., Currie, K., and Mackaskill, B.: Apparatus for continuous-flow underway spectrophotometric measurement of surface water pH, Marine Chemistry, 72, 193-202, 2000.

Thomas, H., Bozec, Y., de Baar, H. J. W., Elkalay, K., Frankignoulle, M., Schiettecatte, L. S., Kattner, G., and Borges, A. V.: The carbon budget of the North Sea, Biogeosciences, 2, 87-96, 2005.

Volk, T., and Hoffert, M.: Ocean carbon pumps-Analysis of relative strengths and efficiencies in ocean-driven atmospheric CO2 changes, Cambridge Contemporary Astrophysics, 99-110, 1985.

Wang, Z. A., Liu, X., Byrne, R. H., Wanninkhof, R., Bernstein, R. E., Kaltenbacher, E. A., and Patten, J.: Simultaneous spectrophotometric flow-through measurements of pH, carbon dioxide fugacity, and total inorganic carbon in seawater, Analytica Chimica Acta, 596, 23-36, 2007.

Wolf-Gladrow, D. A., Riebesell, U., Burkhardt, S., and Bijma, J.: Direct effects of CO2 concentration on growth and isotopic composition of marine plankton, Tellus B, 51, 461-476, 1999.

Zeebe, R. E., and Wolf-Gladrow, D. A.: CO2 in seawater: equilibrium, kinetics, isotopes, Elsevier Science, 2001.

Zondervan, I., Zeebe, R. E., Rost, B., and Riebesell, U.: Decreasing marine biogenic calcification: A negative feedback on rising atmospheric pCO2, Global Biogeochemical Cycles, 15, 2001.

Zondervan, I., Rost, B., and Riebesell, U.: Effect of CO2 concentration on the PIC/POC ratio in the coccolithophore Emiliania huxleyi grown under light-limiting conditions and different daylengths, Journal of Experimental Marine Biology and Ecology, 272, 55-70, 2002.

Chapter 2: Methods

This chapter provides technical details of the methods used such as chemical preparation, system development and testing. An overview of the principles of operation, design and testing of the pH sensor is given in chapter 4. Two set up are possible for the pH sensor, referred as system 1 (connected to the underway seawater supply of the ship with continuous measurements) and system 2 (controlled at 25 °C for discrete sample measurements). These two set ups differ mainly on two aspects: pumps and temperature control. These differences will be detailed in Chapter 4.

2.1. Chemical preparation

2.1.1. Indicator solutions

A 2 mM thymol blue indicator solution was prepared by dissolution of thymol blue sodium salt (ACS Reagent, $C_{27}H_{29}NaO_5S$, Sigma Aldrich 861367) in deionised water (MilliQ, Millipore, >18.2 mΩ cm^{-1}). A 2 mM meta-Cresol Purple (mCP) solution with an ionic strength of 0.7 was prepared by dissolution of mCP sodium salt (Acros Organics, 199250050) and sodium chloride (NaCl; Fisher Scientific, S/3160153) in deionised water. The solutions were left to equilibrate overnight and the pH was adjusted to ca. 8.1±0.02 using a 1 M sodium hydroxide solution (NaOH, Fisher Scientific S/4920/53). The pH of the solution was verified with a glass electrode (LL Combined Unitrode PT 1000 WC-Electrode, Metrohm UK Ltd) calibrated with NBS buffer solutions (Fluka Analytical, Sigma Aldrich). The indicator solutions were stored in gas tight nutrition bags (Flexboy® Bags, Sartorius Stedim Biotech) wrapped in aluminium foil to avoid photo-bleaching.

2.1.2. Acid buffers and basic solutions

Acidic buffer solutions of pH≈5 ± 0.1 were prepared using acetic acid ($C_2H_4O_2$, Fisher Scientific A/0400/PB08), sodium acetate trihydrate ($C_2H_3NaO_2.3H_2O$, Fisher Scientific S/2000/53) and sodium chloride (NaCl, Fisher Scientific S/3160/53). Basic solutions of pH ≈ 10 ± 0.5 were prepared by dissolution of NaCl in deionized water and adjustment of the pH with 1 M NaOH. The pH of the solution was measured using the glass electrode. Both acidic and basic solutions were adjusted with NaCl to certain ionic strengths in order to mimic seawater at four salinities: 22.5, 27.5, 32.5 and 37.5 PPT, as detailed in Table 2.1. The pH of the solutions was verified with a glass pH electrode.

Table 2.1: Composition of the acidic and basic solutions used for indicator characterization (weights for 1 liter of solution)

Acidic Buffer (Salinity in PPT)	**m$C_2H_3NaO_2.3H_2O$ (g)**	**m$C_2H_4O_2$ (g)**	**mNaCl (g)**
1 (22.46)	7.757	1.375	19.163
2 (27.46)	7.770	1.370	24.165
3 (32.46)	7.784	1.363	29.17
4 (37.46)	7.784	1.363	34.179
Basic solution (Salinity)	**mNaCl (g)**	**1 M NaOH (mL)**	
1 (22.46)	22.46	1	
2 (27.46)	27.46	1	
3 (32.46)	32.46	1	
4 (37.46)	37.46	1	

2.2. Microfluidic flow cell: Fabrication method

The microfluidic flow cell comprises the absorption cell and static serpentine mixer and was manufactured in tinted poly(methyl methacrylate) (PMMA, thicknesses: 8 mm for the cell and 3 mm for the lid) obtained from Evonik Industries AG (PLEXIGLAS® Shop, Germany). The fabrication method has been developed in the Sensor group and is detailed in Ogilvie *et al.* and Floquet *et al.* (Floquet et al., 2011;Ogilvie et al., 2010). The design of the cell was first drawn in 2D drawing software such as DraftSight (Solidworks). It was converted as a tool path with the CircuitCam software (LPKF laser and electronics AG, Garbsen, Germany) and the channels were then micro-milled on one side of the PMMA chip with an automated LPKF Proto S100 micro-mill. A lid of similar shape and material but without channels was subsequently solvent-bonded on top; first by exposure to chloroform at 25°C for 3-4 minutes and secondly, by hot pressure of the two assembled parts in a LPKF Multipress. The solvent vapour softened the sections for bonding and also polished the channels resulting in reduced optical losses (Ogilvie et al., 2010). All channel cross sections were 250 x 250 µm, except for the 1 cm absorption cell which was 700 x 700 µm. The static mixer was a long (2.2 m) serpentine shaped channel. The design of the flow cell is detailed in Figure 2.1. The tools used for the fabrication of the chip and the settings are detailed in Table 2.2.

The light source and detector are connected to the cell using optical fibres (600 µm diameter, Thorlabs, USA) inserted directly in the PMMA chip. The fluidic connections are made with Minstac® connectors (Lee Products Ltd., UK) screwed on top of the PMMA chip.

Table 2.2: Milling tools and settings used for the fabrication of the microfluidic flow cell.

Feature	Colour on schema	Milling Depth (mm)	Tool	Tool setting Optimal Speed		
				Rotation (1/min)	Speed (mm/s)	z-speed (mm/s)
Serpentine	Green	0.25	0.25 EM	25000	5	2
Absorption cell	White	0.7	0.4 EM	15000	5	2
Holes (ALL)	Pink purple and blue	Through	2 EM	25000	20	6
Fibre optic connections	Purple	1.95 on chip 1.25 on lid	1 EM	25000	25	10
Fibre Optic holder	Purple	5	1 EM	25000	25	10
Fluid holes	Yellow	Through	0.7 Spiral Drill	25000	0	4

EM= End Mill

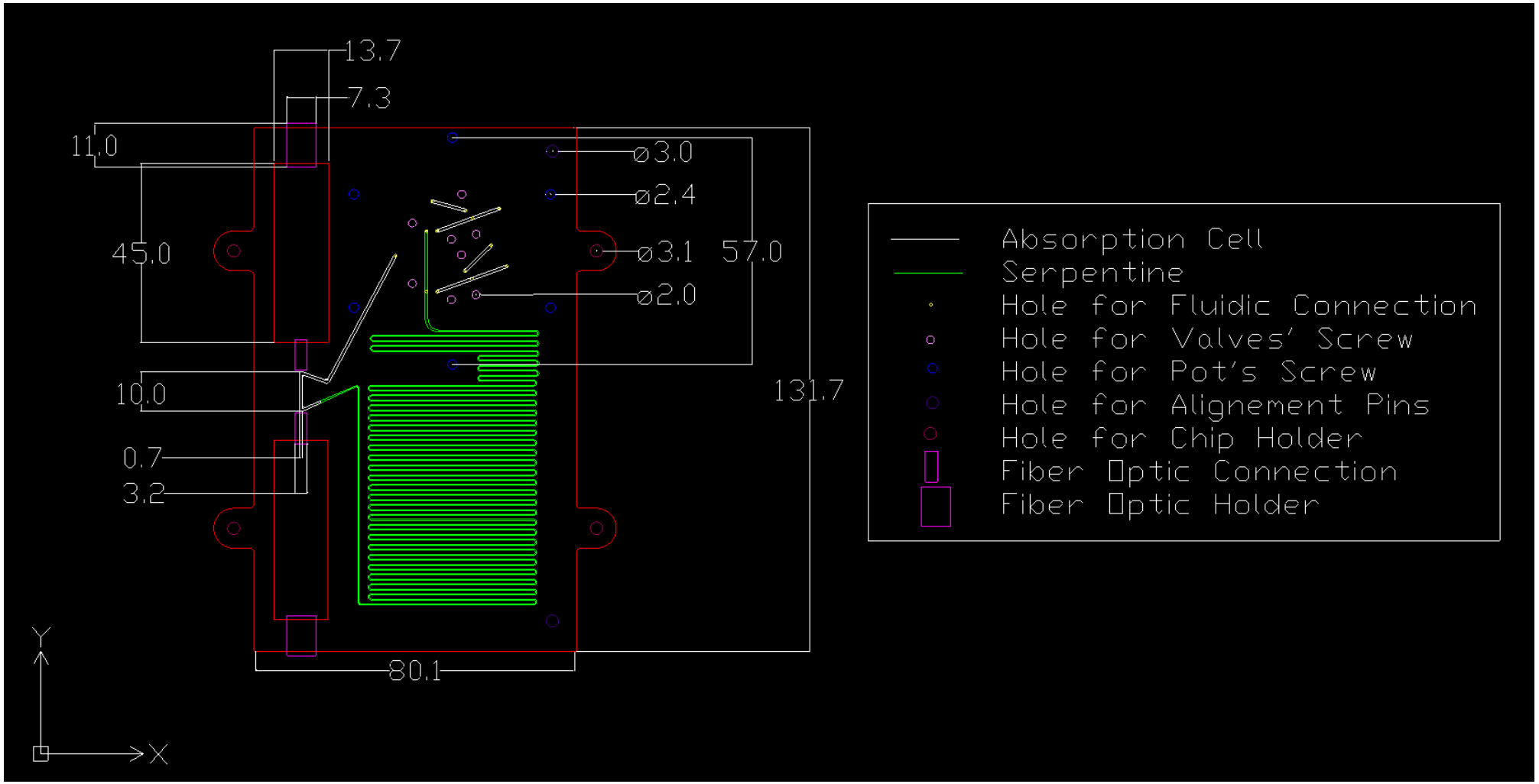

Figure 2.1: Schematic of the pH system's microfluidic chip designed in Draftsight® (bottom view). The different colours correspond to different features milled using different tools. This design will then be converted as a tool path using the CircuitCam® software. The dimensions, written in white are in mm.

2.3. Thermistors calibration

Three thermistors are used to measure the seawater temperature in the sampling chamber. This enables to check the reliability of the measurements and make sure that the thermistors have not drift. The thermistors are calibrated against the thermometer F250 (ASL, US) in a temperature controlled water bath (Fig. 2.2). The accuracy of the ASL F250 thermometer is estimated to be 0.01 °C (personal communication form Xi Huang). The thermistors can be used to measure temperature between -20°C and +30°C, depending on the calibration. The temperature range of the calibration depends on the range surface seawater temperature of the study area. Here is an example of the thermistors calibration done in June 2012 before deployment on the RRS James Clark Ross 271 research cruise.

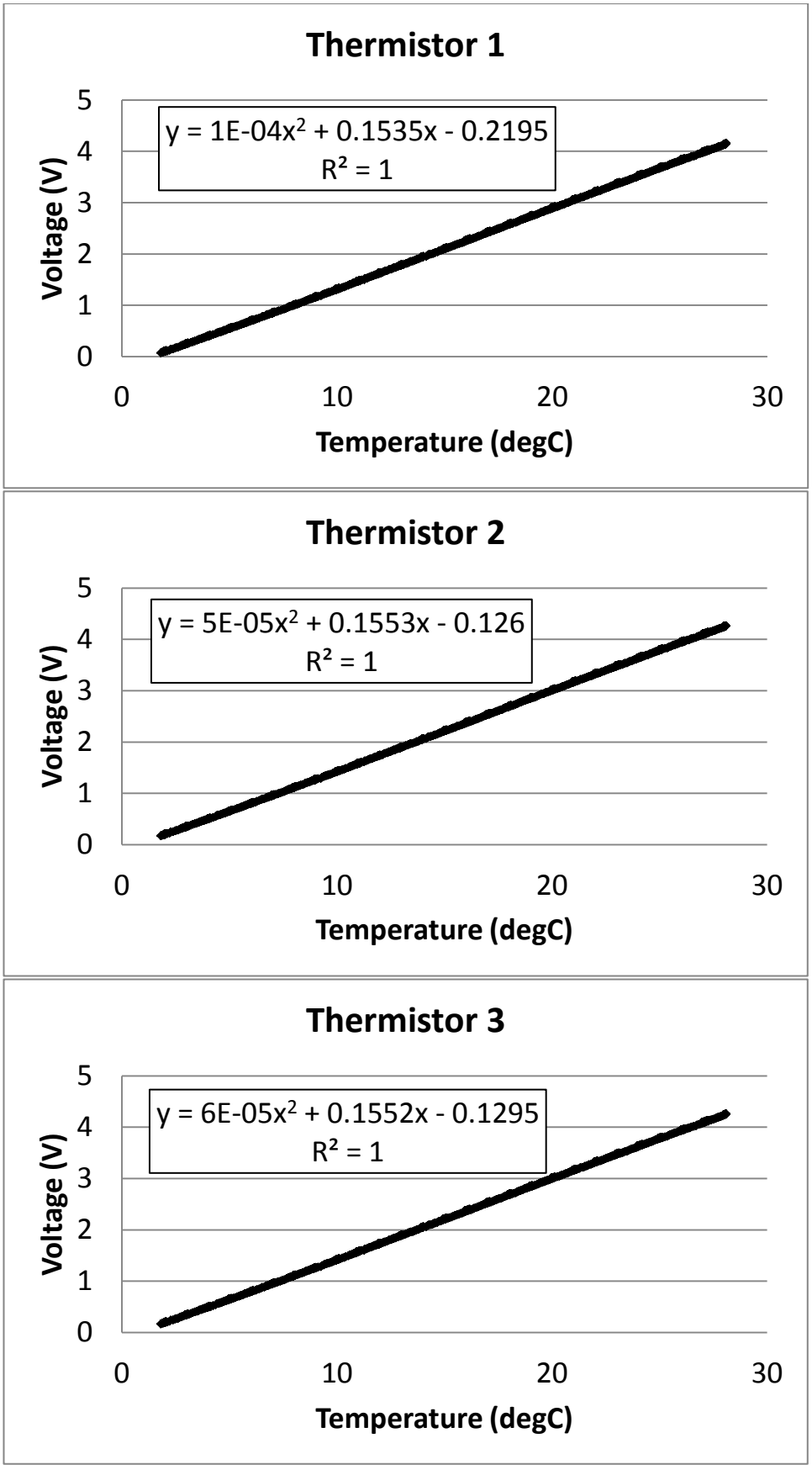

Figure 2.2: Calibration of the three thermistors against the ASL F250 thermometer in a temperature controlled water bath.

2.4. Replacement of the spectrophotometer with a photodiode

The last experiment undertaken to miniaturize the system was the replacement of the spectrophotometer with a single photodiode (TSL257, TAOS Inc., USA). In order to measure at the three wavelengths of interest (435, 596 and 750 nm), the three LEDs are switched On and Off, alternatively. The measurement at the different wavelengths needs to be relatively simultaneous to observe the absorbance variations while the indicator slug passes through the cell. A microcontroller based system (PIC, Microchip Technology Inc., Arizona, USA), developed in house, controls the timing intervals of the LEDs. A timing interval of 104 ms On and 66 ms Off was chosen to obtain the most stable signal while measuring the three wavelengths within a short time period.

2.5. System control (LabVIEW program)

2.5.1. Control of the systems with the spectrophotometer

The system is controlled by computer using custom software (written in LabVIEW, National Instruments Corporation, US). Note: spectra read in LabVIEW seem to have an offset of 5 nm compared to spectra read in Spectra-Suite (Ocean Optics). This offset is due to the wrong calibration coefficients used in LabVIEW to convert the pixel number to the corresponding wavelength. The correct coefficients are supplied by Ocean Optics for each spectrometer with the calibration certificate and can be changed in the spectrometer's LabVIEW subVI. Here, it does not affect our data as data from the whole LED peaks are used. Three versions of the virtual instrument software (VI) are available:

1. **A manual version allowing control of each element of the system and instruments individually**. This is convenient when setting up the system, debugging or rinsing the system prior to shut down.
2. **A version that automates optics and fluidics control and data logging for system 1.** A user interface allows the control of the LED voltage and the spectrometer integration time in order to obtain the required signal. Once the required parameters are entered, the START button will start the measurement sequence and the system will run continuously until stopped by the user.
3. **A version that automates optics and fluidics control and data system 2.** A user interface allows the control of the LED voltage, the spectrometer integration time, the pumping time for the sample and indicator pumps, the number of measurements per sample and

the type of sample (e.g. CTD, UNDERWAY or BIOASSAY). Once the required parameters are entered, the START button will start the measurement sequence and the system will run continuously until the number of measurements demanded is reached.

Raw data (e.g. intensity spectra and thermistors' voltage outputs) are saved in a single table: the first column corresponds to the wavelength and then each column is a different spectrum in counts per seconds, the last three lines of each column are the thermistors' voltages, see 2.3. Thermistors calibration). Each measurement's file is named with the date and time and a suffix 'ref' or 'sample' (e.g. m1206071545ref='m'YYMMDDhrmin'ref', the letter 'm' is to avoid names starting with a number which can be an issue when processing the data with Matlab®).

2.5.2. Control of the system with the photodiode

Another VI has been developed to control the system with the photodiode. Raw data are saved in a single table with a different line for each measurement point. The first column is the time elapsed since the start of the measurement, the second column is the photodiode voltage output, the columns 3, 4 and 5 correspond to the state (1=On or 0=Off) of the LEDs 1 (435 nm), 2 (596 nm) and 3 (750 nm) respectively. The final last three columns report the voltage outputs of each thermistor (see 2.3. Thermistors calibration).

2.6. Indicator solution characterization

2.6.1 Determination of the extinction coefficients of the Thymol Blue indicator

The pK_2 for the thymol blue indicator as determined by Zhang and Byrne (Zhang and Byrne, 1996) was used

$$pK_2=-\log_{10}([H^+]_T[I^{2-}]/[HI^-]) = 4.706S/T + 26.3300 - 7.17218\log_{10}(T)- 0.017316\ S$$

where $[H^+]_T$ is the total hydrogen ion concentration in seawater (mol.kg-soln^{-1}), T is the temperature in Kelvin and S the salinity (Zhang and Byrne, 1996). The molar extinction coefficients of the batch of thymol blue indicator were determined (as described below) for the temperature and salinity ranges encountered during our deployments in tropical and temperate surface ocean waters (T= 8-26 °C and S=22.5-37.5 PPT).

The molar extinction coefficients of the acid indicator form (HI^-) at wavelengths 435 nm and 596 nm were determined in the acidic buffer. The basic solution was used to obtain the coefficients of the basic form (I^{2-}) of the dye. Absorbance of the indicator in each buffer solution was measured at five indicator concentrations. The signal at each wavelength was obtained by

integration on the whole LED peak. A 1 cm absorption cell was used to determine $\varepsilon_{435}(HI^-)$ and $\varepsilon_{596}(I^{2-})$, and a 10 cm cell was used to determine $\varepsilon_{596}(HI^-)$ and $\varepsilon_{435}(I^{2-})$. The light source and detector were the same as for the pH system, e.g. 3λ LED and HR4000 spectrometer. The cells were made in PMMA using the design and fabrication method outlined above. Measurements of the 5 indicator concentrations for each of the four salinities (22.5, 27.5, 32.5 and 37.5 PPT) were performed at 5 temperatures (8, 12, 17, 22 and 26°C).

2.6.2. Characterization of the meta-Cresol Purple indicator

The characterization of mCP extinction coefficients was performed using the same method as for Thymol Blue but at 25°C and salinity 35 only. The pK_2 value was determined by absorption measurements of mCP in certified Tris buffer provided by Scripps Institution of Oceanography, USA (batch 10) at 25°C.

2.7. Cruise deployment

2.7.1. RRS Discovery Cruise D366

The underway pH sensor was deployed on cruise D366 as part of the UK Ocean Acidification Research Program. The automated pH system was operated continuously on the underway seawater supply in the period between 06/06/2011 to the 07/07/2011. Only 5 µL of indicator was injected per sample during the deployment. The volume of indicator was increased to 12 µL in studies conducted after the D366 deployment in order to reduce the Schlieren effect observed during the deployment (see section 4.2.3.3. Deviation due to Schlieren effect). Three bottles of certified Tris buffer (batch 7) provided by the Scripps Institution of Oceanography have been analysed at the beginning, the middle and the end of the cruise in order to evaluate the performances of the system.

2.7.2. RRS James Clark Ross Cruise JR271

The underway pH instrument and the second system for discrete samples were deployed on cruise JR271 as part of the UK Ocean Acidification Research Program. The automated pH system was operated continuously on the underway seawater supply in the period between 02/06/2011 to the 02/07/2011. The second system was set up on the bench next to the first system and temperature was controlled to 25°C with a water bath. CTD and samples from a pCO_2 perturbation bioassay experiment were analysed on this instrument using mCP. Five bottles of certified Tris buffer (batch 10) and two bottles of DIC/TA Certified Reference Material (CRM, batch 117) provided by the Scripps Institution of Oceanography have been analysed during the cruise in order to evaluate the performances of the two pH systems.

All pH values in this study are reported using the total pH scale (pH_{tot}), as this is the most commonly used pH scale, and importantly the only available certified pH buffer (Tris from Scripps) has been certified on this pH scale.

2.8. Data processing and error analysis

Data are processed in Matlab with a single text file output. Each line of the text file corresponds to a measurement with the following information: file name, date and time, temperature, pH, and other parameters used during the data processing (e.g. error on pH, regression coefficient, absorbance range…). Corresponding data from the underway water supply are also reported (e.g. coordinates, *in situ* temperature, salinity and fluorescence).

2.8.1. Data processing of the measurement made with the spectrophotometer

Absorbances at the three wavelengths (λ=435, 596 and 750 nm) are measured by integration of the light signal on the full spectrum of the LED.

$$A_\lambda = -\log_{10}\frac{\sum_{\lambda_a}^{\lambda_b} I_\lambda}{\sum_{\lambda_a}^{\lambda_b} I_\lambda^{ref}}$$

With I_λ intensity at wavelength λ, I_λ^{ref} reference intensity at wavelength λ, λ_a and λ_b the indexes of the start and end pixel respectively of the LED peak centered on wavelength λ.

Only the data from the selected absorbance range (1.6 to 0.5) are used to determine a linear relationship between pH and indicator concentration and interpolate the data to a zero indicator concentration. The interpolation of pH to a zero indicator concentration is undertaken using a weighted linear regression, whereby the weights are the reverse of the squared error (noted u) on pH at each concentration ($1/upH([ind])^2$).

All the data processing equations are detailed below and in the copy of the Matlab script used to process the data.

2.8.1.1. Error on pH data (uncertainty)

The error on pH is calculated as the square root of the sum of the squares of the estimated uncertainties of the method (e.g. the indicator pK and molar absorptivities, the accuracy of the temperature, salinity and absorption measurements).

$$pH_T = pK_2 + \log_{10}\left(\frac{R - e_1}{e_2 - R.e_3}\right) = pK_2 + \ln\left(\frac{R - e_1}{e_2 - R.e_3}\right).\frac{1}{\ln(10)}$$

Error propagation method:

$$u_{pH} = \sqrt{\left(\frac{\partial pH}{\partial pK_2}\cdot u_{pK_2}\right)^2 + \left(\frac{\partial pH}{\partial R}\cdot u_R\right)^2 + \left(\frac{\partial pH}{\partial e_1}\cdot u_{e_1}\right)^2 + \left(\frac{\partial pH}{\partial e_2}\cdot u_{e_2}\right)^2 + \left(\frac{\partial pH}{\partial e_3}\cdot u_{e_3}\right)^2}$$

$$u_{pH} = \sqrt{\left(D_{pK_2}\cdot u_{pK_2}\right)^2 + \left(D_R\cdot u_R\right)^2 + \left(D_{e_1}\cdot u_{e_1}\right)^2 + \left(D_{e_2}\cdot u_{e_2}\right)^2 + \left(D_{e_3}\cdot u_{e_3}\right)^2}$$

With $D_{pK_2} = 1$ $\qquad D_R = \frac{1}{\ln(10)}\cdot\frac{e_2 - e_1\cdot e_3}{(e_2 - R\cdot e_3)\cdot(R - e_1)}$

$$D_{e_1} = -\frac{1}{\ln(10)}\cdot\frac{1}{R - e_1} \qquad D_{e_2} = -\frac{1}{\ln(10)}\cdot\frac{1}{e_2 - R\cdot e_3}$$

$$D_{e_3} = \frac{1}{\ln(10)}\cdot\frac{R}{e_2 - R\cdot e_3}$$

Error on the absorbance ratio (u_R):

R is the ratio of absorbances defined as $R = \frac{A_2}{A_1} = \frac{\log_{10}\left(\frac{I_2^{ref}}{I_2}\right)}{\log_{10}\left(\frac{I_1^{ref}}{I_1}\right)} = \frac{\ln\left(\frac{I_2^{ref}}{I_2}\right)}{\ln\left(\frac{I_1^{ref}}{I_1}\right)}$

Then we have:

$$u_R = \sqrt{\left(\frac{\partial R}{\partial I_2^{ref}}\cdot u_2^{ref}\right)^2 + \left(\frac{\partial R}{\partial I_2}\cdot u_2\right)^2 + \left(\frac{\partial R}{\partial I_1^{ref}}\cdot u_1^{ref}\right)^2 + \left(\frac{\partial R}{\partial I_1}\cdot u_1\right)^2}$$

$$u_R = \sqrt{\left(D_1\cdot u_2^{ref}\right)^2 + \left(D_2\cdot u_2\right)^2 + \left(D_3\cdot u_1^{ref}\right)^2 + \left(D_4\cdot u_1\right)^2}$$

With: $\qquad D_1 = \frac{1}{\ln\left(\frac{I_1^{ref}}{I_1}\right)}\cdot\frac{1}{I_2^{ref}} \qquad D_2 = -\frac{1}{\ln\left(\frac{I_1^{ref}}{I_1}\right)}\cdot\frac{1}{I_2}$

$$D_3 = -\ln\left(\frac{I_2^{ref}}{I_2}\right)\cdot\frac{1}{I_1^{ref}\cdot\ln^2\left(\frac{I_1^{ref}}{I_1}\right)} \qquad D_4 = \ln\left(\frac{I_2^{ref}}{I_2}\right)\cdot\frac{1}{I_1\cdot\ln^2\left(\frac{I_1^{ref}}{I_1}\right)}$$

And the error on intensity:

The error on reference intensity is calculated as the standard deviation of the 10 reference spectra recorded.

$$u_1^{ref} = std\left(I_1^{ref1} : I_1^{ref10}\right)$$

$$u_2^{ref} = std\left(I_2^{ref1} : I_2^{ref10}\right)$$

The error on the signal intensity is determined from a linear relationship between the intensity level of the signal and the noise (this relationship was obtained using the standard deviation of 10 spectra at each intensity level).

$$u_1 = 0.0002I_1 + 165$$
$$u_2 = 0.0002I_2 + 160.31$$

Error on pK_2 (upK_2):

The pK_2 has been calculated following the Zhang & Byrne equation:

$$pK_2 = 4.706\frac{S}{T} + 26.3300 - 7.17218 \cdot \log_{10}(T) - 0.017316 \times S$$

Then

$$u_{pK_2} = \sqrt{\left(\frac{\partial pK_2}{\partial T} \cdot u_T\right)^2 + \left(\frac{\partial pK_2}{\partial S} \cdot u_S\right)^2}$$

$$u_{pK_2} = \sqrt{\left(\left(-4.706\frac{S}{T^2} - 7.17218\frac{1}{T}\right) \cdot u_T\right)^2 + \left(\left(4.706\frac{1}{T} - 0.017316\right) \cdot u_S\right)^2}$$

with u_S and u_T the uncertainties on the salinity and temperature.

Error on the extinction coefficients ratios (ue1, ue2 and ue3):

The extinction coefficients ratios are defined as follow:

$$e_1 = \frac{\varepsilon_2^{HI}}{\varepsilon_1^{HI}} \qquad e_2 = \frac{\varepsilon_2^{I}}{\varepsilon_1^{HI}} \qquad e_1 = \frac{\varepsilon_1^{I}}{\varepsilon_1^{HI}}$$

Then

$$u_{e_1} = \sqrt{\left(\frac{u_{\varepsilon_2^{HI}}}{\varepsilon_1^{HI}}\right)^2 + \left(\frac{\varepsilon_2^{HI}.u_{\varepsilon_1^{HI}}}{{\varepsilon_1^{HI}}^2}\right)^2}$$

$$u_{e_2} = \sqrt{\left(\frac{u_{\varepsilon_2^{I}}}{\varepsilon_1^{HI}}\right)^2 + \left(\frac{\varepsilon_2^{I}.u_{\varepsilon_1^{HI}}}{{\varepsilon_1^{HI}}^2}\right)^2}$$

$$u_{e_3} = \sqrt{\left(\frac{u_{\varepsilon_1^{I}}}{\varepsilon_1^{HI}}\right)^2 + \left(\frac{\varepsilon_1^{I}.u_{\varepsilon_1^{HI}}}{{\varepsilon_1^{HI}}^2}\right)^2}$$

With $\varepsilon_1^{HI}, \varepsilon_1^{I}, \varepsilon_2^{HI}$ *and* ε_2^{I} the indicator extinction coefficients dependent on salinity and temperature (see chapter 3 for the extinction coefficients definition and chapter 4 for their temperature and salinity dependency).

$$u_{\varepsilon_1}^{HI} = 2 * 0.5346 * T * u_T$$

$$u_{\varepsilon_2}^{HI} = (3.3209 + 2 * 0.1258 * T) * u_T$$

$$u_{\varepsilon_1}^{I} = 2 * 0.1472 * T * u_T$$

$$u_{\varepsilon_2}^{I} = \sqrt{(51.0149 * u_T)^2 + ((755.0331 + 2 * 13.4534 * S) * u_S)^2}$$

2.8.1.2. pH System Data Processing

1. Read Files 53
2. Absorbance 54
3. Error Analysis 55
4. Indicator Correction 57

1. Read Files

```
clear                                                                    all;

D=dir('J:\PhD\Cruise\JR271\underway\CRM\CRM1171075\*');
for z=8:2:1000
    clearvars -except underwaydata z lt underwaydata D;
    pHres='pHJR271.txt';% Name of text file
    nRows=2003;% Nnumber of rows in the file
    nR=nRows-3;% Nnumber of rows in the file without the three last lines of
temperature
    S=33.503;
```

Get data from reference and measurement files

```
    fnameref=D(z).name;
    eval('fnameref');
    fidref=fopen(fnameref,'r');
    dataref=fscanf(fidref,'%f');
    data2ref=reshape(dataref,[],nRows);
    fileref=data2ref';
    fclose(fidref);

    fname=D(z+1).name;
    eval('fname');
    fid=fopen(fname,'r');
    data=fscanf(fid,'%f');
    data2=reshape(data,[],nRows);
    file=data2';
    fclose(fid);
```

Time of the measurement

```
    datefin=D(z+1).date(1:11);
    heurefin=D(z+1).date(13:20);
    a=datevec(D(z+1).date);
    numfile=a(1)*10^7+(a(3)+151)*10^4+a(4)*10^2+a(5)*1-6;% Real sample time=6
minutes before end of measure

    darkc=mean(file(10:150,2)); % Dark of the spectrometer
```

LED peaks wavelengths index

```
    dk=darkc+200;    %    Intensity    level    to    identify    LED    peaks
    w435a=250+dsearchn(file(250:350,2),dk)-1;  % Begining of peak 1 (intensity
200C/s                      above                                        dark)
    w435b=450+dsearchn(file(450:550,2),dk)-1;    %    End    of    peak    1
    w596a=750+dsearchn(file(750:850,1),dk)-1;
    w596b=1000+dsearchn(file(1000:1150,2),dk)-1;
    w750a=1350+dsearchn(file(1350:1450,2),dk)-1;
    w750b=1650+dsearchn(file(1650:1750,2),dk)-1;
    [x,y]=max(file(w435a:w435b,2));w435=y+w435a-1;
    [x1,y1]=max(file(w596a:w596b,2));w596=y1+w596a-1;
    [x2,y2]=max(file(w750a:w750b,2));w750=y2+w750a-1;
```

Sample Temperature: Convert the voltages in degree Celsius. Equations from calibration (see Chapter 2.3 Thermistors calibration). There are 3 thermistors in sampling chamber, T=mean of the 3 thermistors.

```
volt=file(2001,5);T1=-0.0256*volt^2+6.5022*volt+1.4302;%    Yellow    thermistor
volt2=file(2002,5);T2=-0.0138*volt2^2+6.434*volt2  +  0.812;%  Green  thermistor
calib                                                          Dec2011
volt3=file(2003,5);T3=-0.0146*volt3^2+6.4397*volt3+0.8352;%    Blue    thermistor
T=mean([T1 T2 T3]);Tm=273.15+T;Tc=T;
```

2. Absorbance

```
n=size(file,2);upHwp=NaN(n,1);Abs435wp=NaN(n,1);Abs596wp=NaN(n,1);Abs750wp=NaN(n,
1);Rwp=NaN(n,1);pHwpLab=NaN(n,1);weights=NaN(n,1);
```

Calculate intensity

```
    I=ones(nR,n);Iref=ones(nR,1);
    for                                                          j=1:nR
        Iref(j)=mean(fileref(j,2:11))-darkc;
        for                                                       i=1:n
            I(j,i)=file(j,i)-darkc;
        end;
    end;

    for i=1:n
```

Calculate absorbance at the three wavelengths Integrate on the whole LED peak (wp)

```
Int435wp=sum(I(w435a:w435b,i));Int435refwp=mean(sum(Iref(w435a:w435b,:)));
Int596wp=sum(I(w596a:w596b,i));Int596refwp=mean(sum(Iref(w596a:w596b,:)));
Int750wp=sum(I(w750a:w750b,i));Int750refwp=mean(sum(Iref(w750a:w750b,:)));
        Abs750wp(i)=-log10(Int750wp/Int750refwp);
```

```
Abs435wp(i)=-log10(Int435wp/Int435refwp);
Abs596wp(i)=-log10(Int596wp/Int596refwp);
Rwp(i)=Abs596wp(i)/Abs435wp(i);
```

Extinction Coefficients determined in the laboratory November 2011

```
epsLABHI435wp=                                    -0.5346*Tc*Tc+1.3506e+004;
epsLABHI596wp=99.2208-3.3209*Tc+0.1258*Tc*Tc;
epsLABI435wp=2.2712e+003+0.1472*Tc*Tc;
epsLABI596wp=41881-51.0149*Tc-755.0331*S+13.4534*S*S;
e1LABwp=epsLABHI596wp/epsLABHI435wp;
e2LABwp=epsLABI596wp/epsLABHI435wp;
e3LABwp=epsLABI435wp/epsLABHI435wp;
```

pK2 from Zhang and Byrne 1996

```
a=4.706;
b=26.3300;
c=-7.17218;
d=-0.017316;
pK2=a*S/Tm+b+c*log10(Tm)+d*S;
```

Calculate pH

```
pHwpLab(i)=pK2+log10((Rwp(i)-e1LABwp)/(e2LABwp-Rwp(i)*e3LABwp));
```

3. Error Analysis

```
if                    i<2                    &&                    i<=(n-1)
    r=0;s=1;
elseif                  i>=2                   &&                    i<(n-1)
    r=1;s=1;
else                                                                 r=1;s=0;
end;
l=1;            %            Absorption            cell            length
ul=0;       %       Error       on       absorption       cell       length
uS=0;             %             Error             on             salinity
C=2E-3;      %      Indicator      stock      solution      concentration
uT=std([T1 T2 T3]); % Error on temperature
```

Error on intensity

```
ui435refwp=std(sum(Iref(w435a:w435b,:)));
ui596refwp=std(sum(Iref(w596a:w596b,:)));
ui435wp=0.0002*Int435wp+165;% I determined a linear relationship between
                                intensity   and   noise   in   intensity
ui596wp=0.0002*Int596wp+160.31;
```

Error on coefficients due to error propagation from Salinity and Temperature Salinity

```
uepsLABHI435=2*0.5346*T*uT;
uepsLABHI596=(3.3209+2*0.1258*T)*uT;
uepsLABI435=2*0.1472*T*uT;
uepsLABI596=sqrt((51.0149*uT)^2+((755.0331+2*13.4534*S)*uS)^2);
ue1=sqrt((1/epsLABHI435*uepsLABHI596)^2+(epsLABHI596/epsLABHI435^2*uepsLABHI435)^
2);
ue2=sqrt((1/epsLABHI435*uepsLABI596)^2+(epsLABI596/epsLABHI435^2*uepsLABHI435)^2)
;
ue3=sqrt((1/epsLABHI435*uepsLABI435)^2+(epsLABI435/epsLABHI435^2*uepsLABHI435)^2)
;
upK2=sqrt(((-4.706*S/Tm^2-7.17218/Tm)*uT)^2+((4.706/Tm-0.017316)*uS)^2);
        %
```

Error on Absorption Ratio R

```
D1wp=1/log(Int435refwp/Int435wp)*1/Int596refwp;
D2wp=-1/log(Int435refwp/Int435wp)*1/Int596wp;
D3wp=-log(Int596refwp/Int596wp)*1/(Int435refwp*log(Int435refwp/Int435wp)^2);
D4wp=log(Int596refwp/Int596wp)*1/(Int435wp*log(Int435refwp/Int435wp)^2);
uRwp=sqrt((D1wp*ui596refwp)^2+(D2wp*ui596wp)^2+(D3wp*ui435refwp)^2+(D4wp*ui435wp)
^2);
```

Error on pH

```
        Dpk2=1;
        DRwp=1/log(10)*(e2LABwp-e1LABwp*e3LABwp)/((e2LABwp-
Rwp(i)*e3LABwp)*(Rwp(i)-e1LABwp));
        De1wp=-1/log(10)*1/(Rwp(i)-e1LABwp);
        De2wp=-1/log(10)*1/(e2LABwp-Rwp(i)*e3LABwp);
        De3wp=1/log(10)*Rwp(i)/(e2LABwp-Rwp(i)*e3LABwp);

upHwp(i)=sqrt((Dpk2*upK2)^2+(DRwp*uRwp)^2+(De1wp*ue1)^2+(De2wp*ue2)^2+(De3wp*ue3)
^2);
        weights(i)=1/upHwp(i)^2;
        pHwperr=upHwp(i);

    end;
```

Find absorbances ranging from 0.55 and 1.65 to process the data

```
    AbsMax435=dsearchn(Abs435wp(:),1.65000);      %      Maximum      absorbance
    AbsMin596Search=dsearchn(Abs596wp(AbsMax435:n),0.55000);% Minimum absorbance
    AbsMin596=AbsMin596Search+AbsMax435-1;
    maxabs435=Abs435wp(AbsMax435);
    minabs596=Abs596wp(AbsMin596);
    nbpoints=AbsMin596-AbsMax435+1;
```

```
    if nbpoints>10 % If not enough data then there is probably a bubble or
particulate
```

```
        pHwpLabAbs1=pHwpLab(AbsMax435);
```

4. Indicator Correction

Calculate pH corrected from dye addition using Seidel et al. 2008's method

```
        TBconwpLAB=ones(nbpoints,1);
        for                                                    i=AbsMax435:AbsMin596
            TBconwpLAB(i-AbsMax435+1)=(epsLABI596wp*Abs435wp(i)-
epsLABI435wp*Abs596wp(i)-(epsLABHI596wp*Abs435wp(i)-
epsLABHI435wp*Abs596wp(i)))/(epsLABHI435wp*epsLABI596wp-
epsLABHI596wp*epsLABI435wp);
        end;
        % Weighted linear regression* to correct pH data from indicator induced
pH                                                                  perturbation
        [pHcorrWeightedWPLab,
upHcorrWeightedWPLab]=TBcorr(TBconwpLAB,pHwpLab(AbsMax435:AbsMin596),upHwp(AbsMax
435:AbsMin596));
        % Standard linear regression* to estimate error and confidence interval
        Conc=[ones(nbpoints,1)                                          TBconwpLAB];
        [B,BINT,R,RINT,STATS]=regress(pHwpLab(AbsMax435:AbsMin596),Conc);
        pHcorrwpLab=B(1);
        RMSwpLab=STATS(1);
        pHcorr95low=BINT(1,1);
        pHcorr95up=BINT(1,2);
        ConfInt=pHcorr95up-pHcorrwpLab;
        pHwperrmax=upHwp(AbsMax435);
        %
```

Write the results in a text file

```
        fid2=fopen(pHres,'a+');
        fprintf(fid2,'%3s %10s %10s %6.3f %6.4f %6.4f %6.4f %6.4f %6.4f %6.4f
%6.4f              %6.4f              %6.4f              %6.4f              %6.4f
%6.4f\r\n',fname,datefin,heurefin,T,pHcorrWeightedWPLab,upHcorrWeightedWPLab,RMSw
pLab,pHcorrWeightedWPLit,upHcorrWeightedWPLit,pHwperrmax,nbpoints,maxabs435,minab
s596,Int435refwp,Int596refwp,Int750refwp);
        fclose(fid2);
```

```
    else

    end;
```

```
end
```

Published with MATLAB® R2012b.

2.8.2. Data processing of the measurement made with a photodiode

Photodiode voltage data are first sorted and assigned to each LED. In order to obtain simultaneous data points at each wavelength, the discontinuous data are interpolated and filtered. The interpolation is made using a linear method with the function *interp1* in Matlab. The resulting dataset is then processed in a similar way as detailed above (e.g. calculate absorbance, pH and then correct for the indicator addition).

References

Floquet, C. F. A., V. J. Sieben, A. Milani, E. P. Joly, I. R. G. Ogilvie, H. Morgan, and M. C. Mowlem (2011), Nanomolar detection with high sensitivity microfluidic absorption cells manufactured in tinted PMMA for chemical analysis, *Talanta*, 235-239.

Mintrop, L.: Versatile Instrument for the Determination of Titration Alkalinity. Manual for versions 3S and 3C. Version 2.0. MARine ANalytics and DAta (MARIANDA), Kiel, Germany, 45 pp, 2004.

Ogilvie, I., V. Sieben, C. Floquet, R. Zmijan, M. Mowlem, and H. Morgan (2010), Reduction of surface roughness for optical quality microfluidic devices in PMMA and COC, *Journal of Micromechanics and Microengineering*, *20*, 065016.

Zhang, H., and R. H. Byrne (1996), Spectrophotometric pH measurements of surface seawater at in-situ conditions: absorbance and protonation behavior of thymol blue, *Marine Chemistry*, *52*(1), 17-25.

Chapter 3: Seawater pH measurements for ocean acidification observations: current approaches and future developments

3.1. Introduction

3.1.1. Impacts of atmospheric CO_2 emissions

The increasing concentration of CO_2 in the atmosphere as a result of fossil fuel burning and land use changes has significant impacts on the global climate, and one of the most noticeable effects is global warming. However, only 43% of the CO_2 emitted between 1959 and 2006 is still present in the atmosphere, the remainder has been taken up by land vegetation (29%) and the oceans (28%) (Canadell et al., 2007). Without these carbon sinks, climate change would likely be more pronounced.

The accumulation of CO_2 in the ocean results in a shift in the carbonate system equilibria, with a reduction in seawater pH (González-Dávila, 2010;Dore et al., 2009a;Byrne et al., 2010b;Wolf-Gladrow et al., 1999). Since the onset of the industrial revolution, average surface ocean pH has decreased by 0.1 pH units (Caldeira and Wickett, 2005), and currently the rate of decrease is 0.002 pH units per year (González-Dávila, 2010;Dore et al., 2009a;Byrne et al., 2010b). This phenomenon is called ocean acidification and is a major topic in oceanographic research. Significant shifts in the carbonate system form a serious cause of concern for marine biodiversity and ecosystem functioning, and in particular for calcifying organisms (Doney, 2010).

The changes in the marine carbonate system also reduce the ocean's capacity to absorb future atmospheric CO_2 emissions (Sabine et al., 2004). This decline in the efficiency of the oceanic CO_2 sink contributes to an acceleration in the rate of atmospheric CO_2 increase (Canadell et al., 2007).

High quality carbonate chemistry measurements are required in order to fully understand the dynamics of the oceanic carbonate system (Bellerby et al., 1993). The precision of seawater pH measurements needs to be better than 0.002 pH units in order to allow detection of the average annual surface ocean pH decrease (González-Dávila, 2010;Dore et al., 2009a;Byrne et al., 2010b). Seawater pH data with good spatial and temporal coverage are particularly critical to apprehend ocean acidification phenomena and their consequences.

3.1.2. Marine carbonate chemistry variables

Four variables of the marine carbonate system can be directly determined in an accurate manner: total dissolved inorganic carbon (DIC), partial pressure of CO_2 (pCO_2), total alkalinity (TA) and pH. If two of the carbonate system variables are determined, along with *in situ* temperature, salinity and macronutrients, it is possible to calculate the other two. With the spectrophotometric pH method, pH can be measured with a sufficiently high precision and accuracy to allow comparison

with the other thermodynamic variables that characterize the oceanic carbonate system (Cullison-Gray et al., 2011). Nevertheless, inconsistencies have been observed when using different pairs of variables to determine the carbonate system (Hoppe et al., 2012). The sources of these inconsistencies are uncertain but may be due to inaccuracies in the analytical measurements, inaccuracies in the thermodynamic constants used for the calculations or presence of dissolved organic acid/base compounds which are not taken into account in the estimation of alkalinity from titration using the Gran method (Kim and Lee, 2009). This highlights the need to measure more than two carbonate chemistry variables.

The spatial and temporal resolution of carbonate system measurements is currently still insufficient, despite important efforts to improve analytical methods, develop new instruments and coordinate international monitoring activities (Doney et al., 2009b). The deployment of appropriate sensors on moorings, drifters, or profiling floats would enable routine high resolution measurements in even the most remote regions (Johnson et al., 2009). There is therefore a growing need for autonomous *in situ* instruments that measure carbonate chemistry on remote platforms. Miniaturized pH systems with high analytical precision and accuracy would be optimal for deployment on oceanic moorings and small vehicles to allow large scale monitoring of ocean acidification. Widespread use, particularly on small platforms as part of a global observing system measuring ocean carbonate chemistry, will only be possible with low cost sensors featuring low power and resource (e.g. reagent) consumption. The simplicity and precision of the spectrophotometric seawater pH method makes it a good candidate for miniaturisation and deployment.

This article critically reviews oceanic pH measurements, and focuses on state-of-the art spectrophotometric pH techniques and instrumentation. A simple micro-fluidic design integrated in a shipboard pH instrument with high accuracy and precision is then presented as a key step towards the targeted *in situ* pH micro-sensor.

3.2. Analytical techniques for seawater pH measurements

3.2.1. Definition of pH and pH scales

pH is a measure of the hydrogen ion concentration in a solution and defined as:

$$\mathrm{pH} = -\log_{10}([\mathrm{H}^+]) \qquad (3.1)$$

whereby the hydrogen ion concentration is expressed in moles per kilogram of solution.

In chemical oceanography, different pH scales have been used, with pH buffers for the various pH scales made up in artificial seawater. The free pH scale only takes into account the free hydrogen ions (Bates and Culberson, 1977), whereas the total pH scale also considers sulphate (Hansson, 1973), and the seawater pH scale includes sulphate and fluoride complexes (Dickson and Millero, 1987;Dickson and Riley, 1979). The IUPAC NBS pH scale is based on low ionic strength buffer standards from the US National Bureau of Standards (NBS) and is universally used in laboratories. The NBS and free pH scales are often used in physiological studies (Dickson, 2010). The difference between the ionic strengths of the NBS pH buffers and seawater samples results in significant changes between calibration and sample measurements, and in particular affects the liquid junction potential when using potentiometric pH systems. This pH scale is hence deemed inappropriate for seawater applications and should not be used in marine carbonate chemistry. In oceanic carbonate chemistry research, the total hydrogen ion scale is most commonly used and forms the recommended pH scale (Dickson et al., 2007). The use of the total pH scale avoids problems associated with uncertainties in the stability constants for fluoride complexes which are required for the seawater pH scale. Importantly, a certified pH buffer based on the total pH scale is now available from the laboratory of Prof. A. Dickson, Scripps Institution of Oceanography at San Diego. This buffer is made of 2-amino-2-methyl-1,3-propanediol (TRIS) in artificial seawater. There is no certified reference material available based on the other seawater pH scales.

3.2.2. Potentiometric method

3.2.2.1 Glass electrode

The classical potentiometric method for the determination of pH in seawater consists of the measurement of the electromotive force (EMF) of a cell most commonly composed of a silver/silver chloride electrode and a glass pH electrode. The pH of a sample is defined in terms of EMF measured in the sample ($\underline{E}_{sample}$) and a standard buffer solution ($\underline{E}_{buffer}$) of assigned pH (pH_{buffer}):

$$pH_{sample} = pH_{buffer} + (E_{buffer} - E_{sample})\, F/(RT \ln 10) \qquad (3.2)$$

Where *R* is the gas constant, *T* is the measurement temperature and F is the Faraday constant. The advantages of the potentiometric method are that it is non-destructive, the equipment is relatively cheap and can achieve a high reading rate (higher than 1 hertz). Nevertheless it requires regular calibration due to electrode drift (up to 0.02 pH units per day (Seiter and DeGrandpre, 2001)), making autonomous measurements problematic. Furthermore, potentiometric sensors are susceptible to electromagnetic interferences and there are various problems with both

residual liquid junction potentials and variations in asymmetry potential (Dickson, 1993). As a result of the ubiquitous experimental problems, potentiometric pH measurements will rarely achieve an accuracy of better than 0.01 pH units (Dickson, 1993). Potentiometric pH sensors are therefore an option when studying pH variations larger than 0.01 pH units (e.g. (Le Bris et al., 2005)), but are not suitable for ocean acidification observations.

3.2.2.2. ISFET sensors

A new type of Nernstian sensor using ion-sensitive field-effect transistors (ISFET) could overcome some of the issues encountered with traditional potentiometric pH measurements, and be applicable to *in situ* pH and pCO_2 measurements (Shitashima et al., 2008;Martz et al., 2010). The ISFET is a semiconductor made of p-type silicon coated with SiO_2 without a metal gate electrode over the conduction channel. The ion sensing layer is a thin Si_3N_4 coating on the conduction channel. The surface charge at the interface of this coating with the solution is controlled by the solution pH and will determine the strength of the electric field in the conduction channel of the FET. The pH is therefore obtained by the measurement of the voltage between the reference electrode and the sensing layer. A Nernstian slope is verified with the use of standard pH buffers in a similar manner as with the classical glass electrode based sensor. The advantage of the ISFET sensor includes reduced drift and noise due to stray currents as a result of the lower impedance compared to a glass electrode. Martz and co-workers (Martz et al., 2010) tested the commercially available Honeywell Durafet® system for pH measurements of surface seawater. They obtained very promising results with a stability better than 0.005 pH units over periods of weeks to months and a short term precision of ±0.0005 pH units over several hours. These workers showed the great potential of the ISFET based sensor for *in situ* applications at 1 atm. An oceanographic instrument is now commercially available (SeaFET Ocean pH Sensor, Satlantic LP), and the ISFET sensors are becoming more commonly used in experimental laboratory studies and on moorings. However, further work is required on the performance of the reference electrode and the chip packaging for deployment at depth. In addition, the stability of the sensor during long-duration oceanic deployments needs to be assessed. In future, an ideal *in situ* system for long term deployment may be formed by a combined ISFET and spectrophotometric sensor system which provides high frequency ISFET measurements with additional lower frequency high precision and accuracy spectrophotometric analyses.

3.2.3. Luminescence method

Luminescence based sensors use optodes with indicator dyes fixed in a polymer. The pH fluorosensors are based on the variation of the fluorescence of the indicator dye with hydrogen ion concentration. The most promising approach for seawater pH measurement is formed by time domain Dual-Lifetime Referencing (t-DLR) which combines ratiometric and lifetime measurements (Liebsch et al., 2001). It uses the fluorescence intensity ratio of two luminescent indicators: one indicator is pH sensitive and has a short luminescence lifetime and the other is not pH sensitive and has a longer lifetime. The advantages of the fluorescence method are its high sensitivity and selectivity. Fluorosensors can also be used for simultaneous detection of several analytes (e.g. oxygen) (Stich et al., 2010). Despite important improvements in analytical luminescent techniques, current pH luminescence based sensors are still subject to a range of issues such as cross sensitivity to ionic strength and temperature, fluorescence foil bleaching and sensitivity to ambient light. The best precision obtained with a pH optode is 0.00064 pH units at pH 7.9 in 35‰ artificial seawater containing 10 mM TRIS-HCL buffer (Larsen et al., 2011), with the system operational in the range between pH 6 and 9. This pH optode sensor was calibrated against a potentiometric pH electrode which had an accuracy of ± 0.02 pH units after calibration with standard buffers (pH 4, 7, and 10, NBS) (Larsen et al., 2011).

3.2.4. Spectrophotometric method

The spectrophotometric pH determination is based on the addition to a seawater sample of an indicator dye, which changes color with pH. The dye is an acid-base compound with a second dissociation constant that should be close to the pH of seawater. The solution pH (i.e. indicator and sample mix) can be expressed as a function of the acid dissociation constant ($pK_{ind} = -\log_{10}(K_{HI^-})$) and the concentration of the protonated (HI^-) and the unprotonated (I^{2-}) forms of the indicator:

$$pH = pK_{ind} + \log_{10}([I^{2-}]/[HI^-]) \qquad (3.3)$$

The acid and base forms of the indicator have different absorption spectra. This allows the determination of the ratio of concentration of the indicator species by multi-wavelength absorption measurements:

$$\frac{[I^{2-}]}{[HI^-]} = \frac{A_1/A_2 - \varepsilon_1^{HI^-}/\varepsilon_2^{HI^-}}{\varepsilon_1^{I^{2-}}/\varepsilon_2^{HI^-} - A_1/A_2\,\varepsilon_2^{I^{2-}}/\varepsilon_2^{HI^-}} \qquad (3.4)$$

A_1 and A_2 refer to the absorbance at wavelengths 1 and 2. $\varepsilon_\lambda(I^{2-})$ and $\varepsilon_\lambda(HI^-)$ are the extinction coefficients at wavelength λ of the base (I^{2-}) and acid (HI^-) forms of the dye, respectively.

The pH can therefore be calculated from the absorbance ratio of the unprotonated and protonated forms using equation 5 (Robert-Baldo et al., 1985):

$$pH = pK_{ind} + log_{10}\left(\frac{A_1/A_2 - \varepsilon_1^{HI^-}/\varepsilon_2^{HI^-}}{\varepsilon_1^{I^{2-}}/\varepsilon_2^{HI^-} - A_1/A_2\,\varepsilon_2^{I^{2-}}/\varepsilon_2^{HI^-}}\right) \quad (3.5)$$

which can be rewritten as

$$pH = pK_{ind} + \log_{10}((R-e_1)/(e_2-Re_3)) \quad (3.6)$$

with $R=A_1/A_2$, $e_1=\varepsilon_1(HI^-)/\varepsilon_2(HI^-)$, $e_2=\varepsilon_1(I^{2-})/\varepsilon_2(HI^-)$ and $e_3=\varepsilon_2(I^{2-})/\varepsilon_2(HI^-)$.

The extinction coefficients and the pK_{ind} are functions of temperature and salinity.

The advantage of the spectrophotometric pH method is that it is not prone to drift as is the case with the potentiometric method. Because the ratio of the concentrations of the two indicator forms is used to calculate pH, the exact total concentration of the indicator is not required to determine the pH of the sample mixed with the indicator. In case the exact indicator concentration is needed, this can be obtained from the absorbance measured at the isosbestic wavelength (λ_{iso}) at which the extinction coefficients for both protonated and unprotonated forms are equal. Absorbance at the isosbestic wavelength is dependent on the total indicator concentration only. The spectrophotometric pH measurements are therefore inherently calibrated.

The pH indicator dye needs to be characterized for temperature, pressure and ionic strength dependence, which should take place in the laboratory prior to instrument deployment. Variations in the background absorption of seawater samples, and changes to the optical cell, the strength and spectrum of the light source and the sensitivity of the detector can all lead to drift and inaccuracies of the pH measurements. However, these effects are typically small (<0.004 pH (Bellerby et al., 2002)) and can be mitigated by periodic reference measurements of the light in the absence of the indicator (see 5.5 Baseline correction). The precision and long term reproducibility of spectrophotometric pH measurements are potentially better than 0.001 pH units (see table 1).

3.3. Spectrophotometric pH systems

3.3.1. pH systems

The different components of an automated spectrophotometric pH system are presented in Figure 3.1. The seawater sample and the indicator dye are pumped into the system and mixed

before detection in the absorption cell. The light transmitted in the absorption cell is recorded by a photo-detector and the obtained data is converted into absorption values which are used for the pH calculations.

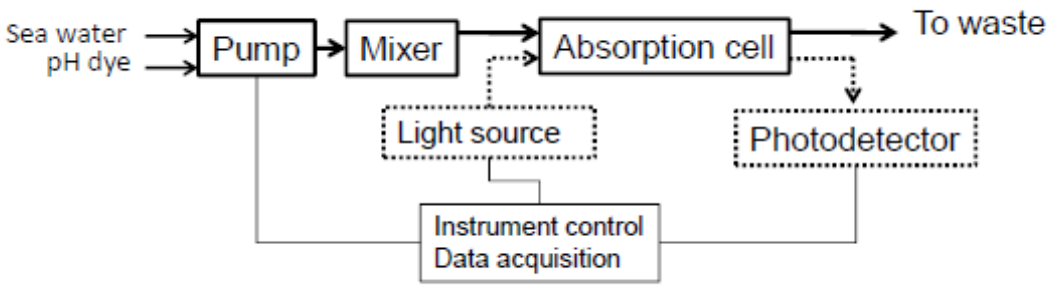

Figure 3.1: Schematic diagram of an automated spectrophotometric pH system.

Most automated spectrophotometric pH systems in use by researchers are deployed at sea on ships for surface water measurements ((Aßmann et al., 2011a;Bellerby et al., 1995;Bellerby et al., 2002;DelValls, 1999;Mosley et al., 2004;Ohline et al., 2007;Tapp et al., 2000;Wang et al., 2007;Assmann et al., 2011), but recently, successful *in situ* deployments have been reported (Kaltenbacher et al., 2000;Liu et al., 2006;Martz et al., 2003;Nakano et al., 2006;Seidel et al., 2008). Some of the automated spectrophotometric systems currently used are summarised in table 1 and reviewed in the following paragraphs. The accuracy reported in Table 3.1 corresponds to either the discrepancy of a pH measurement by the reported instrument with a measurement by a bench top spectrophotometer (Aßmann et al., 2011b;Friis et al., 2004;Liu et al., 2006;Nakano et al., 2006;Seidel et al., 2008;Wang et al., 2007;Aßmann et al., 2011a;Assmann et al., 2011), the square root of the sum of the squares of the estimated inaccuracies (Bellerby et al., 2002) or the discrepancy between measured and certified values established by the analysis of certified TRIS buffer (underlined values (Assmann et al., 2011)).

Table 3.1: Figures of merit of spectrophotometric pH systems. Underlined values correspond to the discrepancy between measured and certified values for the analysis of certified TRIS buffer. Precision and accuracy are given in pH units.

A. Automated ship-board pH systems				
Systems	Bellerby et al. 2002 (Bellerby et al., 2002)	Friis et al. 2004 (Friis et al., 2004)	Wang et al. 2007 (Wang et al., 2007)	Aßman et al. 2011 (Aßmann et al., 2011a)
Precision	<0.001	0.0032	0.0008	0.0012/<u>0.0007</u>
Accuracy	0.004	not reported	0.0012 ± 0.0042	0.0018/<u>0.0076</u>
Frequency (sample.h^{-1})	20	not reported	7	60

B. Automated *in situ* pH systems			
Systems	SEAS-pH (Liu et al. 2006 (Liu et al., 2006))	(Nakano et al. 2006 (Nakano et al., 2006))	SAMI-pH (Seidel et al. 2008 (Seidel et al., 2008))
Application	Deployed to 250 m on rosette frame	Deployed to 1000 m on rosette frame	Moored/ deployed at 4 m deep
Precision	0.0014	0.002	±0.0007
Accuracy	not reported	not reported	+0.0017
Frequency (sample.h^{-1})	1800	360	15

3.3.2. Fluid propulsion

Most of the reported pH systems use two pumps: one for the seawater sample and the other for the indicator solution (Bellerby et al., 1995;Kaltenbacher et al., 2000;Tapp et al., 2000). Alternatively, one single pump can be used with a system of valves controlling the selection of liquids (Martz et al., 2003). Pumps have also been replaced by a gravity based fluid propulsion system (Bellerby et al., 2002). Valve control simplifies the routing and pumping systems, but may

result in lower accuracy of the pumped volumes and an increase in dead volume in the flow system. A range of pump types has been reported, including solenoid (Seidel et al., 2008), peristaltic (Liu et al., 2006), piston (Friis et al., 2004) and syringe pumps (DelValls, 1999). The choice of pump will depend on sample volume, accuracy of the required volume delivery and whether the flow has to be continuous. If continuous flow is required, peristaltic pumps provide a constant mean flow with a superimposed near-sinusoidal variation, and two pumps (sample and indicator pumps) can be readily synchronized. Syringe pumps provide the best accuracy in volume delivery, and can also be used for mixing of the sample and indicator dye (DelValls, 1999). Continuous fluid flow is possible using syringe pumps with two parallel pumping setups (Ogilvie et al., 2011). A key consideration for *in situ* pH systems is the size of the pump and its power consumption. Different types of micro-scale pumps have recently been developed and will allow for miniaturisation of pH systems (Laser and Santiago, 2004). At present, small peristaltic pumps are certainly most appropriate for *in situ* applications.

3.3.3. The absorption cell

Most benchtop pH systems use 100 mm pathlength cuvettes and relatively low indicator concentrations of $1x10^{-6}$ - $1x10^{-5}$ $mol.kg^{-1}$, in order to minimize sample pH perturbations due to the indicator addition (Clayton and Byrne, 1993;Friis et al., 2004;Ohline et al., 2007). Systems with shorter pathlengths of 50 mm (Bellerby et al., 2002) or 10 mm (Tapp et al., 2000) have been used successfully but require a higher indicator concentration to achieve a similar precision as the 100 mm pathlength systems. Increasing the indicator concentration requires consideration of the associated pH perturbations as discussed in 3.5. Corrections. The minimum pathlength required to obtain a perturbation smaller than one milli-pH depends on the pH difference between the indicator and seawater sample, and on the indicator to sample mixing ratio. The latter is determined by the apparent extinction coefficients of the pH system, and the concentration of indicator stock solution required to obtain appropriate absorption readings for high quality pH measurements. The flowcells and cuvettes used in pH systems include standard cylindrical glass cells, custom made Polyvinyl Chloride (PVC), polyethylene, Polyether Ether Ketone (PEEK) or other polymeric cells. Some reported systems use liquid core waveguides (LCW) (Liu et al., 2006), which display excellent optical properties and can be as long as 2 m. However, high precision can be achieved with 100 mm pathlength cells (DelValls, 1999), and the standard polymeric cells are more rugged, less expensive and less prone to lining with bubbles or contaminants compared with the LCWs. The PEEK flowcells are also easier to mount and maintain compared with the LCWs, and do not require the use of surfactants to minimize bubble problems (Liu et al., 2006). Polymeric cells are therefore attractive for *in situ* applications.

The presence of bubbles is a recurrent issue in spectrophotometric flow systems. Bubbles can cause significant interferences in fluid flow, mixing and spectrophotometric measurements. Care should be taken to limit potential sources of bubbles (e.g. fluid inlets and connectors) in the system. As bubbles will often advertently occur in flow systems, it is key to design the systems in such a way as to minimise the possibility for bubbles to get stuck, which often takes place at sharp angles and rough surfaces. The bubble problems are greatly minimised when channel dimensions are reduced, internal surface roughness is reduced, and system integration is increased in order to reduce the number of connections. These features are typically found in lab-on-chip sensors and lead to prevention of bubble formation. In these systems, the bubbles that are acquired from environmental samples are readily flushed through the system and cause only temporary disturbances.

3.3.4. Mixing of indicator with seawater sample

The reported seawater to indicator mixing ratios vary between systems from 10:1 to 1000:1; an optimal sensitivity is obtained with absorbance readings in the range 0.4 to 1 (Dickson et al., 2007). Mixing can be achieved by active or passive approaches. Active methods include the use of syringe pumps (Clayton and Byrne, 1993), or a magnetic stirrer to mix the indicator with the sample (Bellerby et al., 2002). Passive methods use a mixing coil or an in-line static mixer, and mixing is often enhanced by injecting the indicator in the sample stream (Bellerby et al., 1995;Friis et al., 2004;Liu et al., 2006;Martz et al., 2003;Seidel et al., 2008;Wang et al., 2007). Specifically designed mixing joints enhance the mixing process (Tapp et al., 2000;Ohline et al., 2007), but may result in longer flushing times due to dead volumes in corners and joints. The advantage of the passive mixing systems is that they require only a negligible increase in power consumption (due to additional pressure drops across the mixers). However, homogenisation of the sample-indicator mixture can be a challenge given the high mixing ratios required for the spectrophotometric pH measurements.

3.3.5. Light Source

High light intensities are required at the absorbance maxima of the indicator. High intensities at the isosbestic point and a non-absorbing wavelength will allow corrections for pH perturbations and light variations (see 3.5. Corrections). The most commonly used light source is a tungsten halogen lamp. However, these have low intensities in the wavelength region of 430 nm, required for all spectrophotometric pH determinations. It is possible to improve the light spectrum with a combination of optical filters (Martz et al., 2010), but this leads to a more complex system. Another approach to improve the spectrum at low wavelengths involves the use of a deuterium

lamp in addition to the tungsten lamp. Combined halogen and deuterium light sources are commercially available, but are expensive. Furthermore, halogen lamps are fragile, power demanding and relatively large, which makes them less suitable for shipboard or *in situ* applications. Averaging of several spectra constitutes a simple way to improve the signal to noise ratio and mitigates the effects of low power at the lower wavelength. However, bias in the mean absorbance due to potentially strong absorbance fluctuations can induce an error in the final pH value.

The use of Light Emitting Diodes (LEDs) provides an excellent alternative to the tungsten halogen lamp. LEDs are widely used in modern spectrometry as light source because they are cheap, compact, extremely stable, typically monochromatic, have low power requirement and a long life-time with minimal intensity degradation over their life span. The light spectrum of LEDs has a full width at half maximum (FWHM) of typically 25 nm, which is comparable to bandwidths achieved by the combination of wideband sources and interference type optical filters. Therefore, it is possible to carry out photometric measurements without the use of wavelength discriminating devices (Hauser et al., 1995).

3.3.6. The signal detector

Light absorbances at multiple wavelengths can be determined using a scanning spectrophotometer (McElligott et al., 1998), or a diffractive element (such as an optical grating) and a detector array (such as a charge couple device (CCD) array) as used in CCD spectrophotometers. Double-beam spectrophotometers are recommended because of the high sensitivity and precision (DelValls, 1999) obtained by the simultaneous measurement of both the source and transmitted light. These devices are expensive and have a high power consumption, whilst *in situ* instruments for pH measurements need to be rugged and compact. The photodiode array spectrophotometer is more appropriate for *in situ* operations and their rapid acquisition of a broad wavelength region allows repeated spectral measurements, which improves the signal to noise ratio. The limited wavelength resolution (because of large pixel size), high dark current and poor signal to noise ratio at low optical powers are the principal limitations to the portable versions of photodiode array systems. It is possible to perform multiple wavelength measurements of pH indicator absorption spectra without using diffractive spectrometry. For example Seidel et al. (Seidel et al., 2008) used three silicon photodiodes to detect and discriminate absorption spectra from a pH indicator. The transmitted light was divided and then filtered to isolate optical power in three narrow wavelength bands of interest. Photodiodes are extremely versatile, low cost and have been employed in various configurations such as in

detectors of flow injection analysis systems, separation systems and probe photometers (O'Toole and Diamond, 2008). They are robust, have a rapid response and wide linear range (3-4 orders of magnitude better than phototransistor). Simple spectral separation and photodiode detection is therefore attractive for miniaturized *in situ* devices.

3.3.7. Temperature

Seawater pH analysis is very sensitive to temperature variations. Sample temperature must therefore be measured. pH measurements are often made under carefully controlled temperature conditions; typically between 20-25°C (Friis et al., 2004). Alternatively, pH is measured at *in situ* temperature (Nakano et al., 2006), or simply at measurement temperature (i.e. without temperature control) (Bellerby et al., 1995;Bellerby et al., 2002). The advantage of measuring pH at a fixed temperature is that the indicator solution only needs to be characterized at one temperature. The instrument's components (in particular the detector) may also be more stable when operated at a constant temperature. However, enhanced bubble formation may occur in the sample stream if cold seawater is warmed and this will then require the inclusion of a debubbler upstream of the optical cell (Friis et al., 2004). In addition to flow and measurement problems, bubble formation may also cause outgassing of CO_2 which would change the sample pH. The thermostatting of the pH measurements leads to a more complex and expensive system with higher power consumption, but it also requires correction of the measured pH back to *in situ* seawater temperatures. The best option is to measure directly at *in situ* temperatures and avoid errors induced by temperature corrections.

It should be noted that despite the high sensitivity of pH measurements to temperature, the accuracy of the temperature measurement is not so critical. An error in the temperature measurement of a sample is partially cancelled out by the temperature dependency of the indicator parameters. Indeed, an unrecognized temperature error of 0.1°C will only lead to an error of about 0.001 pH units when using Thymol Blue indicator.

3.4. Sulphonephtalein indicator

The optimum pH range for an indicator dye is determined by its pK value, and the extinction coefficient ratios of the acidic and basic indicator forms (Dickson et al., 2007;Dickson and Goyet, 1994). The pK of the indicator should be comparable to the expected pH of the indicator-seawater solution so that $pK-1 \leq pH \leq pK$ (Byrne et al., 1988). The pH indicator Thymol Blue (TB) ($pK \approx 8.6$ (Byrne, 1987)) has been proposed as optimal for the narrow pH range encountered in surface seawaters (open-ocean surface water pH range between 7.95 and 8.35 (Feely et al., 2009)), whereas meta-cresol purple (mCP) ($pK \approx 8.0$ (Clayton and Byrne, 1993)) has been proposed for the

pH range encountered in typical surface to deep ocean profiles. The equations for pH calculations involving the different indicator dyes are presented in Table 3.2. It is recommended that every new batch of indicator is characterized, despite the availability in the literature of the indicators' extinction coefficients as a function of temperature, salinity (Clayton and Byrne, 1993;Gabriel et al., 2005;Liu et al., 2011;Mosley et al., 2004;Zhang and Byrne, 1996) and even pressure (Hopkins et al., 2000). This is particularly important in case the indicator has not been purified to remove impurities (Yao et al., 2007). Liu and coworkers [41] observed discrepancies between measurements with purified and unpurified indicator of as much as 0.010 pH units at pH 7.4 and 0.018 pH units at pH 8.2. The apparent extinction coefficients are also dependent on the detection system and measurement procedure, and hence need to be determined for each instrument. The apparent extinctions coefficients are influenced by the wavelength resolution of the detector and the spectral slope of the light source within the resolution window. Published values are generally obtained with scanning double-beam spectrometer using a detector with relatively narrow slit-width. The use of the published values obtained with instruments using larger wavelength resolutions and light sources with shaped spectra will lead to inaccuracies in the measurements. In case the indicator cannot be characterized for a particular system, it is desirable to purify the indicator and thus ensure that the indicator used is accurately characterized by literature coefficients (Seidel et al., 2008). Inaccuracies due to source spectral slope and finite detector resolution can then be reduced by calculating their impact through simple absorption models (Floquet et al., 2011).

The indicator extinction coefficients are determined by absorption measurements in acidic and basic solutions, conditions which ensure that only one form of the indicator (HI^- or I^{2-}) is present. The coefficients at specific wavelengths are obtained using the Beer-Lambert law from absorption data and known indicator concentrations. The indicator acid formation constant is determined by absorption measurements in a solution of known pH (e.g. TRIS buffer). Liu and coworkers (Liu et al., 2011) rearranged equation 6 in order to reduce the number of parameters to be measured in the basic buffer to one (e_3/e_2) and in the acid buffer to one (e_1). This approach reduces the number of parameters to be determined in the indicator characterization process.

To allow future corrections of pH data when refined indicator characterizations are available for a wider range of conditions, it is advisable to archive the following data (Clayton and Byrne, 1993): raw absorbance measurements, volume of indicator added, seawater salinity, temperature of measurements, indicator concentration, absorption ratio, pH perturbation, algorithms used to calculate R (corrected) and sample pH, and documentation of quality control.

Table 3.2: Equations for pH calculations (pK and extinction coefficient) reported in literature.

Publication	Indicator	Extinction coefficient ratio						pK_2	Operating ranges	
		λ_{Hlind}^{max}	λ_{lind-}^{max}	λ_{iso}	e_1	e_2	e_3		Salinity	Temperature
Robert-Baldo et al. 1985	Phenol Red	433	558	479.7	0.0038	2.6155	0.1234	-4054.8374/T + 116.6037 - 38.6645log(T) + 0.004(35-S) -log(1-0.00106S)	33≤S≤37	0≤T(°C)≤35
Zhang & Byrne 1996	Thymol Blue	435	596	495	-0.00132 + $1.6x10^{-5}T$	7.2326 - 0.0299717T + $4.6x10^{-5}T^2$	0.0223 + 0.0003917T	4.706S/T + 26.3300 - 7.17218log(T) - 0.017316S	30≤S≤40	5≤T(°C)≤35
Mosley et al. 2004	Thymol Blue							$9.1427 - 0.3105S^{1/2} + 0.0783S - 0.01135S^{3/2} + 0.000684S^2$	0≤S≤40	T=25°C
Mosley et al. 2004	meta-Cresol Purple							$8.6353 - 0.3238S^{1/2} + 0.0807S - 0.01157S^{3/2} + 0.000694S^2$	0≤S≤40	T=25°C
Hopkins et al. 2000	Thymol Blue	435	596		0.0035	2.386 - $(2.7\ 10^{-6})P$	0.139 + $(6.6x10^{-6})P$	$-\log(pK_2^0) - (2.99(\pm0.02)\ 10^{-4})P + (3.3(\pm0.3)\ 10^{-8})P^2$	0≤P≤40 bar	T=25°C
					e_1	**e_3/e_2**		**$-\log(K_2e_2) = a + (b/T) + c\ln(T) - dT$**		
Liu et al. 2011	meta-Cresol Purple	434	578		-0.007762+ $4.5174x10^{-5}T$	-0.020813+ $2.60262x10^{-4}T$+ $1.0436x10^{-4}(S-35)$		a = -246.64209 + 0.315971S + 2.8855 x $10^{-4}S^2$; b = 7229.23864 - 7.098137S - 0.057034S^2; c = 44.493382 - 0.052711S; d = 0.0781344;	20≤S≤40	25≤T(°C)≤35

3.5. Corrections

Several corrections need to be applied to pH values obtained using spectrophotometric techniques.

3.5.1. Baseline correction

Changes in the instrumental response due to optical source fluctuations and movement of optics can be corrected using parallel measurements of the light signal on a second (slave or reference) channel without cuvette (Friis et al., 2004). However, a second channel is not necessary if regular reference light measurements are made before addition of the indicator at a higher rate than any periodic fluctuation or variation in the source or optics.

3.5.2. Transparency correction

Light scatter due to the presence of particles in seawater is detected through intensity measurements at a non-absorbing wavelength of the indicator dye, usually between 700 and 750 nm. Some systems also use the transparency correction to correct for baseline fluctuations assuming that instrumental response fluctuations are the same at every wavelength (Husheer, 2001).

3.5.3. Corrections of pH to *in situ* conditions

When measurements are conducted at a convenient constant standard temperature and pressure, it is necessary to correct the pH data back to *in situ* conditions at which the sample was collected. The most reliable way to correct for temperature changes is to use the measured value of pH with another carbonate variable such as TA (or DIC) (Hunter, 1998;Millero, 2007) to calculate DIC (or TA). DIC and TA are not temperature dependent and can be used to calculate pH at the *in situ* oceanic temperature using thermodynamic relationships. If no second carbonate chemistry variable has been determined, TA can also be calculated from salinity data using the equations from Bradshaw and coworkers (Bradshaw et al., 1981) (TA=660+47.6S). Hunter (Hunter, 1998) obtained a resulting error smaller than 0.0002 pH units using this method.

3.5.4. Correction for indicator-induced pH perturbation:

The correction for indicator-induced pH perturbation is made by measurements of pH at several indicator concentrations. The indicator concentration range is obtained through sequential addition of the indicator to the sample (Clayton and Byrne, 1993;Zhang and Byrne, 1996;Friis et al., 2004;Bellerby et al., 2002) or a dilution/dispersion curve of the indicator aliquot in the sample after passing through a static mixer (Seidel et al., 2008;Martz et al., 2003). A linear relationship is observed between pH and the indicator concentration in the sample, and correct sample pH is

obtained by linear extrapolation to an indicator concentration equal to zero. Similarly, Clayton and Byrne proposed an empirical approach where a pair of additions of dye is only made once per series of seawater samples with different pH (Clayton and Byrne, 1993;Dickson et al., 2007). A relationship is obtained for the change in the measured absorbance ratio ΔR between the two additions, the volume added V and the absorbance ratio R_1 measured after the first addition:

$$\Delta R/V=a+bR_1 \qquad (3.7)$$

The absorbance ratio R is then corrected using the following equation:

$$\mathrm{Rcorrected}=R-V(a+bR) \qquad (3.8)$$

Hunter and Macaskill, and Chiercici and co-authors (Hunter and Macaskill, 1999;Chierici et al., 1999) proposed theoretical methods to correct for dye additions but this requires the use of the same seawater to indicator dye mixing ratio as the one used in their work (i.e. 1:50 (Hunter and Macaskill, 1999) or 1:100 and 1:500 (Chierici et al., 1999)). Furthermore, an accurate knowledge of the dilution factors is required which can be problematic in miniaturized systems using less accurate pumps. The pH of the indicator stock solution should be adjusted to the expected seawater pH in order to minimize the indicator-induced perturbations. Sample dilution by the indicator solution could also alter the sample pH (Martz et al., 2003) as it decreases DIC and TA. The indicator stock solution should therefore be prepared at a sufficiently high concentration (typically 2 mM) in order to minimize sample dilution effects and to optimize the optical detection.

3.6. Precision and accuracy

3.6.1. Precision

The precision reported in literature corresponds to the standard deviations of repetitive measurements. For ocean acidification observations, the precision should be better than the average annual decrease of 0.002 pH units in surface oceans (Byrne et al., 2010a;Dore et al., 2009b;Gonzalez-Davila et al., 2010).

3.6.2. Accuracy

The accuracy of pH measurements is more difficult to determine as the pH method determines the absorption ratio of the acidic and basic forms of the indicator dye and thus requires no calibration. The accuracy of the method depends on the accuracy of the indicator pK and molar absorptivity values, the accuracy of the temperature and salinity measurements, and the calibration and sensitivity of the spectrometers.

The main sources of inaccuracy involve the uncertainty in the pK value of the indicator and the error in the absorption measurements at the wavelength corresponding to the absorption of the basic form of the indicator. TRIS buffer is used to determine pK, hence the uncertainty in the pK value cannot be smaller than the uncertainty in the TRIS buffer used. The accuracy of the TRIS buffer can be as good as 0.002 pH units if prepared carefully (DelValls and Dickson, 1998). Certified TRIS buffers are currently provided by the laboratory of Prof. A. Dickson, Scripps Institution of Oceanography at San Diego, and have an overall uncertainty of 0.004 (Certificate of Analysis, e.g. batch 8). Care should be taken when comparing performance metrics from the literature: often the accuracies reported are actually the discrepancies observed between direct instrument measurements and discrete samples measured with a bench top spectrophotometer (Friis et al., 2004;Liu et al., 2006;Nakano et al., 2006;Seidel et al., 2008;Wang et al., 2007). For example, inaccuracy due to the use of biased extinction coefficients resulting from impurities in the indicator will not be noted by such a comparison. Accuracy can be assessed by measuring the pH of TRIS buffer and comparing results to theoretical pH calculated with an accuracy of 0.005 pH units from the following equation (DelValls and Dickson, 1998):

$$\mathrm{pH(T)}=(11911.08\text{-}18.2499S\text{-}0.039336S^2)/T + (\text{-}366.27059 + 0.53993607S + 0.00016329S^2) + (64.52243\text{-}0.084041S)\log_{10}(T) - 0.11149858T \quad (3.9)$$

where T is the temperature (in Kelvin) and S is the salinity.

Certified TRIS buffer should be used in order to assess sensor performance. This is critical for comparison of data obtained by different sensors. However the use of TRIS buffer does not enable coverage of the pH and temperature range encountered in the oceans. A combination of TRIS buffer measurements along with an estimation of the system inaccuracies covering the natural range of temperature and pH would therefore be advisable. It should be noted that the TRIS buffer is less affected by pH perturbations due to indicator additions compared with seawater and hence does not allow us to check the adequacy of the indicator pH correction method. Comparisons with pH calculated from other carbonate parameters will provide further information on the system accuracy, particularly on its temperature dependence and on the applied indicator dye pH correction. However these comparisons are dependent on the chosen carbonate system dissociation constants and the DIC/TA ratios (Millero, 2007).

3.7. Microfluidic pH system

Current pH systems are not suitable for a widespread application on *in situ* platforms and therefore smaller and more rugged instruments are required. The next generation pH systems will use simple micro-fluidic designs with low power and reagent consumption. Such a pH micro-sensor featuring high precision and accuracy is being developed at the National Oceanography Centre, Southampton. The implementation of the spectrophotometric method on a robust microfluidic flow cell is a key step toward the targeted micro-sensor. A schematic of this microfluidic pH system is presented figure 3.2.

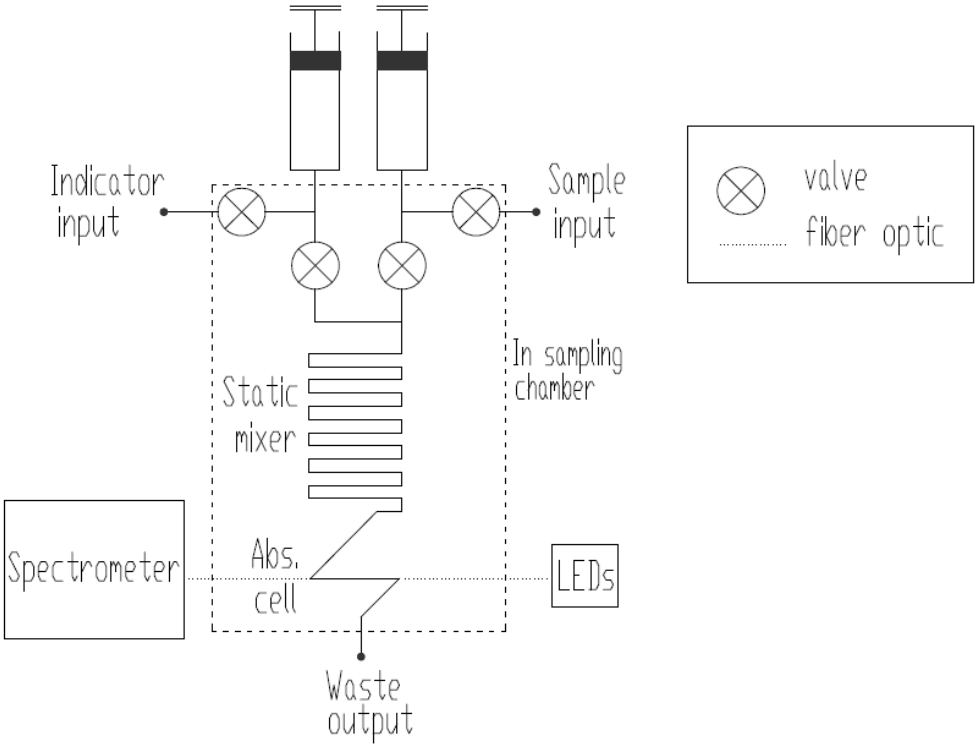

Figure 3.2 : Schematic of the microfluidic pH system. The seawater sample (400 µL) and the indicator (5 µL) are pumped by two individual syringe pumps and mixed in the flow cell using a static mixer prior to reaching the absorption cell. Light from LEDs is transmitted through the absorption cell and measured by a miniature spectrophotometer. The measurement is made close to in situ temperature (+0.2 °C) in a sampling chamber which has a continuous flow of the ship's underway seawater supply. The processing and analysis of one sample takes 6 min.

The microfluidic flow cell comprising the absorption cell and the static mixer is manufactured in poly(methyl methacrylate) (PMMA) (Ogilvie et al., 2010);(Floquet et al., 2011). Fluidics are controlled by four micro-inert valves (LFNA1250125H, Lee Products Ltd., UK) directly mounted on the chip and fluid propulsion is conducted using two syringe pumps (Harvard Apparatus

Nanomite, Kent, UK). The 10 mm absorption cell has a volume of 5 µL and is connected to the light source and detector by two optical fibres (600 µm diameter, Thorlabs, USA). The light source is a tri-colored LED with wavelengths of 435 nm and 596 nm corresponding to the absorption maximum of the Thymol Blue indicator forms HI^- and I^{2-}, and 750 nm to monitor the sample turbidity. A linear array photodiode spectrophotometer (HR4000, Ocean Optics) is used as detector. The gradient of the indicator concentration observed at the end tail of the dilution/dispersion curve of the indicator aliquot in the sample stream after passing through a static mixer is used to quantify the perturbation of the sample pH by the indicator (Martz et al., 2003;Seidel et al., 2008).

The performance of the system has been evaluated by analyzing certified TRIS buffer at 25.02±0.01 °C. The short term precision was 0.0009 pH unit (n=20) and a discrepancy of 0.0018 pH unit was observed between the measured and the certified value (for more details see Chapter 4.2.5 System precision and accuracy). The long term precision of the system has not yet been evaluated.

The pH sensor has been deployed on RRS *Discovery* cruise D366 as part of the UK Ocean Acidification Research Programme. The automated pH system was operated continuously over a period of a month on an underway seawater supply. Measurements were only interrupted for system performance checks and maintenance. Seawater surface pH data collected during the first week of this cruise are presented in figure 3. The pH data will be corrected to *in situ* temperature using total alkalinity data (Hunter, 1998), but this correction will be minor as the difference between measurement and temperature was only +0.2°C (see Chapter 5.3.2. Distribution and Quality of the carbonate data). The pH observed during the first week of the cruise ranged between 7.974 and 8.118. The highest pH values were observed to the north west of Ireland, whilst sailing through waters with high phytoplankton biomass and primary productivity, resulting in the uptake of DIC. Lowest pH values were observed in the northern Irish Sea as a result of DIC production through remineralisation of organic matter.

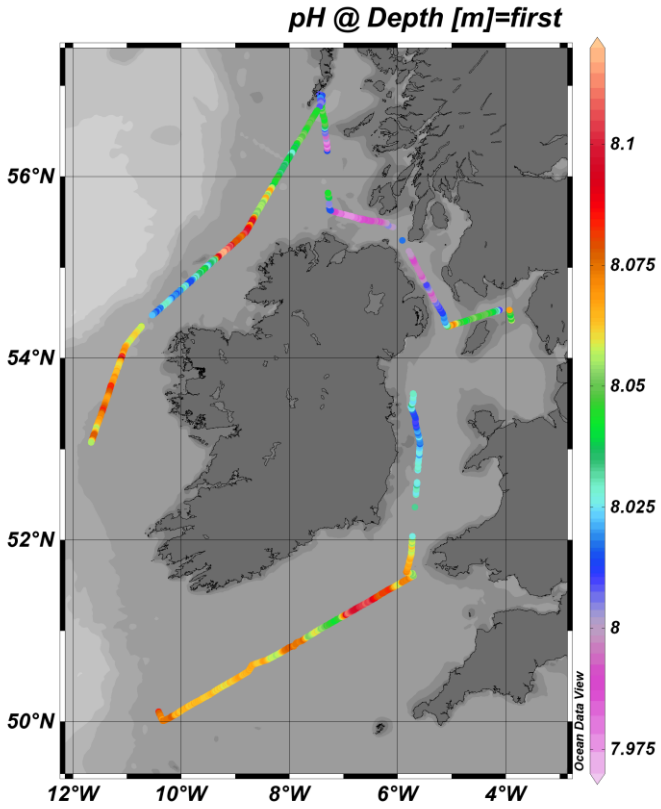

Figure 3.3: Map of surface pH determined during the first week of cruise D366 (June 6 to 13, 2011).

3.8. Conclusion and future directions

The spectrophotometric pH technique is capable of the high-quality measurements required for ocean acidification observations. Spectrophotometric pH systems with high precision and accuracy have been deployed on ships and recently also *in situ* on moorings. Systems for pH measurements have improved in recent years and production costs have come down, but they remain complex and relatively expensive, in particular the optical components. The most suitable components for autonomous *in situ* instruments are a polymeric cell, a static mixer, micro-pumps, LEDs and photodiodes. Ideally, the absorption cell should be 100 mm long in order to minimize the indicator dye addition and consequent sample pH perturbation, but the mixing achievable with the passive mixer will ultimately determine the required path length. Readily available Lab-on-Chip technologies have allowed the development of robust and low cost sensors with low power and reagent consumption. The development of a pH micro-sensor with high accuracy and precision is therefore now possible.The next generation spectrophotometric pH systems will use simple micro-fluidic designs coupled with LEDs and photodiodes.

Acknowledgements

This work is supported by SENSEnet, a Marie Curie Initial Training Network (ITN) funded by the European Commission Seventh Framework Programme, Contract Number PITN-GA-2009-237868. The Discovery D366 cruise was funded by the Natural Environment Research Council as part of the UK Ocean Acidification Programme (grant no. NE/H017348/1).

References

Aßmann, S., C. Frank, and A. Körtzinger (2011a), Spectrophotometric high-precision seawater pH determination for use in underway measuring systems, *Ocean Science*, *7*(5), 597-607.

Bates, R., and C. Culberson (1977), Hydrogen ions and the thermodynamic state of marine systems, *The fate of fossil fuel CO*, *2*, 45-61.

Bellerby, R. G. J., G. E. Millward, D. R. Turner, and P. J. Worsfold (1993), Approaches to the continuous monitoring of seawater pH and its role in the global carbon cycle, *TrAC Trends in Analytical Chemistry*, *12*(9), ix-ix.

Bellerby, R. G. J., D. R. Turner, G. E. Millward, and P. J. Worsfold (1995), Shipboard flow injection determination of sea water pH with spectrophotometric detection, *Analytica Chimica Acta*, *309*(1-3), 259-270.

Bellerby, R. G. J., A. Olsen, T. Johannessen, and P. Croot (2002), A high precision spectrophotometric method for on-line shipboard seawater pH measurements: The automated marine pH sensor (AMpS), *Talanta*, *56*(1), 61-69.

Bradshaw, A., P. Brewer, D. Shafer, and R. Williams (1981), Measurements of total carbon dioxide and alkalinity by potentiometric titration in the GEOSECS program, *Earth and Planetary Science Letters*, *55*, 99-115.

Byrne, R. H. (1987), Standardization of standard buffers by visible spectrometry, *Analytical Chemistry*, *59*(10), 1479-1481.

Byrne, R. H., G. Robert-Baldo, S. W. Thompson, and C. T. A. Chen (1988), Seawater pH measurements: an at-sea comparison of spectrophotometric and potentiometric methods, *Deep Sea Research Part A. Oceanographic Research Papers*, *35*(8), 1405-1410.

Byrne, R. H., S. Mecking, R. A. Feely, and X. Liu (2010), Direct observations of basin-wide acidification of the North Pacific Ocean, *Geophysical Research Letters*, *37*(2), L02601.

Caldeira, K., and M. E. Wickett (2005), Ocean model predictions of chemistry changes from carbon dioxide emissions to the atmosphere and ocean, *J. Geophys. Res*, *110*, 1-12.

Canadell, J. G., C. Le Quéré, M. R. Raupach, C. B. Field, E. T. Buitenhuis, P. Ciais, T. J. Conway, N. P. Gillett, R. Houghton, and G. Marland (2007), Contributions to accelerating atmospheric CO2 growth from economic activity, carbon intensity, and efficiency of natural sinks, *Proceedings of the National Academy of Sciences*, *104*(47), 18866-18870.

Chierici, M., A. Fransson, and L. G. Anderson (1999), Influence of m-cresol purple indicator additions on the pH of seawater samples: Correction factors evaluated from a chemical speciation model, *Marine Chemistry*, *65*(3-4), 281-290.

Clayton, T., and R. Byrne (1993), Spectrophotometric seawater pH measurements: total hydrogen ion concentration scale calibration of m-cresol purple and at-sea results, *Deep-sea research. Part 1. Oceanographic research papers*, *40*(10), 2115-2129.

Cullison-Gray, S. E., M. D. DeGrandpre, T. S. Moore, T. R. Martz, G. E. Friederich, and K. S. Johnson (2011), Applications of in situ pH measurements for inorganic carbon calculations, *Marine Chemistry*.

DelValls, T. A. (1999), Underway pH measurements in upwelling conditions: The California current, *Ciencias Marinas*, *25*(3), 345-365.

DelValls, T. A., and A. G. Dickson (1998), The pH of buffers based on 2-amino-2-hydroxymethyl-1,3-propanediol ('tris') in synthetic sea water, *Deep-Sea Research Part I: Oceanographic Research Papers*, *45*(9), 1541-1554.

Dickson, A. (1993), The measurement of sea water pH, *Marine Chemistry*, *44*(2-4), 131-142.

Dickson, A. (2010), The carbon dioxide system in seawater: equilibrium chemistry and measurements, *Guide to Best Practices for Ocean Acidification Research and Data Reporting*, *1*, 17–40.

Dickson, A., and J. Riley (1979), The estimation of acid dissociation constants in seawater media from potentionmetric titrations with strong base. I. The ionic product of water--Kw, *Marine Chemistry*, *7*(2), 89-99.

Dickson, A., and F. Millero (1987), A comparison of the equilibrium constants for the dissociation of carbonic acid in seawater media, *Deep Sea Research Part A. Oceanographic Research Papers*, *34*(10), 1733-1743.

Dickson, A. G., and C. Goyet (Eds.) (1994), *Handbook of methods for the analysis of the various parameters of the carbon dioxide system in sea water*.

Dickson, A. G., C. L. Sabine, and J. R. Christian (2007), Guide to best practices for ocean CO2 measurements, *PICES special publication*, *3*.

Doney, S. C. (2010), The growing human footprint on coastal and open-ocean biogeochemistry, *Science*, *328*(5985), 1512.

Doney, S. C., B. Tilbrook, S. Roy, N. Metzl, C. Le Quéré, M. Hood, R. A. Feely, and D. Bakker (2009), Surface-ocean CO2 variability and vulnerability, *Deep Sea Research Part II: Topical Studies in Oceanography*, *56*(8-10), 504-511.

Dore, J. E., R. Lukas, D. W. Sadler, M. J. Church, and D. M. Karl (2009), Physical and biogeochemical modulation of ocean acidification in the central North Pacific, *Proceedings of the National Academy of Sciences*, *106*(30), 12235.

Feely, R. A., S. C. Doney, and S. R. Cooley (2009), Ocean acidification: Present conditions and future changes in a high-CO2 world, *Oceanography*.

Floquet, C. F. A., V. J. Sieben, A. Milani, E. P. Joly, I. R. G. Ogilvie, H. Morgan, and M. C. Mowlem (2011), Nanomolar detection with high sensitivity microfluidic absorption cells manufactured in tinted PMMA for chemical analysis, *Talanta*, 235-239.

Friis, K., A. Körtzinger, and D. W. R. Wallace (2004), Spectrophotometric pH measurement in the ocean: Requirements, design, and testing of an autonomous charge-coupled device detector system, *Limnol. Oceanogr. Methods*, *2*, 126-136.

Gabriel, M. D., J. M. Forja, J. A. Rubio, and A. Gomez-Parra (2005), Temperature and salinity dependence of molar absorptivities of thymol blue: Application to the spectrophotometric determination of pH in estuarine waters, *Ciencias Marinas*, *31*(1 B), 309-318.

González-Dávila, M. (2010), The water column distribution of carbonate system variables at the ESTOC site from 1995 to 2004, *Biogeosciences*, *7*, 1995-2032.

Hansson, I. (1973), The determination of the dissociation constants of carbonic acid in synthetic sea water in the salinity range of 20–40‰ and temperature range of 5–3°C, *Acta Chem. Scandinavica*, *27*, 931–944.

Hauser, P. C., T. W. T. Rupasinghe, and N. E. Cates (1995), A multi-wavelength photometer based on light-emitting diodes, *Talanta*, *42*(4), 605-612.

Hopkins, A. E., K. S. Sell, A. L. Soli, and R. H. Byrne (2000), In-situ spectrophotometric pH measurements: The effect of pressure on thymol blue protonation and absorbance characteristics, *Marine Chemistry*, *71*(1-2), 103-109.

Hoppe, C., G. Langer, S. Rokitta, D. Wolf-Gladrow, and B. Rost (2012), Implications of observed inconsistencies in carbonate chemistry measurements for ocean acidification studies, *Biogeosciences*.

Hunter, K. A. (1998), The temperature dependence of pH in surface seawater, *Deep Sea Research Part I: Oceanographic Research Papers*, *45*(11), 1919-1930.

Hunter, K. A., and B. Macaskill (1999), Temperature and dye corrections in the spectrophotometric measurement of pH in surface seawater, paper presented at 2nd International Symposium CO2 in the Oceans.

Husheer, S. L. G. (2001), On Spectrophotometric PH Measurement in Seawater Media: A Thesis Submitted in Partial Fulfilment of the Requirements for the Degree of Master of Science (Chemistry) at the University of Otago, Dunedin, New Zealand, Master of Science thesis, University of Otago.

Johnson, K. S., W. M. Berelson, E. S. Boss, Z. Chase, H. Claustre, S. R. Emerson, N. Gruber, A. Kortzinger, M. J. Perry, and S. C. Riser (2009), Observing biogeochemical cycles at global scales with profiling floats and gliders: Prospects for a global array, *Oceanography*, 216-225.

Kaltenbacher, E., E. Steimle, and R. Byrne (2000), A compact, in-situ, spectrophotometric sensor for aqueous environments: design and applications, IEEE.

Kim, H., and K. Lee (2009), Significant contribution of dissolved organic matter to seawater alkalinity, *Geophys. Res. Lett*, *36*, L20603.

Larsen, M., S. M. Borisov, B. Grunwald, I. Klimant, and R. N. Glud (2011), A simple and inexpensive high resolution color ratiometric planar optode imaging approach: application to oxygen and pH sensing, *Limnol. Oceanogr.: Methods*, *9*, 348-360.

Laser, D., and J. Santiago (2004), A review of micropumps, *Journal of Micromechanics and Microengineering*, *14*, R35.

Le Bris, N., M. Zbinden, and F. Gaill (2005), Processes controlling the physico-chemical micro-environments associated with Pompeii worms, *Deep Sea Research Part I: Oceanographic Research Papers*, *52*(6), 1071-1083.

Liebsch, G., I. Klimant, C. Krause, and O. S. Wolfbeis (2001), Fluorescent imaging of pH with optical sensors using time domain dual lifetime referencing, *Analytical Chemistry*, *73*(17), 4354-4363.

Liu, X., M. C. Patsavas, and R. H. Byrne (2011), Purification and Characterization of meta-Cresol Purple for Spectrophotometric Seawater pH Measurements, *Environmental Science & Technology*, 4862–4868.

Liu, X., Z. A. Wang, R. H. Byrne, E. A. Kaltenbacher, and R. E. Bernstein (2006), Spectrophotometric measurements of pH in-situ: Laboratory and field evaluations of instrumental performance, *Environmental Science and Technology*, *40*(16), 5036-5044.

Martz, T. R., J. G. Connery, and K. S. Johnson (2010), Testing the Honeywell DurafetŽ for seawater pH applications, *Limnol. Oceanogr. Methods*, *8*, 172-184.

Martz, T. R., J. J. Carr, C. R. French, and M. D. DeGrandpre (2003), A submersible autonomous sensor for spectrophotometric pH measurements of natural waters, *Analytical Chemistry*, *75*(8), 1844-1850.

McElligott, S., R. Byrne, K. Lee, R. Wanninkhof, F. Millero, and R. Feely (1998), Discrete water column measurements of CO2 fugacity and pHT in seawater: a comparison of direct measurements and thermodynamic calculations, *Marine Chemistry*, *60*(1-2), 63-73.

Millero, F. J. (2007), The marine inorganic carbon cycle, *Chemical Reviews*, *107*(2), 308-341.

Mosley, L. M., S. L. G. Husheer, and K. A. Hunter (2004), Spectrophotometric pH measurement in estuaries using thymol blue and m-cresol purple, *Marine Chemistry*, *91*(1-4), 175-186.

Nakano, Y., H. Kimoto, S. Watanabe, K. Harada, and Y. W. Watanabe (2006), Simultaneous vertical measurements of in situ pH and CO2 in the sea using spectrophotometric profilers, *Journal of Oceanography*, *62*(1), 71-81.

O'Toole, M., and D. Diamond (2008), Absorbance based light emitting diode optical sensors and sensing devices, *Sensors*, *8*(4), 2453-2479.

Ogilvie, I., V. Sieben, M. Mowlem, and H. Morgan (2011), Temporal optimisation of microfluidic colourimetric sensors using a novel multiplexed stop-flow architecture, *Analytical Chemistry*, 4814–4821.

Ogilvie, I., V. Sieben, C. Floquet, R. Zmijan, M. Mowlem, and H. Morgan (2010), Reduction of surface roughness for optical quality microfluidic devices in PMMA and COC, *Journal of Micromechanics and Microengineering*, *20*, 065016.

Ohline, S. M., M. R. Reid, S. L. G. Husheer, K. I. Currie, and K. A. Hunter (2007), Spectrophotometric determination of pH in seawater off Taiaroa Head, Otago, New Zealand: Full-spectrum modelling and prediction of pCO2 levels, *Marine Chemistry*, *107*(2), 143-155.

Robert-Baldo, G., M. Morris, and R. Byrne (1985), Spectrophotometric determination of seawater pH using phenol red, *Analytical chemistry*, *57*(13), 2564-2567.

Sabine, C. L., R. A. Feely, N. Gruber, R. M. Key, K. Lee, J. L. Bullister, R. Wanninkhof, C. S. Wong, D. W. R. Wallace, and B. Tilbrook (2004), The oceanic sink for anthropogenic CO2, *Science*, *305*(5682), 367-371.

Seidel, M. P., M. D. DeGrandpre, and A. G. Dickson (2008), A sensor for in situ indicator-based measurements of seawater pH, *Marine Chemistry*, *109*(1-2), 18-28.

Seiter, J., and M. DeGrandpre (2001), Redundant chemical sensors for calibration-impossible applications, *Talanta*, *54*(1), 99-106.

Shitashima, K., Y. Koike, M. Kyo, and A. Hemmi (2008), Development of electrochemical in-situ pH-pCO2 sensor for deep-sea oceanography applications, paper presented at IEEE Sensors, IEEE.

Stich, M. I. J., L. H. Fischer, and O. S. Wolfbeis (2010), Multiple fluorescent chemical sensing and imaging, *Chem. Soc. Rev.*, *39*(8), 3102-3114.

Tapp, M., K. Hunter, K. Currie, and B. Mackaskill (2000), Apparatus for continuous-flow underway spectrophotometric measurement of surface water pH, *Marine Chemistry*, *72*(2-4), 193-202.

Wang, Z. A., X. Liu, R. H. Byrne, R. Wanninkhof, R. E. Bernstein, E. A. Kaltenbacher, and J. Patten (2007), Simultaneous spectrophotometric flow-through measurements of pH, carbon dioxide fugacity, and total inorganic carbon in seawater, *Analytica Chimica Acta*, *596*(1), 23-36.

Yao, W., X. Liu, and R. H. Byrne (2007), Impurities in indicators used for spectrophotometric seawater pH measurements: Assessment and remedies, *Marine Chemistry*, *107*(2), 167-172.

Zhang, H., and R. H. Byrne (1996), Spectrophotometric pH measurements of surface seawater at in-situ conditions: absorbance and protonation behavior of thymol blue, *Marine Chemistry*, *52*(1), 17-25.

Chapter 4: Miniaturization of a spectrophotometric pH system

4.1. Introduction

Lab-on-Chip technology has greatly improved over the last decades and enabled considerable miniaturisation of analytical systems leading to a reduction in reagent and power consumption. The implementation of microfluidic technology on such platforms is of great interest for environmental monitoring, in particularly in aquatic systems (Prien, 2007).

High resolution carbonate chemistry measurements (e.g. pH, pCO_2, Total Alkalinity (TA)) are urgently required in order to observe the ocean acidification phenomena and study its consequences. Large scale monitoring of carbonate chemistry in the oceans will only be possible with low cost sensors featuring low power and reagent consumption.

Here we report a low cost spectrophotometric pH sensor with high precision (0.001 pH units) and accuracy (better than 0.004). The system uses a simple micro-fluidic design integrated in a shipboard instrument with low sample (550 µL) and reagent (12 µL) consumption. A robust optical set up is achieved with the use of a custom-made polymeric flow cell coupled to a three wavelength Light Emitting Diode (LED). The system is adaptable for continuous underway measurements or discrete samples analysis. This work forms a key step toward the development of a fully integrated microfluidic pH analyser for *in situ* deployment.

4.2. Development of a colorimetric microfluidic pH sensor for autonomous seawater measurements

4.2.1. Instrument design

4.2.1.1. System overview and principles of operation

The instrument is a lab on a chip implementation of a continuous flow analyser using flow injection analysis. A pulse of pH indicator dye, which has a small perturbing effect on the measured pH is injected into a continuous sample stream where it mixes and disperses with the sample thus creating variable dye concentration as a function of time. Assay pH is measured optically over a range of dye concentrations and hence the perturbation in measured pH is determined and removed by regression to theoretical pH at zero dye concentration.

A schematic of the pH system is presented in Figure 4.1.A. Syringe pumps (Nanomite, Harvard Apparatus, UK) were used to propel the seawater sample (550 µl) and the thymol blue indicator (12 µL). Four micro-inert valves (LFNA1250125H, Lee Products Ltd., UK) controlled the fluid distribution. The reagent and sample streams were mixed in the flow cell in a static mixer before entry into the absorption cell. The light source was formed by a three wavelength LED (435 nm

(25 nm Full Width Half Maximum (FWHM)), 596 nm (15 nm FWHM), and 750 nm (30 nm FWHM), Roithner Laser, Austria), and light transmitted through the absorption cell was recorded by a linear array spectrometer (grating: 300 Line Composite Blaze and Slit width: 5 µm, HR4000, Ocean Optics Inc., UK) with a 0.3 nm wavelength resolution. The system was controlled by computer using custom software (written in LabVIEW, National Instruments Inc., UK) using a control card (PCI 6289, National Instruments Inc., UK). Custom electronics boards were developed by Andy Harris (National Oceanography Centre, Southampton) to interface the valves, light sources and thermistors (see schematics in Appendix 1). The measurements were made at temperatures close (+0.2 °C) to the *in situ* surface ocean values. During the measurement cycle, the flow cell was first rinsed with 300 µL of sample before injection of 12 µl of indicator and the determination of the absorption spectra. The remainder of the sample was pumped through the system at a rate of 60 $\mu L.min^{-1}$. A complete analysis cycle of a seawater sample took 6 min.

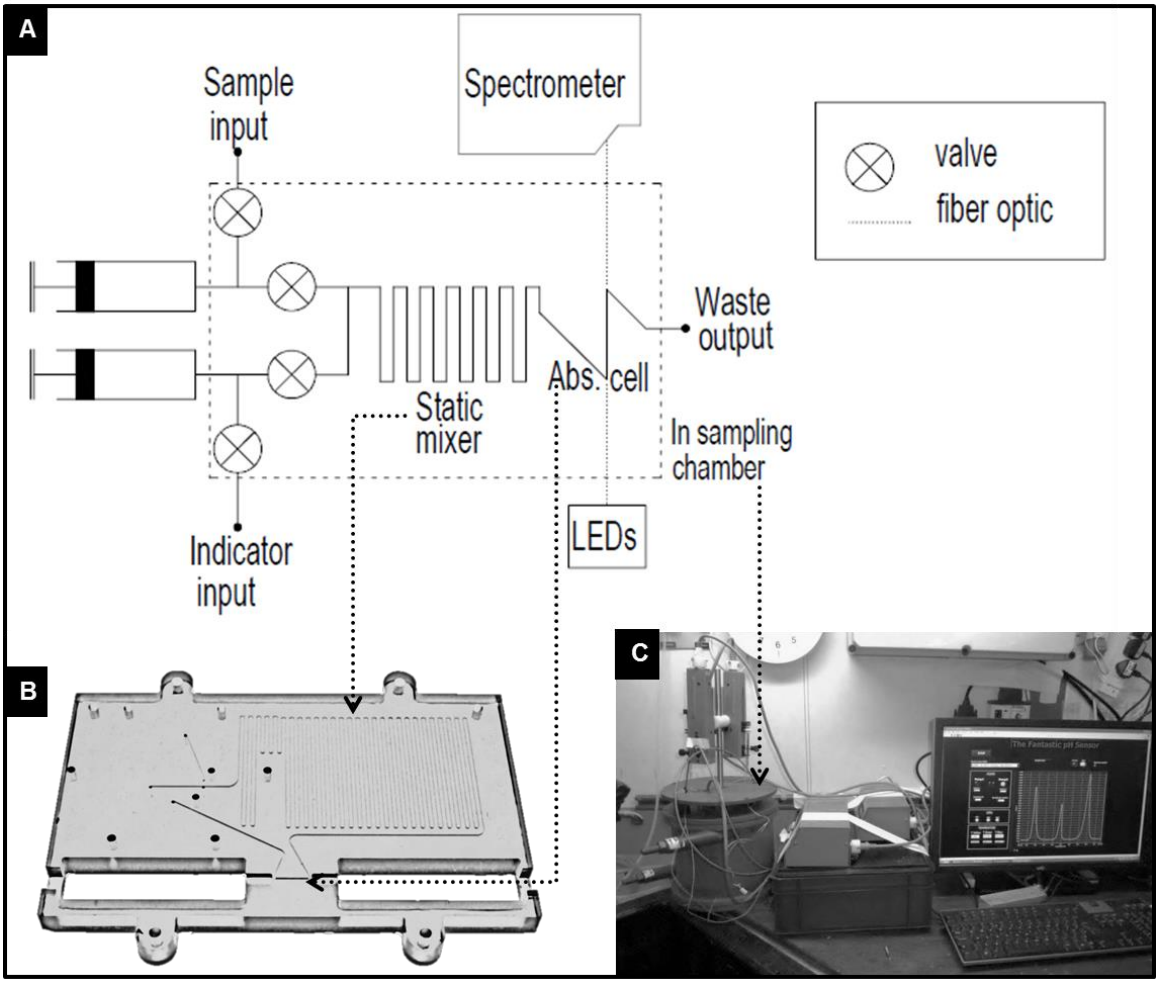

Figure 4.1: A. Schematic of the pH system. The seawater sample and indicator solution are pumped by two different syringe pumps and mixed in the flow cell in a static mixer before entering the absorption cell. The LEDs' light transmitted through the absorption cell is recorded by the HR4000 spectrometer. The measurement is made close to in situ temperature (+0.2 °C) by placement of the microfluidic flow cell in the sampling chamber which has a continuous flow of the ship's underway seawater supply. **B.** Microfluidic flow cell milled in tinted PMMA. All the cross sections of the channels are 250 x 250 µm except for the absorption cell which is 700 x 700 µm. **C.** Picture of the pH set up aboard the RRS Discovery. The sampling chamber is on the left with the two syringe pumps on top. The electronic control box, light source and detector are in the middle and the computer is on the right.

4.2.1.2. Microfluidic flow cell design: mixing of the indicator in the sample

The use of a static mixer instead of active mixing systems reduces power consumption and is more straightforward to include in the custom designed PMMA flow cell. Bench top pH systems typically use 100 mm path length cuvettes (Clayton and Byrne, 1993;Friis et al., 2004;Ohline et al., 2007;DelValls, 1999;Wang et al., 2007) with enhanced sample to indicator mixing ratios (700:1 to 1000:1) in order to minimize the impact of the indicator addition on the sample pH (Chierici et al.,

1999). Similar to work by Martz *et al.*(Martz et al., 2003) and Seidel *et al.* (Seidel et al., 2008) in macro fluidic systems, we addressed the impact of the indicator on sample pH by measurement of the pH over a wide range of mixing ratios (1:25 to 1:80) and used this data to regress back to a theoretical pH when no indicator was present (see Figure 4.7 in 4.2.3. Correction for indicator induced pH perturbation). This range in mixing ratios was created by providing a short (7 seconds, 12 uL) pulse of indicator into the flow cell. This pulse is dispersed in the long serpentine mixer by "Taylor Aris" dispersion resulting from the fluid flow reduction near the channel walls due to enhanced friction as detailed below (Taylor, 1953;Edwards and Brenner, 1993). The dispersion produced a near Gaussian indicator concentration profile in the sample stream in time and space. The end tail of the indicator slug was used to calculate pH as a function of indicator concentration and is interpolated to a zero indicator concentration. A sample flow rate of 60 µL.min^{-1} was used in order to obtain an enhanced dispersion and a homogenous mixing across the channel. A 10 mm long absorbance cell was used in our design in order to minimize deviations from Beer Lambert's law (see 4.2.4.2. Deviation due to indicator gradient in the absorption cell). This approach allowed us to use flow rates which were sufficiently high to enable good flow control via the pumps.

4.2.1.2.1. Diffusion

The mixing of the indicator into the seawater sample relied on diffusion in the flow cell. Full mixing was anticipated if the residence time (τ_D) in the serpentine mixer was sufficient to allow for a molecule of indicator to diffuse from the top to the bottom of the channel.

$$\tau_D \approx w^2/4D \qquad (4.1)$$

where w=width of the channel and D=diffusion coefficient.

The diffusion coefficient of a charged particle is described in equation 4.2.

$$D = \frac{\mu_q k_B T}{q} \qquad (4.2)$$

Where q is the electrical charge of a particle, μ_q is the electrical mobility of the charged particle (i.e. the ratio of the particle's terminal drift velocity to an applied electric field), k_B is the Boltzmann's constant, T is the absolute temperature.

However the electrical mobility is difficult to determine. A minimum value of the diffusion coefficient can then be evaluated thanks to the Einstein-Stokes equation relating D to the radius of the diffusive molecule for non-charged spherical particles.

$$D = \frac{k_B T}{6\pi\eta r} \qquad (4.3)$$

Where η is the viscosity and r is the radius of the spherical particle.

Table 4.1 summarizes some typical diffusivity for various tracers in water at room temperature.

Table 4.1: Typical diffusivities for various tracers in water at room temperature (taken from (Squires and Quake, 2005)):

Characteristic diffusivities		
Particle	**Typical Size**	**Diffusion constant**
Solute ion	10^{-1} nm	$2x10^3$ $\mu m^2/s$
Small protein	5 nm	40 $\mu m^2/s$
Virus	100 nm	2 $\mu m^2/s$
Bacterium	1 µm	0.2 $\mu m^2/s$
Mammalian/human cell	10 µm	0.02 $\mu m^2/s$

The size of the molecule of thymol blue (≈1-2 nm) is roughly estimated by measuring the length of the longest carbon chain. D is then estimated to be 5.2E-10 m^2/s. This estimation is made by taking the worst case in terms of molecule size and by neglecting the charges of the diffusing particulate as well as salt ions in seawater. When a colloidal electrolyte such as a dye is allowed to diffuse freely into water, the rapidly diffusing non-colloidal ions tend to diffuse away from the slowly diffusing oppositely charged particles, so that a potential gradient is set up in the solution. This potential gradient causes the diffusion coefficient to be very different from that which would be expected from the Stokes-Einstein equation. The velocity of diffusion may actually be higher for this substance than for the one whose colloidal particles are very much smaller (Hartley and Robinson, 1931;Robinson, 1935;Lenher and Smith, 1936). Even if dye impurities will tend to decrease this effect, the diffusion coefficient of thymol blue is probably twice as big as the first estimate. Calculation on mixing and Taylor dispersion were therefore done with D_1=5.2E-10 and D_2=1E- m^2/s.

With a channel width of 250 µm, the recommended residence time are τ_{D1}=16 s and τ_{D2}=30 s.

4.2.1.2.2. Dispersion

In pressure driven micro-fluidic devices, the fluid shear disperses the solute slug as it travels through the micro channel. This dispersion is caused by the slowing down of the fluid near the channel walls due to the no-slip flow condition at the solid–fluid interface (Taylor, 1953;Edwards and Brenner, 1993). The resulting variation in the streamline velocity causes the solute band to stretch as convection proceeds in the axial direction, pulling the plug of indicator in a "bullet shape". Molecular diffusion across the solute streamlines ultimately limits this spreading process and homogenises the dye over the cross section. The overall effect is an enhancement of the rate

of axial dispersion over and above what would occur due to molecular diffusion alone in the absence of flow. The phenomena is called ‘‘shear-induced’’ or ‘‘Taylor’’ or ‘‘Taylor-Aris’’ dispersion. Figure 4.2 shows the Taylor dispersion phenomenon in time where an inert dye is transported in a micro channel by a liquid driven by a pump.

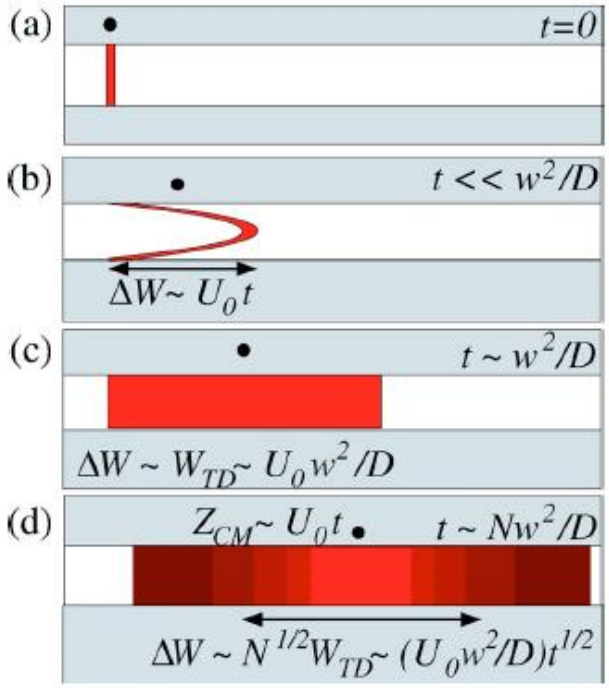

Figure 4.2: Taylor dispersion. (a) An infinitesimally thin tracer stripe in a circular channel of radius w. (b) Under a pressure-driven flow, the stripe is convectively stretched into a parabolic shape whose width W increases linearly with time. (c) After a characteristic time scale $T_D \sim w^2/D$ for tracers to diffuse across the channel, the parabola is “smoothed” into a plug of width $W_{TD} \sim U_0 w^2/D$. (d) The plug can be broken into many thin stripes, each of which subsequently undergoes processes (a)-(c) to be smoothed into plugs of width W_{TD} on a time scale T_D. A tracer thus takes a random step of size $\leq W_{TD}$ on each time step T_D, causing the stripe to evolve as a Gaussian spreading with effective diffusivity $Dz \sim U_0^2 w^2/D$. (Taken from (Squires and Quake, 2005)).

At long times (i.e. longer than the diffusion time across the section of the channel), the effective dispersion coefficient can be described as:

$$Deff = D\left(1 + \alpha\left(\frac{Ud}{D}\right)^2\right) \qquad (4.4)$$

where D is the molecular diffusion coefficient of the solute species, U is the average fluid velocity and d is the characteristic length of the system. The above expression suggests that the overall dispersion in a pressure-driven system arises from two additive contributions. The first term results from diffusive transport in the flow direction whereas the second term represents the effective dispersivity due to the fluid shear. Note that the latter term scales with the square of the Peclet number (Pe=Ud/D), which estimates the relative magnitude of convective to diffusive transport rates in the system. The alpha coefficient multiplying this dimensionless group in Eq. 4.4

is a function of the channel cross section and has a value of 1/210 for pressure-driven flow between two parallel plates (Wooding, 1960). It is important to note that the exact cross section of the conduit can significantly affect the actual result (Aris, 1956;Doshi et al., 1978;Dutta and Leighton Jr, 2001;Guell et al., 1987;Chatwin and Sullivan, 1982). Mathematically, Dutta *et al.* (Dutta et al., 2006) evaluated this effect by introducing a function f in Eq. 4.4 with alpha from the two parallel plane geometry to yield:

$$Deff/D = 1 + \alpha\left(\frac{Ud}{D}\right)^2 f \qquad (4.5)$$

They showed that f=1.76 for a square cross section (equivalent to α=0.0084 (Datta and Ghosal, 2009)).

This coefficient (α=0.0084) is used to predict the Taylor dispersion in the flow cell at a flow rate of 60 µL/min (Figure 4.3).

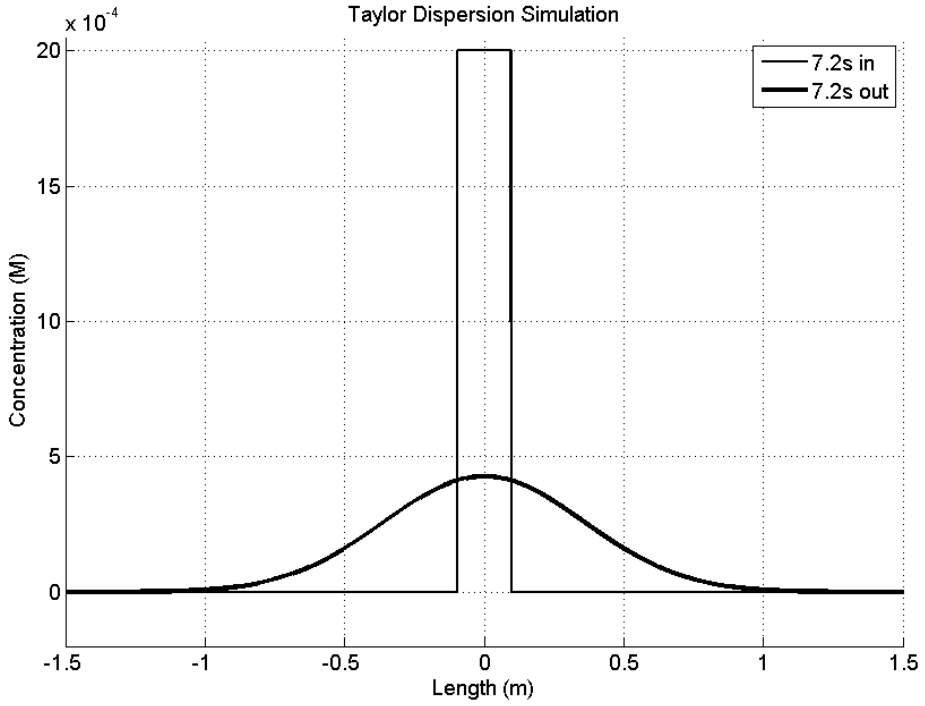

Figure 4.3: Simulation of the axial dispersion of the indicator slug at a flow rate of 60uL/min with an injection of 12 µL of thymol blue and diffusion coefficient D=5.20E-10 m^2/s. The thin line represent profile of the slug of indicator just after injection in the cell and the thick line represents the profile of the slug of indicator after passing through the mixer.

4.2.1.3. Optical set up

The light source used in our pH system was a tri-coloured LED with wavelengths of 435 nm (25 nm FWHM) and 596 nm (15 nm FWHM) corresponding to the absorption maxima of the indicator forms (HI^- and I^{2-}), and 750 nm (30 nm FWHM) to monitor the sample turbidity and Schlieren

effect (Figure 4.4). The three individual single wavelength LED dies were mounted in a single package (TO-98) to create the tri-coloured LED.

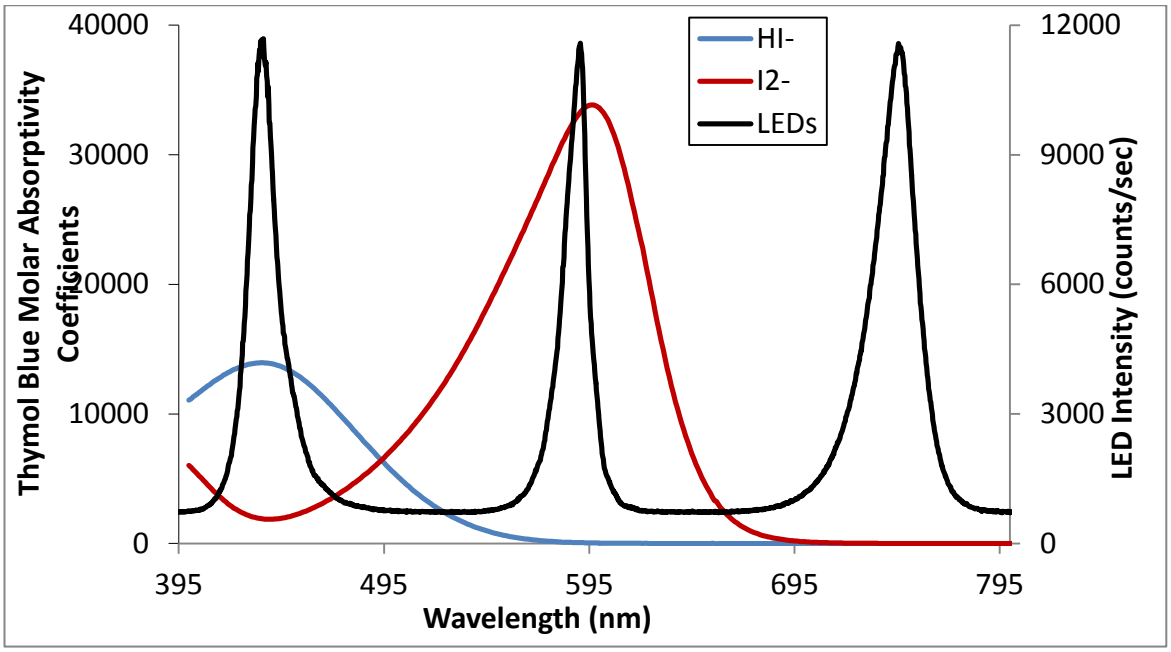

Figure 4.4: Thymol blue indicator and light source spectra. Extinction coefficient spectra of the basic (I2- in red) and acidic (HI- in blue) forms of the thymol blue indicator (data from (Ohline et al., 2007)). The light spectrum of the tri-coloured LED is shown in black.

A linear array photodiode spectrometer (HR4000, Ocean Optics, UK) was used as detector. To improve the signal to noise ratio, absorbances at the three wavelengths were measured by integration of the light signal on the full spectrum of the LED. The light source and detector were connected to the microfluidic chip by two optical fibres (600 µm diameter, Thorlabs, USA).

4.2.1.4. Measurement at in situ temperature

The pH measurements were undertaken at *in situ* surface temperature by submersion of the microfluidic chip in the sampling chamber which was continuously flushed using surface seawater (Figure 4.1.C). The valves mounted on the chip are protected from the seawater by a small chamber connected to the chip (Figure 4.5).

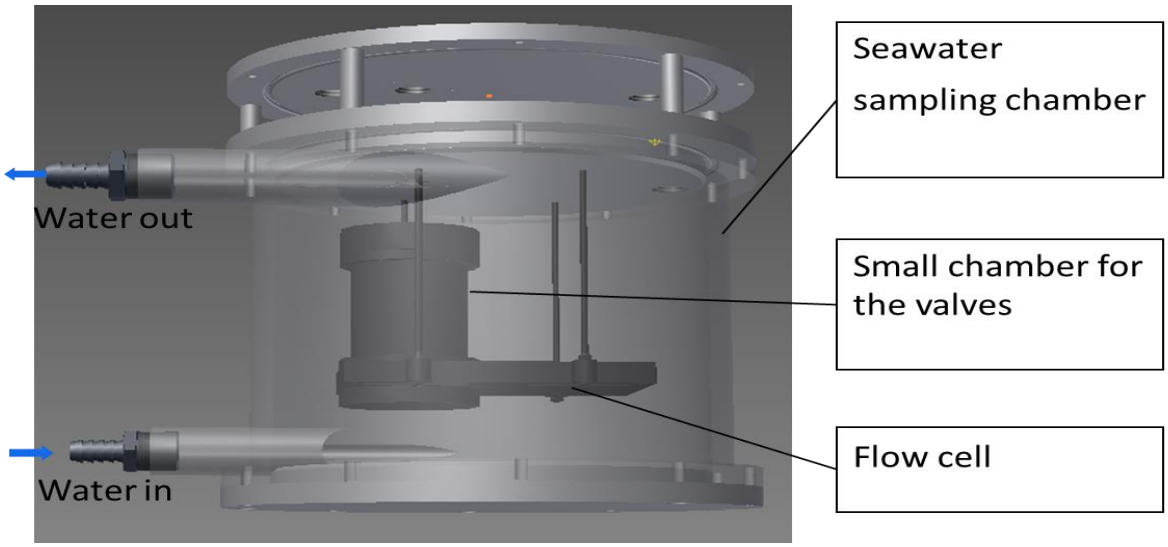

Figure 4.5: Underway sampling chamber. The flow cell is immersed in seawater which flows continuously from the ship's underway surface water supply.

This approach simplified the set-up, minimised potential gas exchange with the atmosphere and resulted in a minor temperature discrepancy between the sampling chamber (i.e. measurement temperature) and *in situ* seawater temperatures in the ocean, thereby minimizing the requirement for temperature correction of pH data as is the case for thermostatted (e.g. 25°C) measurements. During the pH system deployment on a cruise in European shelf seas in 2011, we observed a temperature difference between the surface ocean and the measurement chamber of only ca. 0.2 ± 0.06 °C. To avoid channel blockage and light scattering by particulates, an *in line* filter (0.45 µm pore size, Millex HP syringe filter Millipore Express® (PES) membrane 33 mm diameter, Millipore) was placed at the entry of the sample tube.

The design of the chamber was made in CAD using Autodesk Inventor Professional. Fabrication was outsourced to Quayside Precision Engineering in Southampton. All the drawings can be found in Appendix 2.

4.2.1.5. Second system for discrete samples analysis

Two set ups were achieved for the pH sensor: system 1 (detailed above) connected to the underway seawater supply of the ship with continuous pH measurements, and system 2 controlled at 25°C for discrete sample measurements. These two set ups differ mainly on two aspects:

1. Pumps
2. Measurement at 25°C

4.2.1.5.1. Pumps set up

Syringe pumps (Nanomite, Harvard Apparatus, UK) were used to control the fluids in the system 1. These syringes allowed a very accurate and reliable control of the fluid. Once set up correctly the system can run continuously and can be left unattended for weeks which is key for an underway system. However these pumps are fragile, expensive and bulky.

For system 2, smaller and cheaper solenoid pumps were used (MCP-50,12V, PTFE, 1/4-28UNF, Takasago Electric, Inc.). These pumps are less reliable and require a person checking on the delivered volume and flow rates on a regular basis. This is satisfactory for discrete sample measurement as the user needs to remain next to the instrument to manually change the samples. The main issue is that small bubbles of air can come into the system when changing the sample and this air accumulates in the sample pump, slowly reducing the volume per stroke delivered (hence the flow rate of the sample). This is resolved by disconnecting the tubing at the outlet of the pump at the start of each sequence of sample measurements. The syringe pump from the Lee Company (LPVA1520075D Lee Products Ltd., UK) is potentially a good alternative for the Takasago solenoid pump and should be implemented on the next prototype.

4.2.1.5.2. Measurement at 25°C

Discrete pH measurements were undertaken at 25°C. The temperature was controlled by immersion of the chip: either directly in the water bath using the small valve pot or in a temperature chamber connected to a water bath which allows water flow (Figure 4.6). The latter option is particularly interesting as it allows us to couple the pH system with instruments used to measure DIC and TA such as the VINDTA instrument which already has a water bath at 25 °C (Mintrop, 2004).

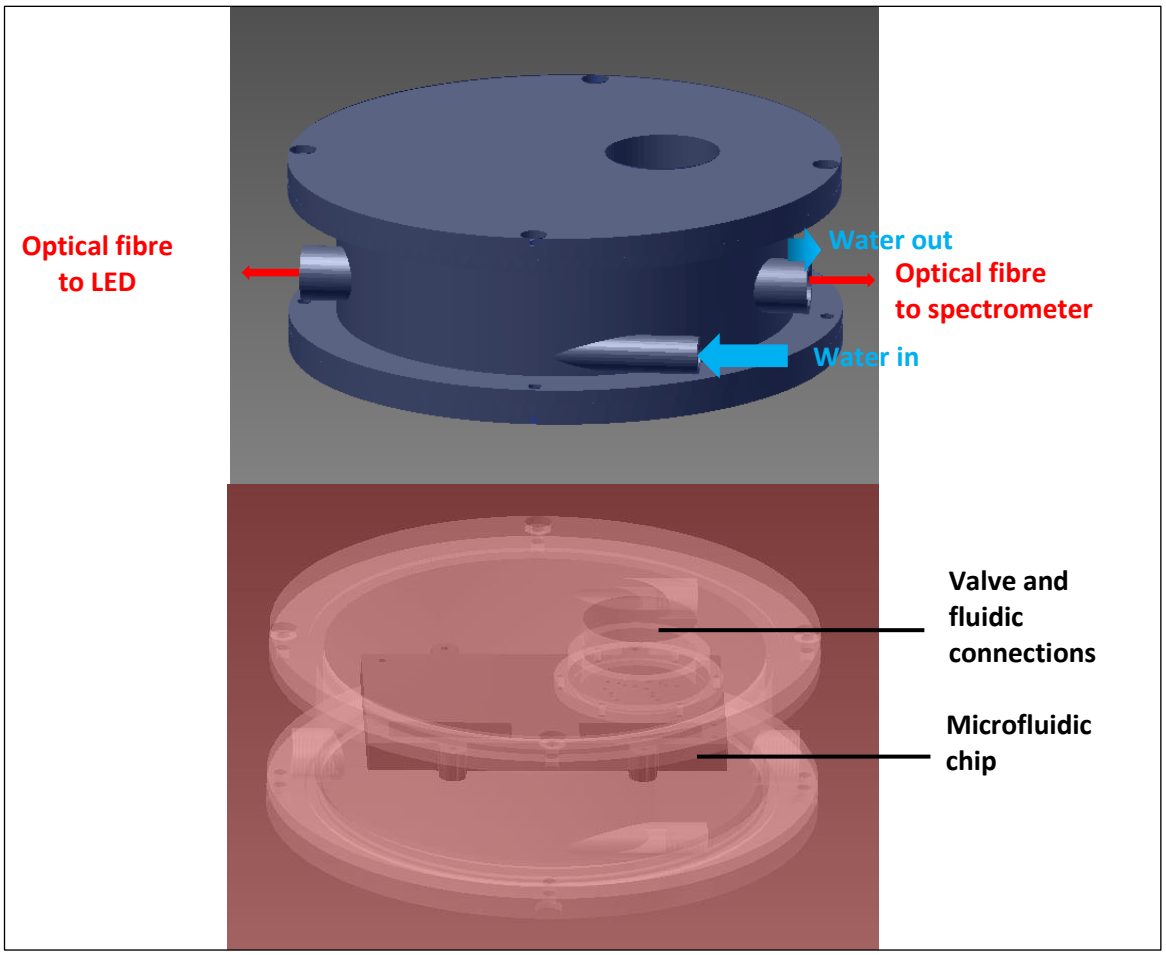

Figure 4.6: Temperature control chamber.

4.2.2. Thymol Blue indicator characterization

The acidic form of the indicator is dominant for absorbance measurements at pH 5, and the basic form at pH 10. Nevertheless, it is important to account for the absorbance contributions of I^{2-} and HI^{-} to the determination of the extinction coefficient of the acidic form of indicator at 596 nm ($\varepsilon^{HI^-}_{596}$) (see Chapter 3 for definition) because of the important I^{2-} absorption at 596 nm relative to the HI^{-} absorption at this wavelength (Zhang and Byrne, 1996). The corrections for each molar absorptivity value used for the determination of molar absorptivity ratios are (corrected extinction coefficient are annotated with prime):

$$\varepsilon_{HI}^{435\prime} = \frac{\varepsilon_{435}^{HI^-}[Ind_{acid}^{tot}][I_{basic}^{2-}] - \varepsilon_{435}^{I^{2-}}[Ind_{basic}^{tot}][I_{acid}^{2-}]}{[HI_{acid}^{-}][I_{basic}^{2-}] - [HI_{basic}^{-}][I_{acid}^{2-}]} \qquad (4.6)$$

$$\varepsilon_{I}^{435\prime} = \frac{\varepsilon_{435}^{HI^-}[Ind_{acid}^{tot}][HI_{basic}^{-}] - \varepsilon_{435}^{I^{2-}}[Ind_{basic}^{tot}][HI_{acid}^{-}]}{[HI_{basic}^{-}][I_{acid}^{2-}] - [HI_{acid}^{-}][I_{basic}^{2-}]} \qquad (4.7)$$

$$\varepsilon_{HI}^{596\prime} = \frac{\varepsilon_{596}^{HI^-}[Ind_{acid}^{tot}][I_{basic}^{2-}] - \varepsilon_{596}^{I^{2-}}[Ind_{basic}^{tot}][I_{acid}^{2-}]}{[HI_{acid}^{-}][I_{basic}^{2-}] - [HI_{basic}^{-}][I_{acid}^{2-}]} \quad (4.8)$$

$$\varepsilon_{I}^{596\prime} = \frac{\varepsilon_{596}^{HI^-}[Ind_{acid}^{tot}][HI_{basic}^{-}] - \varepsilon_{596}^{I^{2-}}[Ind_{basic}^{tot}][HI_{acid}^{-}]}{[HI_{basic}^{-}][I_{acid}^{2-}] - [HI_{acid}^{-}][I_{basic}^{2-}]} \quad (4.9)$$

Where

$\left[Ind_{acid}^{tot}\right]$= total indicator concentration in the acidic buffer solution

$\left[Ind_{basic}^{tot}\right]$= total indicator concentration in the basic buffer solution

The concentration of the two indicator forms in each buffer was determined by the pH of the buffer:

$\left[I_{basic}^{2-}\right]$= I^{2-} concentration in the basic buffer= I_b^{2-}*$\left[Ind_{basic}^{tot}\right]$

$\left[I_{acid}^{2-}\right]$= I^{2-} concentration in the acidic buffer= I_a^{2-}*$\left[Ind_{acid}^{tot}\right]$

$[HI_{basic}^{-}]$= HI^{-} concentration in the basic buffer= HI_b^{-}*$\left[Ind_{basic}^{tot}\right]$

$[HI_{acid}^{-}]$= HI^{-} concentration in the acidic buffer= HI_a^{-}*$\left[Ind_{acid}^{tot}\right]$

With the $HI_x^- \; and \; I_b^{2-}$factors defined by:

HI_x^-=1/(1+$10^{pH_x - pK_2} + \frac{1}{10^{pH_x - pK_1}}$) (4.10)

I_x^{2-}=HI_x^-*$10^{pH_x - pK_2}$ (4.11)

Accounting for the presence of the two indicator species in the acidic and basic solutions resulted in a correction of up to 11% for e_1, 1% for e_2 and 5% for e_3 (see Chapter 3 for definition).

The temperature (T) and salinity (S) dependencies of the extinction coefficients were estimated via stepwise multiple linear regressions of the experimental results with T, T^2, S and S^2. A t-test was performed to find the most important variable to the model of the e_i coefficients as a function of temperature and salinity and an F-test was used to determine if the model was adequate. The coefficients of the multiple variable regressions as well as the statistical analysis results are given in Table 4.2.

Table 4.2: Coefficients derived from multiple linear regression analysis, with results of statistical analysis.

Parameter	Intercept	T	T^2	S	S^2	F-test	Prob>F	R^2	MSE
$\varepsilon^{HI^-}_{435}$	13506		-0.535			21.22	2.517e-4	0.555	1.18e4
$\varepsilon^{HI^-}_{596}$	99.2208	-3.321	0.126			71.25	5.436e-9	0.893	8.127
$\varepsilon^{I_2^-}_{435}$	2271.2		0.147			5.30	0.034	0.238	3.862e3
$\varepsilon^{I_2^-}_{596}$	41881	51.015		755.033	13.453	7.71	0.002	0.591	2.497e5

MSE: mean square error. **Prob**: Probability.

The discrepancy between pH values calculated with these coefficients and values calculated with coefficients from Zhang and Byrne (Zhang and Byrne, 1996) was about 0.02, and varied between 0.015 and 0.029 pH units. Aparent extinction coefficients are influenced by the wavelength resolution of the detector. Zhang and Byrne used the Varian Instruments Cary 17D and Cary 3 spectrophotometers with a wavelength resolution of ca. 1-2 nm. We estimated that about 0.015 pH units of the observed discrepancy was due to the wide wavelength resolution in our system resulting from integration on the whole LED peak (LEDs FWHM = 15-20 nm). This was estimated by comparing our pH values with those calculated with a wavelength resolution as narrow as 0.3 nm (resolution of the spectrophotometer HR4000 used) and coefficients from Zhang and Byrne. The consistency and the magnitude of this discrepancy demonstrated that it was correct to integrate the signal under the whole LED peak. Impurities in the indicators also affected the coefficients (Liu et al., 2011;Yao et al., 2007) but to a smaller extent (about 0.005 pH units). The magnitude of the discrepancy due to the wide wavelength resolution highlighted the importance of the indicator characterization when using a system with wider wavelength resolution than the systems used to obtain the indicators' extinction coefficients and reported in the literature (Rérolle et al., 2012b). Finally, the variability in the observed discrepancy was mainly due to the fact that the salinity dependence of the extinction coefficient $\varepsilon^{I_2^-}_{596}$ was taken into account in our model, whereas it was not included in the model from Zhang and Byrne.

4.2.3. Correction for indicator induced pH perturbation

The interpolation of pH to a zero indicator concentration was undertaken using a weighted linear regression (Figure 4.7B), whereby the weights were the reverse of the squared error (noted u) in pH at each concentration ($1/upH([ind])^2$). The error in pH (equation 4.12) was calculated as the square root of the sum of the squares of the estimated uncertainties of the method (e.g. the indicator pK and molar absorptivities, the accuracy of the temperature, salinity and absorption measurements).

$$u_{pH} = \sqrt{\left(\frac{\partial pH}{\partial pK_2}\cdot u_{pK_2}\right)^2 + \left(\frac{\partial pH}{\partial R}\cdot u_R\right)^2 + \left(\frac{\partial pH}{\partial e_1}\cdot u_{e_1}\right)^2 + \left(\frac{\partial pH}{\partial e_2}\cdot u_{e_2}\right)^2 + \left(\frac{\partial pH}{\partial e_3}\cdot u_{e_3}\right)^2} \qquad (4.12)$$

upH varies between 0.0005 at low absorbance to 0.002 at high absorbance. At high absorbance, the main sources of error were the fluctuation of the light intensity at 435 nm, followed by temperature. At high absorbance, the errors in intensity at 435 nm, temperature, and intensity at 596 nm, were responsible for about 68%, 26%, and 6% of upH^2, respectively. At low absorbance, the main sources of error are temperature, followed by the fluctuation of the light intensity at 435 nm. At low absorbance, the errors in intensity at 435 nm, temperature, and intensity at 596 nm accounted for about 31%, 55%, and 14% of upH^2, respectively. Details of the calculations are given in the Matlab script in chapter 2.

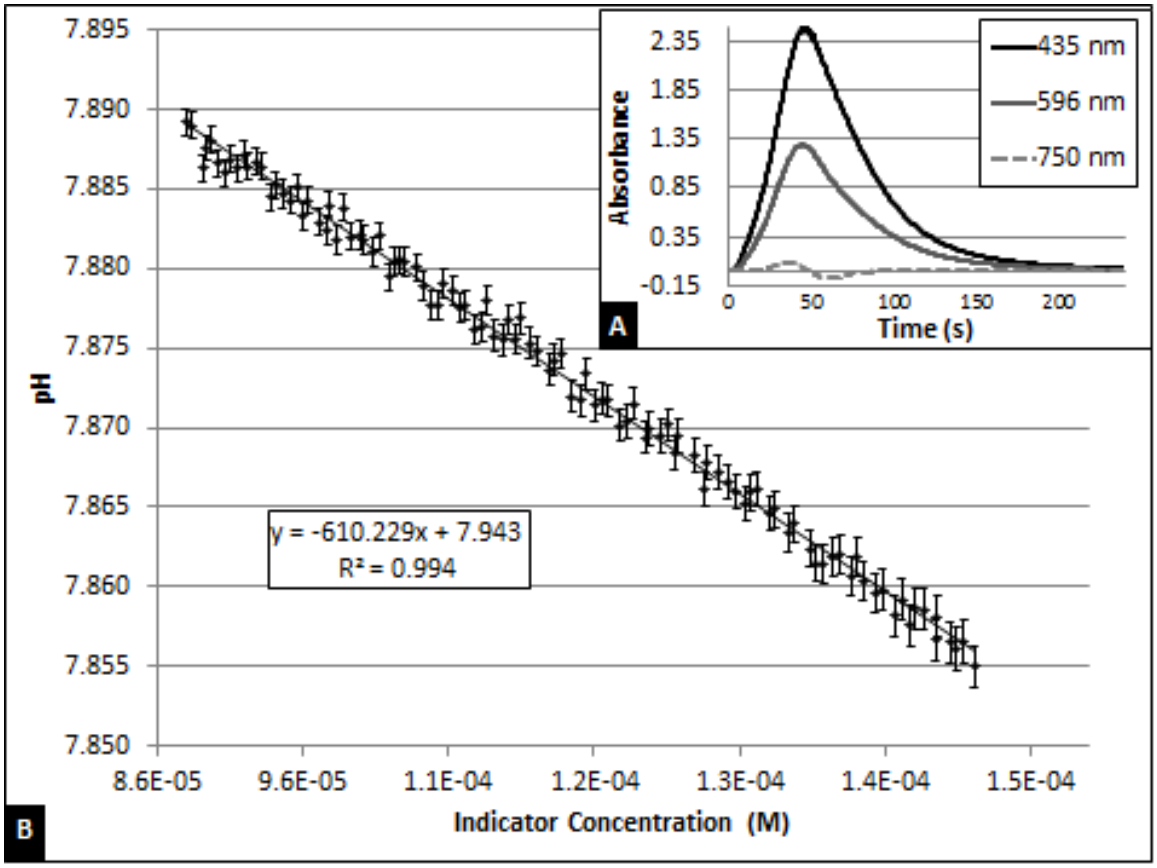

Figure 4.7: Correction for indicator induced pH perturbation. **A.** Absorbances at wavelengths 435, 596 and 750 nm as a function of time (s) as the indicator slug passes through the flow cell. **B.** pH as a function of indicator concentration (M). The end tail of the absorbance slug was used to calculate pH as a function of indicator concentration and is interpolated to a zero indicator concentration. The corrected pH is 7.943 in this example.

The mean magnitude of the correction was 0.02 ± 0.01 pH units during the cruise deployment of the analytical system (Surface ocean pH data obtained during cruise D366 are presented in Chapter 5). The estimated standard error of the corrected pH was on average 0.0005 ± 0.0003 pH units.

4.2.4. Deviations of absorbance behaviour from Beer's law

4.2.4.1. Deviation due to the polychromatic light source

The sensitivity of the absorbance measurement to signal variations and linearity of the Beer's law are affected by signal poly-chromaticity in the case that a non-monochromatic light source is used (Chan and Chan, 2001). The bandwidth ratio of the absorbance profile to the light source spectra was between 3 and 5 in our system. It was therefore important to verify that the sensitivity of the absorbance measurements was not affected by the integration of the signal over the full LED peak (Chan and Chan, 2001). Integration over the full LED peak did result in a small negative deviation of the apparent absorbance compared to the peak absorbance obtained with the single maximum absorption wavelength (Figure 4.8A and B). These effects were due to the fact that absorptivities are not constant across the spectral emission bands of the LEDs. The sensitivity of the detector also varies with the wavelength resulting in an increased signal at longer wavelengths and hence skewing of the LED emission spectra moving the peak to a higher wavelength (Hauser et al., 1995). In addition, the peak of the LED emission bands may not be well centered on the absorption peak of the indicator species. The linearity of the curves on Figure 4.8A and B was verified with the range of the relative sensitivity ($S=A_{apparent}/A_{peak}$) as a function of the peak absorbance (Chan and Chan, 2001) (Figure 4.8C). Although there was a deviation from Beer's law, the absorbance range is still in the linear range of Beer's law (within the ±5% tolerance range). It was therefore considered appropriate to integrate the signal of the full LED spectrum to calculate the absorbance values.

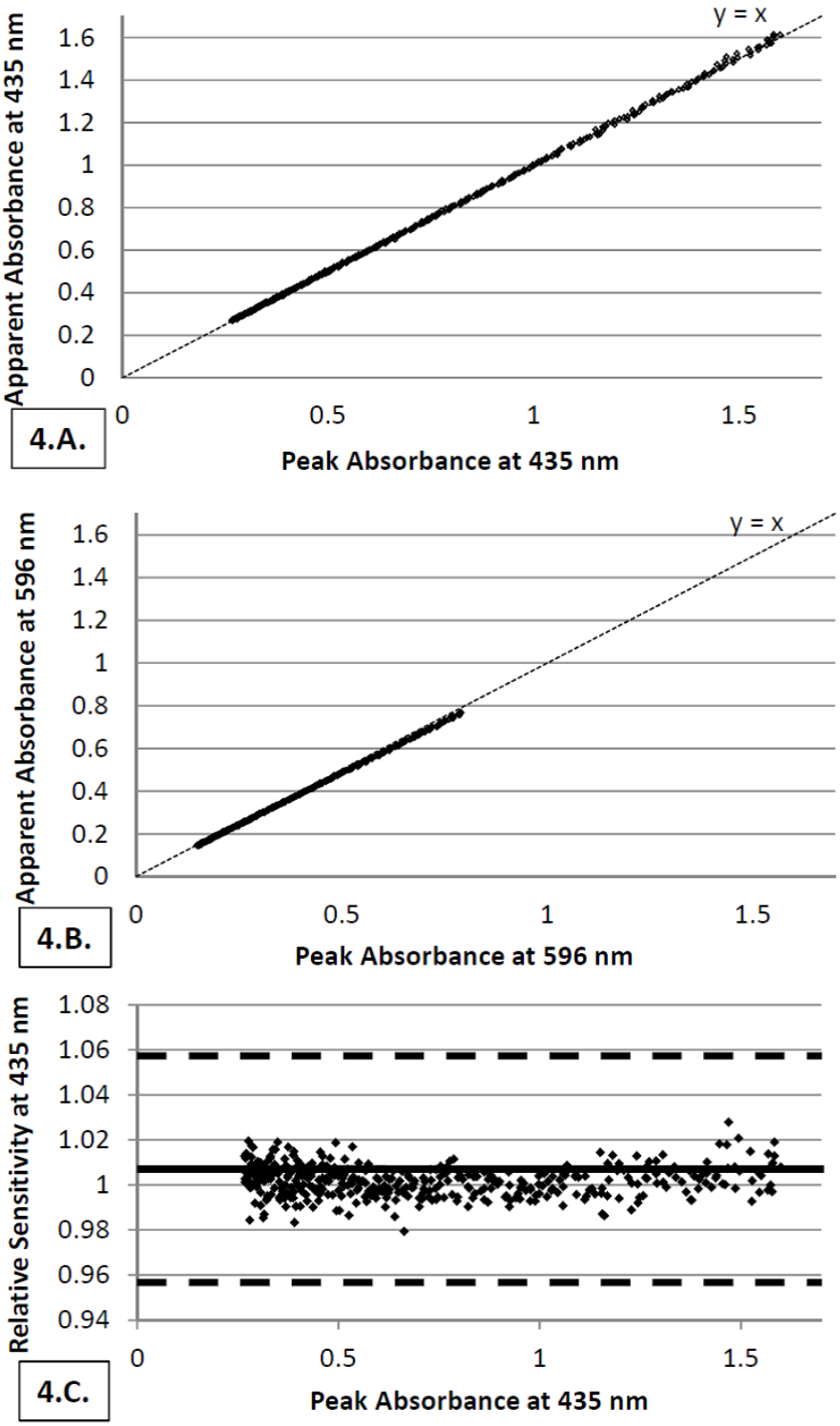

Figure 4.8: Sensitivity analysis. A. and B. Apparent Absorbance (using the whole LED peak) versus Peak Absorbance (using a single pixel). The dotted line represents the case when the peak absorbance equals the apparent absorbance. C. Linearity plot for the LED centred on 435 nm. The line represents the linear case and the dotted lines represent the ±5% tolerance interval.

4.2.4.2. Deviation due to indicator gradient in the absorption cell

The indicator gradient along the absorption cell length will lead to a systematic pH measurement error due to a deviation from the Beer Lambert's law condition which is the homogeneity of the substance within the optical path length. The error depends on the dispersion length of the indicator slug and the length of the optical cell. The dispersion length of the indicator after its passage through the static mixer in our microfluidic flowcell was estimated using a model based on Taylor-Aris dispersion theory (Ogilvie et al., 2011;Taylor, 1953). The concentration distribution obtained with the model at an 8 µm resolution was used to calculate pH, assuming a linear relationship between the indicator concentration and pH (as stated by the Beer Lambert's law). Absorbances at the two wavelengths of interest were deduced from pH and indicator concentration at every data point and then summed in order to obtain the absorbances of a 1 cm optical path length. These absorbances were processed using the same procedure as for sample measurements. The pH estimated from the linear regression was 0.0001 pH units lower than the actual pH of the sample. This error is of the same order of magnitude as the +0.0004 pH units offset estimated for the SAMI-pH system (Seidel et al., 2008). The deviation from the Beer Lambert's law due to indicator gradients is therefore also considered negligible in our system.

4.2.4.3. Deviation due to Schlieren effect

The indicator concentration gradients combined with the parabolic flow led to the formation of density lenses in the sample flow. The inflexion of the light through the absorption cell due to this artefact (the Schlieren effect) varies with wavelength (Dias et al., 2006). The Schlieren effect was evidenced here by absorption variations at 750 nm (Figure Fig. 4.7.A.). This phenomenon became noticeable at strong concentration gradients and resulted in non-linearity of the absorbance ratio as a function of indicator concentration. The Schlieren effect was relatively important in our system because of the low ionic strength (I=2 mM) of the indicator solution compared to the sample. Matching the density of the indicator solution to the sample by increasing the ionic strength of the indicator solution should reduce this effect. However thymol blue at high concentrations precipitates in high ionic strength solutions, and we were not able to prepare solutions of the thymol blue indicator at I=0.7. In order to estimate the influence of I on the Schlieren effect, we performed pH measurements with a meta-Cresol Purple indicator solution prepared at I=0.7. A significant reduction of at least 85% of the Schlieren effect was observed. The approach used here to reduce this artefact was to inject a volume of indicator in the cell large enough to obtain the maximum indicator concentration gradients at absorbance values higher than 1.7. For example in Figure 4.7.A., the highest indicator gradients at 435 nm, corresponding to the sharpest slopes towards the top of the curve, are observed at absorbances higher than 1.8.

The Schlieren effect became negligible at absorbances lower than 1.7 and we were then able to use absorbance values ranging from 0.2 and 1.7. The best linear fits to correct for the indicator addition were obtained with absorbance values ranging from 0.55 and 1.65 (RMS>0.99]).

4.2.5. System precision and accuracy

The performance of the system has been evaluated through pH analysis at 25°C of three bottles of certified Tris buffer (batch 7). The temperature was controlled to 0.01°C by placement of the flow cell in a temperature controlled water bath (Techne-10A Tempette). During the five weeks of deployment of the instrument at sea, we obtained a short term precision of 0.0009 pH unit (n=20) and pH values within the reported range of the certified Tris buffer (0.004 pH units) (Table 4.3).

Table 4.3: Precision and accuracy of certified Tris buffer measurements

Average discrepancy between certified pH and measured value for Tris buffer (n=20)	Precision (pH unit) of replicate Tris buffer analyses (n=20)	Date of analysis
0.0007	0.0007	11/06/2011
0.0021	0.0009	23/06/2011
0.0025	0.0011	07/07/2011

In order to estimate the precision of the system for natural seawater analyses at sea during the cruise, the standard deviation of 20 consecutives measurements was determined at three different locations. The locations were chosen where the ship maintained its position sufficiently long to obtain 20 measurements in similar water mass. Although this is not perfect as the water mass characteristics may vary with time, it gives a first estimate of system precision for replicated natural seawater analysis. The precision at the three locations was found to vary between 0.0008 and 0.0017 pH unit (n=20).

Measurement accuracy is affected by the accuracy of the indicator extinction coefficients and pK_2, the indicator perturbation correction method, and the accuracy of the temperature and salinity measurements. The analysis of the Tris buffer demonstrated the good accuracy of our indicator characterization (within 0.004 pH units) at 25°C and salinity 35. However, the Tris buffer analyses are less strongly affected by pH perturbations from the indicator additions than seawater and are therefore not appropriate to verify the indicator pH correction method. Comparison of cruise pH data with pH calculated from a pair of the carbonate parameters DIC, TA and pCO_2 showed a discrepancy between 0.005 and 0.013 pH units. Calculations were made using CO2SYS (Pierrot et al., 2006), on the total pH scale with K_1 and K_2 from Mehrbach *et al*. (Mehrbach et al., 1973),

refitted by Dickson and Millero (Dickson and Millero, 1987) and $KHSO_4$ from Dickson (Dickson, 1990). Part of this offset was likely due to the Schlieren effect impacting the indicator perturbation correction method (see 4.2.4.3. Deviation due to Schlieren effect). The error due to the Schlieren effect has been estimated to be 0.004 pH units during the cruise D366. Data from the cruise have been corrected for this offset. In order to verify the adequacy of the indicator pH correction method, DIC and TA certified reference material (CRM TA=2239.18±0.52 $\mu mol.kg^{-1}$ & DIC=2009.99±0.64 $\mu mol.kg^{-1}$, batch 117, Scripps Institution of Oceanography, USA) was analysed at 25.03 ± 0.01 °C at a later date with the new analytical configuration (i.e. with 12 µL of indicator per sample instead of the 5 µL injected per sample during the cruise deployment) to minimize the Schlieren effect and a new solution of indicator prepared from the same batch. The pH of the CRM at 25 °C can be estimated with an accuracy of about 0.006 pH units by propagation of the experimental error from DIC (±0.64 $\mu mol.kg^{-}1$) and TA (±0.52 $\mu mol.kg^{-1}$) values and of the errors in pK_1 and pK_2 (see 1.1 Marine carbonate chemistry): the experimental error in DIC and TA result in an error of about 0.002 pH units (calculated in CO2SYS) and the combined errors in pK_1 and pK_2 result in an error of about 0.004 pH units (Millero, 2007). As shown in Table 1.2 in Chapter 1, DIC and TA is not the best pair of parameters to calculate pH. The combination of pCO_2 with either DIC or TA would be a lot more favourable. The large error in pH calculated from DIC and TA is largely due to the uncertainty in the coefficient pK_2 (Millero, 2007).The discrepancy between measured pH and pH values calculated from DIC and TA values was 0.0011 ± 0.0011 (n=20). The method applied to correct for the indicator perturbation was therefore considered adequate. Finally, the thermistors were calibrated with an accuracy of 0.03°C resulting in a potential error in pH of 0.0004 pH units.

4.2.6. Cruise data

The automated pH system was operated continuously on the underway seawater supply for a month during the cruise D366 and more than 5000 pH data were obtained. Less than 30 mL of indicator was consumed over the duration of the cruise. Measurements were only interrupted for system performance checks and maintenance. Surface ocean pH data obtained during cruise D366 are presented in Chapter 5. Dissolved inorganic carbon data were used to calculate pH data at *in situ* temperature (Hunter, 1998). The magnitude of the correction was about 0.002 ± 0.001 pH units, whereas measurements at 25 °C would have required a correction of ca. 0.2 pH units. The determination of pH at temperatures close to the *in situ* values therefore significantly reduces the potential error introduced by the required temperature corrections. With our system, *in situ* pH can also be obtained using the linear regression proposed by Millero (dpH/dT= -1.582E-2) (Millero, 2007) which avoids the requirement of a second carbonate parameter. The difference

between the two methods to calculate pH at *in situ* temperature was about 0.0003 ± 3E-5 pH units.

4.3. Extension to mCP indicator: Results from the discrete sample pH system

The choice of which pH indicator to use depends on the indicator characteristics (particularly the acid dissociation constant pK_2) and on the expected pH of the sample to be analysed (see 3.3.3 Sulphonephtalein Indicators for more details). Being able to choose, on the same analytical pH system, which indicator to use depending on the application (e.g. seawater profiles, underway transects, samples from ocean acidification experiments) would be very useful. We show here that with an adapted indicator characterization, it is possible to use mCP indicator with our established Thymol Blue pH system without making any physical modifications to the instrument.

4.3.1. Use of the mCP indicator with the same LEDs as Thymol Blue

The main issue with the use of mCP indicator on our system is that the absorption peak of the basic form of indicator is at a shorter wavelength compared to Thymol Blue's absorption spectra. As a result the second LED spectrum is at longer wavelength than the absorption peak maximum of the indicator basic form (Figure 4.9).

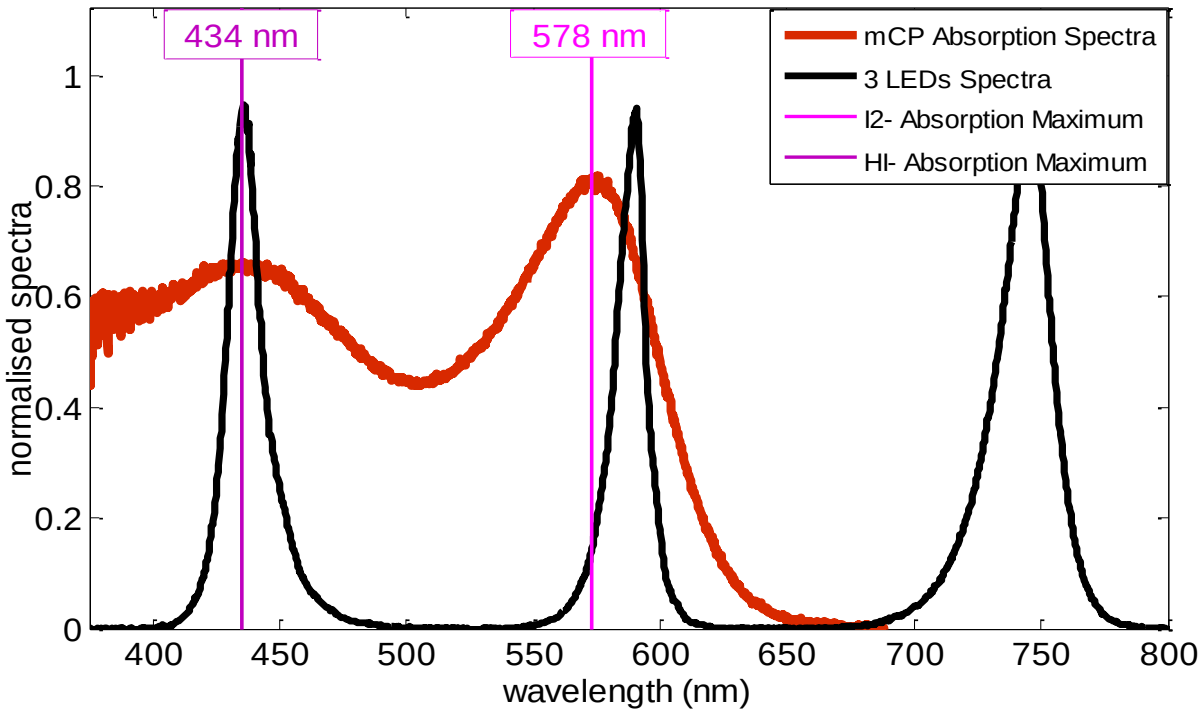

Figure 4.9: meta-Cresol Purple indicator and light source spectra.

Absorption spectra of the acidic and basic form of mCP indicator (in red) with their absorption maxima in pink. The light spectrum of the tri-coloured LED is shown in black.

The effect of the integration of the signal over the full LED peak on the sensitivity of the absorbance measurements was examined following the same method as detailed for Thymol Blue (see 4.2.3.1. Deviation due to the polychromatic light source). Integration over the full LED peak resulted in a positive deviation of the apparent absorbance at 578 nm compared to the peak absorbance obtained with the single maximum absorption wavelength (Figure 4.10). The linearity of the curves was verified using the range of the relative sensitivity as a function of the peak absorbance (Chan and Chan, 2001). The deviation observed and the noise in the data are due to the fact that the light spectra is relatively weak at 578 nm compared to the maximum LED output power peak at 596. The relative sensitivity ($S=A_{apparent}/A_{peak}$) is actually 1.15 when using a light source with higher intensity at 578 nm (Tungsten light source) to measure absorbance at the single wavelength 578 nm. The absorbance range is still in the linear range of Beer's law (within the ±5% tolerance range, Figures 4.10C and D). The use of mCP with the LEDs and integration of the signal on the full LED spectrum was therefore considered to be appropriate to calculate the absorbance values.

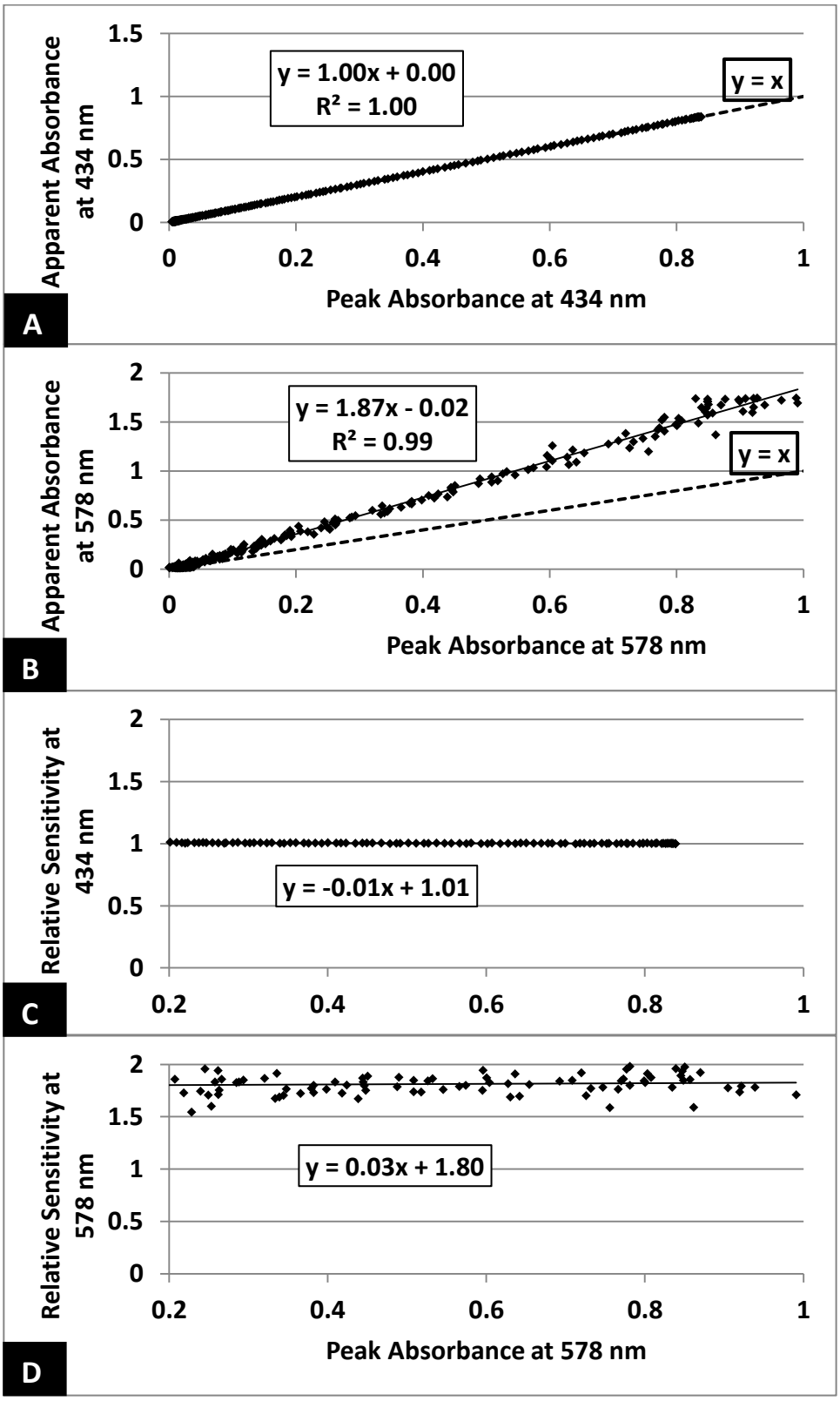

Figure 4.10: Sensitivity analysis.
A. and **B.** Apparent Absorbance (using the whole LED peak) versus Peak Absorbance (using a single pixel) for the LED centred on 435 nm and 596 nm respectively. The dotted line represents the case when the peak absorbance equals the apparent absorbance. **C.** and **D.** Linearity plots for the LED centred on 435 nm and 596 nm respectively. The line represents the linear case and the dotted lines represent the ±5% tolerance interval.

4.3.2. mCP indicator characterization

Characterization of the mCP extinction coefficients on the system has been performed at 25°C and salinity 35 using the same method as detailed for Thymol Blue indicator (see 4.2.2 Thymol Blue indicator characterisation). This work has been done under my supervision with Sara Fowell for her Master's Research Thesis. The extinction coefficient ratios (see Chapter 3 for definition) obtained by Sara are presented in Table 4.4.

Table 4.4: Extinction coefficient ratios of the mCP indicator on the pH system at 25°C and salinity 35.

mCP extinction coefficient ratio	
e1	0.0042
e2	2.1304
e3	0.1799

pK_2 was determined by measuring certified Tris buffer from Scripps at 25°C. Tris buffer has been analysed five times during the cruise JR271. The mean of the five measurements sessions resulted in pK_2=8.062 ± 0.005.

4.3.3. Discrete system precision and accuracy

The performance of the system has been evaluated through pH analysis at 25.0°C of two bottles of DIC/TA CRM (batch 117). The temperature was maintained within 0.01°C by placing the flow cell in a temperature controlled water bath. During the deployment of the instrument at sea, we obtained a short term precision of 0.001 pH unit (n=20) (Table 4.4). However, the discrepancy between pH measured and pH calculated from DIC and TA was about 0.018 pH units.

Table 4.5: Precision and accuracy of DIC/TA CRMs measurements

pH measured	Average discrepancy between pH(TA,DIC) and measured value for DIC/TA CRMs (n=20)	Precision (pH unit) of replicate DIC/TA CRMs analyses (n=20)	Date of analysis
7.9246	0.0184	0.0007	26/06/2012
7.9247	0.0183	0.0011	01/07/2012

Given the good precision and reproducibility of CRM measurements for the two dates of analysis, the large inaccuracy observed is probably due to uncertainties in the indicator coefficients characterization. Figure 4.11 shows the pH of a water column profile (CTD cast 42) measured during the RRS James Clark Ross cruise JR271. Measured pH and pH calculated from DIC and TA follow a very similar trend with depth. The varying discrepancy between the two data points at

each depth is probably due to the uncertainty in the extinction coefficient ratios as well as gas exchanges between sampling and analysis of the samples. Further work should be done to improve the characterization of the extinction coefficients by improving the laboratory setting as well as the data processing (iterative calculation between e_i and pK_2 in order to refine the parameters (Dickson et al., 2007)).

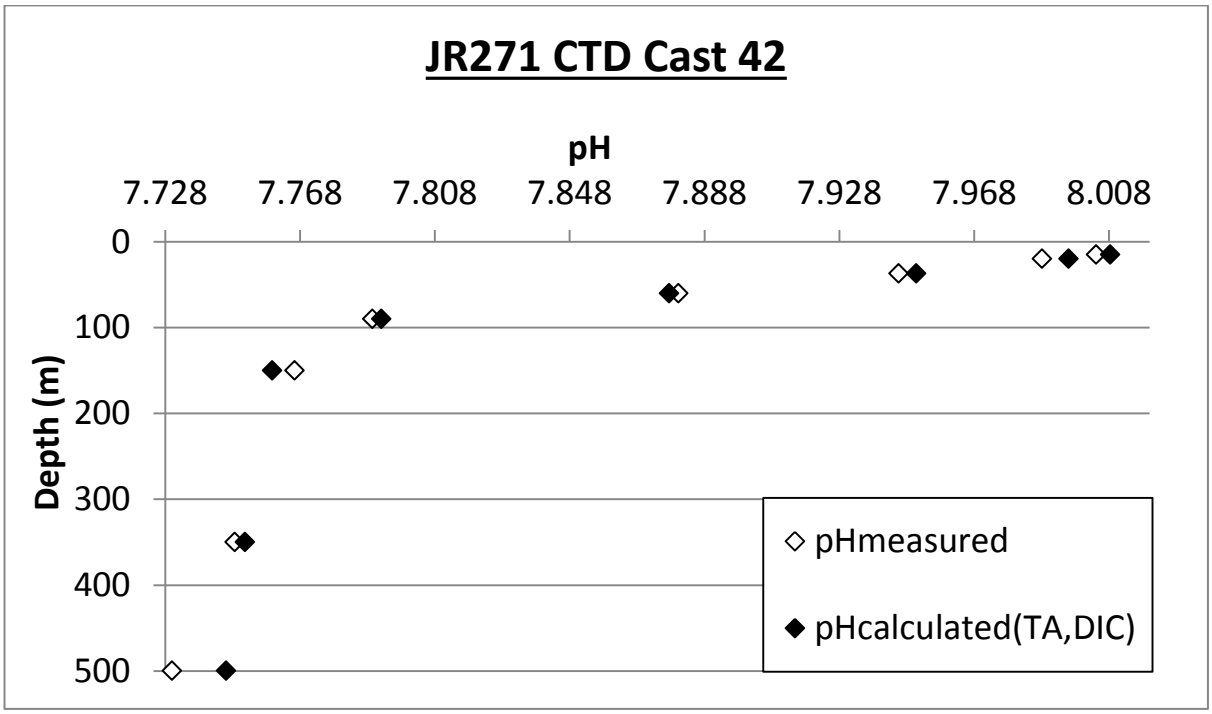

Figure 4.11: pH of a water column profile (CTD cast 42) measured during JR271. White squares are measured pH data and black squares are pH data calculated from DIC and TA (values provided by M. Humphreys).

4.4. Replacement of the spectrometer with a photodiode

4.4.1. Quasi-simultaneous measurements at three wavelengths with a single photodiode

A key step in the miniaturization of the pH system is to replace the Ocean Optics spectrophotometer with a photodiode. Photodiodes are much smaller, cheaper and more robust than USB spectrometers. Photodiodes can also be directly glued onto the chip, avoiding the use of an optical fibre. However, contrary to the spectrometers, photodiodes do not offer the possibility to resolve the spectral shape of the signal or to provide a narrow optical bandwidth. Instead, a single voltage output is obtained from the total light detected by the photodiode. Given that measurements are made continuously while the indicator slug passes through the absorption cell,

it is necessary to measure the three wavelengths simultaneously. Three approaches exist to measure the light signal at three different wavelengths with photodiodes:

1. Split the transmitted light and use three photodiodes with different filters to isolate optical power in three narrow wavelength bands of interest. This approach has been used on the SAMI-pH system (Seidel et al., 2008). The advantage of this method is that signals at the three wavelengths are recorded simultaneously but this set up is relatively complex and a significant amount of light can be lost when splitting the signal.
2. Modulate the LEDS at different frequencies and use a single photodiode. Each individual signal can be recovered by Fast Fourier Transform or other frequency domain demodulation scheme. The advantage of this method is that the set-up is very simple and signals at the three wavelengths are recorded simultaneously. Nevertheless, the strength of each signal is limited to a third of the total signal strength received by the photodiode. This has as a consequence that it reduces the sensitivity of the measurements.
3. Switch on/off one LED at a time. The set-up is very simple and the maximum signal strength is used for each wavelength. Additionally the signal processing is more straightforward than for method 2. Yet the three signals are not strictly recorded simultaneously. This issue can be overcome as detailed below and we chose to implement this approach on the pH system.

4.4.1.1. Frequency of the LED rotation

In order to measure signals as close to each other as possible at the three wavelengths, the three LEDs must be flashed as quickly as can be achieved while keeping stable signals. Several frequencies have been tested to find which configuration leads to the most stable signals. Table 4.6 compares the stability of the reference signal (no indicator) at 435 nm obtained for the different frequencies tested.

Table 4.6: Comparison of the stability of the reference signal (in volt) for different On/Off configurations

LED setting: ms On/ms Off	Standard deviation (volt)
64/64	0.008
104/64	0.002
144/16	0.003
184/16	0.009
224/16	0.003

The best signal stability was observed with the setting 104 ms On and 64 ms Off so this setting was chosen for the next experiments.

4.4.1.2. Observing 3 signals with a single photodiode

It is important for the correction of the indicator addition to obtain the data at 435 nm and at 596 nm at the same time. Although the three signals are neither measured continuously nor simultaneously, it is possible to recover the continuous signals by interpolating the observed signals. After interpolation, data points at the three wavelengths appear simultaneous. Figure 4.12 illustrates the steps undertaken to obtain the three signals simultaneously from a single photodiode voltage output. Once processed, signals very similar to the one observed with the spectrophotometer are obtained. The Schlieren effect is still observed at 750 nm. The data are then processed with the same method as detailed for the spectrophotometer.

4.4.2. Precision of the photodiode set up

Seawater samples have been analysed on the shipboard pH system with a single photodiode instead of the spectrometer and the microcontroller system to control the LEDs. Measurements were performed at 25°C in a water bath. The best linear fits to correct for the indicator addition were obtained with absorbance values ranging from 0.2 and 1.0 (RMS≈0.98). In 14 hours of measurements, the average short term precision (n=10) was 0.0054 pH units. But an important drift of -0.022 pH units in 14 hours was observed. This drift is probably due to a real pH reduction of the sample in the water bath. Drifts in light intensity were observed as well but these do not seem to be responsible for the drift in measured pH. In order to estimate the error due to the drift in intensity, data from the first pH sample have been processed using the reference signal from the last sample of the sequence. A discrepancy of 20 mpH was still observed between the first and the last sample of the sequence. Processing the data with a decreasing reference signal during the four minutes of measurement resulted in a correction smaller than 0.0001 pH units. Finally, analysis of Tris buffer (S=35) for more than 14 hours resulted in a drift smaller than -0.001 pH units despite similar drifts in intensity. The average short-term precision (n=10) with Tris buffer was 0.0043 pH units. Although the drifts in intensity will be an issue for long term measurements, they appear to have a negligible impact on the pH results here. The source of the drifts is probably due to instabilities in the set-up: small displacements of the optical fibres will have significant impacts on the signal output. Secondly some components (particularly the resistors) from the electronic board controlling the LEDs were not of very high quality. A better set-up correcting for these issues should improve the signal stability, the drifts in intensity and the measurement precision.

The accuracy of the set-up has not been estimated yet, as it is necessary to determine the extinction coefficients of the indicator for the new set-up using a photodiode.

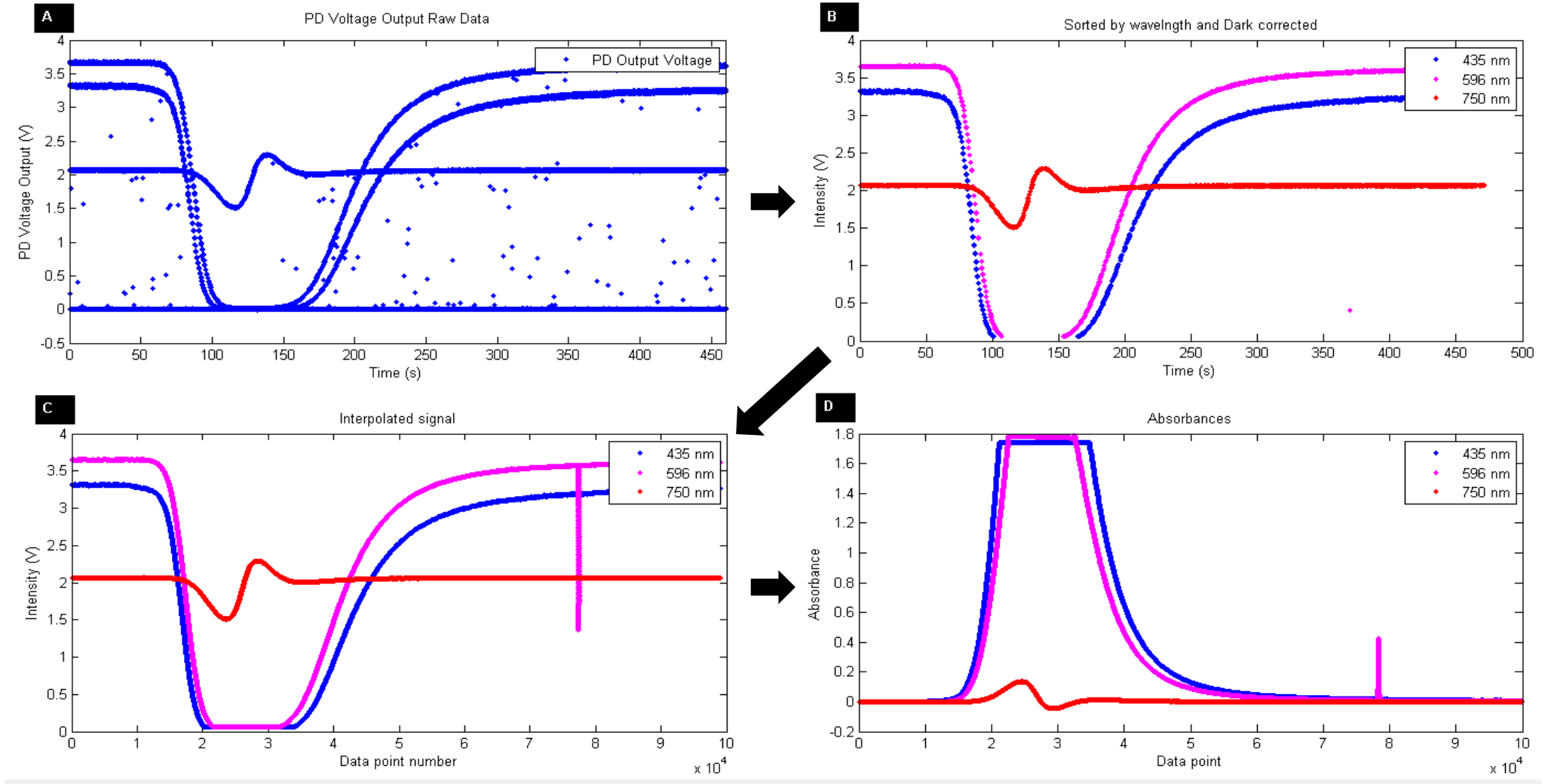

Figure 4.12: Processing steps to obtain the three signals simultaneously from a single photodiode voltage output.

4.5. Conclusion

The successful implementation of a simple microfluidic design with a low reagent consumption is a key step toward the miniaturisation of the colorimetric pH sensor. Less than 30 mL of indicator was consumed during a month of deployment at sea of the novel pH instrument. This is a great advantage for long term deployments on ships (e.g. on FerryBox systems, (Hydes et al., 2010)) or moorings. The system was demonstrated to be particularly adapted to shipboard deployment with high quality data obtained during a month long research cruise in European shelf waters. The system featured a short term precision of 0.001 pH unit (n=20) and an accuracy within the range of a certified Tris buffer (0.004 pH units). The optical set up was robust and relatively small with the use of an USB mini-spectrometer, a custom made polymeric flow cell and the LEDs light source. The simple design of this microfluidic platform proved to be very efficient as it enabled effective mixing of the indicator with the sample, and allowed pH measurements and correction of the indicator effect on the sample pH with a single addition of indicator. The single packaged three wavelengths LED showed the usual advantages of LEDs light sources (low cost, small, stable with relatively narrow spectrum) and had the additional advantage that it did not require coupling of the light from three separate LEDs. The integration of the signal over the whole of each LED peak reduced signal noise, and indicated the possibility to replace the current spectrophotometer with a small chip mountable mini-spectrophotometer featuring a lower wavelength resolution or with a photodiode. The pH measurement close to *in situ* temperature (+0.2 °C) in the sampling chamber greatly reduced the source of error due to the correction to *in situ* conditions. Two indicators, Thymol Blue and meta-Cresol Purple, can be used on the system with the same level of precision. Finally a smaller and very simple design is possible with the use of a single photodiode instead of the USB spectrophotometer. A precision of 0.004 pH units has been achieved with the photodiode which should be improved with straightforward amendments of the set-up.

References

Aris, R. (1956), On the dispersion of a solute in a fluid flowing through a tube, *Proceedings of the Royal Society of London. Series A. Mathematical and Physical Sciences*, *235*(1200), 67-77.

Byrne, R. H., S. Mecking, R. A. Feely, and X. Liu (2010), Direct observations of basin-wide acidification of the North Pacific Ocean, *Geophysical Research Letters*, *37*(2), L02601.

Caldeira, K., and M. E. Wickett (2005), Ocean model predictions of chemistry changes from carbon dioxide emissions to the atmosphere and ocean, *J. Geophys. Res*, *110*, 1-12.

Canadell, J. G., C. Le Quéré, M. R. Raupach, C. B. Field, E. T. Buitenhuis, P. Ciais, T. J. Conway, N. P. Gillett, R. Houghton, and G. Marland (2007), Contributions to accelerating atmospheric CO2 growth from economic activity, carbon intensity, and efficiency of natural sinks, *Proceedings of the National Academy of Sciences*, *104*(47), 18866-18870.

Chan, G. C. Y., and W. T. Chan (2001), Beer's Law Measurements Using Non-monochromatic Light Sources A Computer Simulation, *Journal of Chemical Education*, *78*(9), 1285-1288.

Chatwin, P., and P. J. Sullivan (1982), The effect of aspect ratio on longitudinal diffusivity in rectangular channels, *Journal of Fluid mechanics*, *120*(1), 347-358.

Chierici, M., A. Fransson, and L. G. Anderson (1999), Influence of m-cresol purple indicator additions on the pH of seawater samples: Correction factors evaluated from a chemical speciation model, *Marine Chemistry*, *65*(3-4), 281-290.

Clayton, T., and R. Byrne (1993), Spectrophotometric seawater pH measurements: total hydrogen ion concentration scale calibration of m-cresol purple and at-sea results, *Deep-sea research. Part 1. Oceanographic research papers*, *40*(10), 2115-2129.

Datta, S., and S. Ghosal (2009), Characterizing dispersion in microfluidic channels, *Lab Chip*, *9*(17), 2537-2550.

DelValls, T. A. (1999), Underway pH measurements in upwelling conditions: The California current, *Ciencias Marinas*, *25*(3), 345-365.

Dias, A. C. B., E. P. Borges, E. A. G. Zagatto, and P. J. Worsfold (2006), A critical examination of the components of the Schlieren effect in flow analysis, *Talanta*, *68*(4), 1076-1082.

Dickson, A., and F. Millero (1987), A comparison of the equilibrium constants for the dissociation of carbonic acid in seawater media, *Deep Sea Research Part A. Oceanographic Research Papers*, *34*(10), 1733-1743.

Dickson, A. G. (1990), Standard potential of the reaction: AgCl(s) + 12H2(g) = Ag(s) + HCl(aq), and and the standard acidity constant of the ion HSO4− in synthetic sea water from 273.15 to 318.15 K, *The Journal of Chemical Thermodynamics*, *22*(2), 113-127.

Dickson, A. G., C. L. Sabine, and J. R. Christian (2007), Guide to best practices for ocean CO2 measurements, *PICES special publication*, *3*.

Doney, S. C. (2010), The growing human footprint on coastal and open-ocean biogeochemistry, *Science*, *328*(5985), 1512.

Doney, S. C., B. Tilbrook, S. Roy, N. Metzl, C. Le Quéré, M. Hood, R. A. Feely, and D. Bakker (2009), Surface-ocean CO2 variability and vulnerability, *Deep Sea Research Part II: Topical Studies in Oceanography*, *56*(8-10), 504-511.

Dore, J. E., R. Lukas, D. W. Sadler, M. J. Church, and D. M. Karl (2009), Physical and biogeochemical modulation of ocean acidification in the central North Pacific, *Proceedings of the National Academy of Sciences*, *106*(30), 12235.

Doshi, M. R., P. M. Daiya, and W. N. Gill (1978), Three dimensional laminar dispersion in open and closed rectangular conduits, *Chemical engineering science*, *33*(7), 795-804.

Dutta, D., and D. T. Leighton Jr (2001), Dispersion reduction in pressure-driven flow through microetched channels, *Analytical Chemistry*, *73*(3), 504-513.

Dutta, D., A. Ramachandran, and D. T. Leighton (2006), Effect of channel geometry on solute dispersion in pressure-driven microfluidic systems, *Microfluidics and Nanofluidics*, *2*(4), 275-290.

Edwards, D. A., and H. Brenner (1993), *Macrotransport processes*, 744 pp., Butterworth-Heinemann.

Friis, K., A. Körtzinger, and D. W. R. Wallace (2004), Spectrophotometric pH measurement in the ocean: Requirements, design, and testing of an autonomous charge-coupled device detector system, *Limnol. Oceanogr. Methods*, *2*, 126-136.

González-Dávila, M. (2010), The water column distribution of carbonate system variables at the ESTOC site from 1995 to 2004, *Biogeosciences*, *7*, 1995-2032.

Guell, D. C., R. Cox, and H. Brenner (1987), TAYLOR DISPERSION IN CONDUITS OF LARGE ASPECT RATIO†, *Chemical Engineering Communications*, *58*(1-6), 231-244.

Hartley, G., and C. Robinson (1931), The Diffusion of Colloidal Electrolytes and Other Charged Colloids, *Proceedings of the Royal Society of London. Series A*, *134*(823), 20.

Hauser, P. C., T. W. T. Rupasinghe, and N. E. Cates (1995), A multi-wavelength photometer based on light-emitting diodes, *Talanta*, *42*(4), 605-612.

Hunter, K. A. (1998), The temperature dependence of pH in surface seawater, *Deep Sea Research Part I: Oceanographic Research Papers*, *45*(11), 1919-1930.

Hydes, D., F. Colijn, W. Petersen, F. S. D. K. Mills, D. Durand, and B. N. NIVA (Eds.) (2010), *The way forward in developing and integrating FerryBox technologies*, ESA Publication WPP-306.

Intergovernmental Panel on Climate, C., C. W. Team, R. K. Pachauri, and A. e. Reisinger (2007), *IPCC, 2007: Climate Change 2007: Synthesis Report. Contribution of Working Groups I, II and III to the Fourth Assessment Report of the Intergovernmental Panel on Climate Change*, 104 pp., IPCC, Geneva, Switzerland.

Johnson, K. S., W. M. Berelson, E. S. Boss, Z. Chase, H. Claustre, S. R. Emerson, N. Gruber, A. Kortzinger, M. J. Perry, and S. C. Riser (2009), Observing biogeochemical cycles at global scales with profiling floats and gliders: Prospects for a global array, *Oceanography*, 216-225.

Lenher, S., and J. E. Smith (1936), A Diffusion Study of Dyes, *The Journal of Physical Chemistry*, *40*(8), 1005-1020.

Liu, X., M. C. Patsavas, and R. H. Byrne (2011), Purification and Characterization of meta-Cresol Purple for Spectrophotometric Seawater pH Measurements, *Environmental Science & Technology*, 4862–4868.

Martz, T. R., J. J. Carr, C. R. French, and M. D. DeGrandpre (2003), A submersible autonomous sensor for spectrophotometric pH measurements of natural waters, *Analytical Chemistry*, *75*(8), 1844-1850.

Mehrbach, C., C. H. Culberson, J. E. Hawley, and R. M. Pytkowicz (1973), Measurement of the apparent dissociation constants of carbonic acid in seawater at atmospheric pressure, *Limnology and Oceanography*, 897-907.

Millero, F. J. (2007), The marine inorganic carbon cycle, *Chemical Reviews*, *107*(2), 308-341.

Ogilvie, I., V. Sieben, M. Mowlem, and H. Morgan (2011), Temporal optimisation of microfluidic colourimetric sensors using a novel multiplexed stop-flow architecture, *Analytical Chemistry*, 4814–4821.

Ohline, S. M., M. R. Reid, S. L. G. Husheer, K. I. Currie, and K. A. Hunter (2007), Spectrophotometric determination of pH in seawater off Taiaroa Head, Otago, New Zealand: Full-spectrum modelling and prediction of pCO2 levels, *Marine Chemistry*, *107*(2), 143-155.

Pierrot, D., E. Lewis, and D. W. R. Wallace (2006), MS Excel Program Developed for CO2 System Calculations. ORNL/CDIAC-105a. Carbon Dioxide Information Analysis Center, edited by U. S. D. o. E. Oak Ridge National Laboratory, Oak Ridge, Tennessee.

Prien, R. D. (2007), The future of chemical in situ sensors, *Marine Chemistry*, *107*(3), 422-432.

Rérolle, V. M. C., C. F. A. Floquet, M. C. Mowlem, D. P. Connelly, E. P. Achterberg, and R. R. G. J. Bellerby (2012), Seawater-pH measurements for ocean-acidification observations, *TrAC Trends in Analytical Chemistry*, *40*(0), 146-157.

Robinson, C. (1935), The Diffusion Coefficients of Dye Solutions and their Interpretation, *Proceedings of the Royal Society of London. Series A, Mathematical and Physical Sciences*, *148*(865), 681-695.

Sabine, C. L., R. A. Feely, N. Gruber, R. M. Key, K. Lee, J. L. Bullister, R. Wanninkhof, C. S. Wong, D. W. R. Wallace, and B. Tilbrook (2004), The oceanic sink for anthropogenic CO2, *Science*, *305*(5682), 367-371.

Seidel, M. P., M. D. DeGrandpre, and A. G. Dickson (2008), A sensor for in situ indicator-based measurements of seawater pH, *Marine Chemistry*, *109*(1-2), 18-28.

Squires, T. M., and S. R. Quake (2005), Microfluidics: Fluid physics at the nanoliter scale, *Reviews of modern physics*, *77*(3), 977.

Taylor, G. (1953), Dispersion of Soluble Matter in Solvent Flowing Slowly through a Tube, *Proceedings of the Royal Society of London. Series A. Mathematical and Physical Sciences*, *219*(1137), 186-203.

Wang, Z. A., X. Liu, R. H. Byrne, R. Wanninkhof, R. E. Bernstein, E. A. Kaltenbacher, and J. Patten (2007), Simultaneous spectrophotometric flow-through measurements of pH, carbon dioxide fugacity, and total inorganic carbon in seawater, *Analytica Chimica Acta*, *596*(1), 23-36.

Wooding, R. (1960), Instability of a viscous liquid of variable density in a vertical Hele-Shaw cell, *Journal of Fluid mechanics*, *7*(04), 501-515.

Yao, W., X. Liu, and R. H. Byrne (2007), Impurities in indicators used for spectrophotometric seawater pH measurements: Assessment and remedies, *Marine Chemistry*, *107*(2), 167-172.

Zhang, H., and R. H. Byrne (1996), Spectrophotometric pH measurements of surface seawater at in-situ conditions: absorbance and protonation behavior of thymol blue, *Marine Chemistry*, *52*(1), 17-25.

Chapter 5: Controls on pH in surface waters of Northwest European shelf seas

5.1. Introduction

Oceans form an important sink of atmospheric carbon dioxide (CO_2), thereby significantly buffering climate change. About 28% of the CO_2 emitted between 1959 and 2006 has been taken up by the oceans (Canadell et al., 2007). However with increasing atmospheric CO_2 concentrations, questions arise on whether oceans are able to maintain their current rate of CO_2 uptake or if their capacity to absorb CO_2 is decreasing while ocean waters reach higher dissolved inorganic carbon (DIC) levels. The capacity of the oceans to sequester CO_2 depends on the role of biological (soft tissue and carbonate) and solubility pump processes in altering CO_2 concentrations in the surface ocean (Volk and Hoffert, 1985). The oceanic carbonate system is affected by physical and biological processes leading to seasonal and geographical variations. Coastal seas have been recently recognized as a potentially significant sink of CO_2 (0.2 PgC/yr) due to their high biological activities resulting in a net off shelf transport at depth to the adjacent deep ocean regions (shelf sea carbon pump) (Borges et al., 2005;Chen and Borges, 2009;Thomas et al., 2004). Coastal environments are dynamic, subject to a range of interacting processes with contrasting effects on the marine carbonate chemistry and therefore on the capacity of coastal seas to absorb CO_2.

pH is one of the four parameters (DIC, total alkalinity (TA) and partial pressure of CO_2 (pCO_2)) used to study the carbonate system. The main factors affecting carbonate chemistry in coastal water are biological activity, temperature changes and discharge of river water (Thomas et al., 2005). Photosynthesis decreases the concentration of DIC and free protons and therefore leads to an increase in pH, whereas the reverse processes of respiration and remineralisation lead to a decrease in pH. Temperature changes affect the carbonate equilibrium constants (Mehrbach et al., 1973). A rise in temperature triggers a shift in the marine carbonate system resulting in a decrease in pH. But an increase in temperature will also enhance the water column stratification and primary productivity (Eppley, 1972). The water column stratification enables the export of organic matter out of the surface layer and results therefore in an increase in surface water pH. Riverine inputs can have differing effects on pH. Rivers can result in direct changes in coastal carbonate chemistry through the discharge of high DIC and low TA freshwaters (Thomas et al., 2005;Borges and Gypens, 2010;Gypens et al., 2011). Additionally, riverine inputs can have indirect effects through stimulation of primary productivity by addition of nutrients, resulting in an increase in pH, whereas respiration of riverine organic matter will decrease pH (Frankignoulle et al., 1998). Localised upwelling at shelf breaks of relatively acidic DIC-rich waters can also significantly decrease pH while simultaneously enhancing primary productivity through nutrient supply (Feely et al., 2008). Finally anthropogenic atmospheric inputs of CO_2, HNO_3 and H_2SO_4 will

decrease seawater pH (Doney et al., 2007). The high spatial and temporal variability in surface seawater carbonate chemistry has led to contradicting estimates of air-sea CO_2 fluxes in coastal seas. Most of the processes affecting the carbonate system are usually occurring simultaneously, making it challenging to understand and determine the main drivers of the dynamics of the carbonate chemistry in coastal seas. This highlights the need for datasets with high spatial and temporal resolution to unravel the various processes and their consequences on the carbonate system.

The carbonate chemistry in the English Channel and the North Sea has been well studied and particularly air-sea CO_2 fluxes using pCO_2 data are widely reported (Thomas and Borges, 2012;Kitidis et al., 2012). The North Sea has been shown to be a sink for atmospheric CO_2 with export of DIC to the deep North Atlantic (Thomas et al., 2005). Thomas and co-workers studied the controls of the surface water pCO_2 in the North Sea and found that biological activity was the main driver of the seasonal pCO_2 variability in the northern and central part of the North Sea. The pCO_2 variability in the southern part was mainly driven by temperature variations. The fully mixed waters of the southern region were a source of CO_2 to the atmosphere, apart from spring when primary production was more important for pCO_2 levels than the effect of the temperature increase. Gypens and colleagues observed a similar seasonal variability in the English Channel and the Southern Bight of the North Sea with a seasonal and inter-annual antagonism between biological and temperature effects on pCO_2 (and pH) (Gypens et al., 2011). In brief, surface water pH increases in winter and spring/early summer due to temperature decrease (winter) and biological activity (spring). Surface water pH decreases in summer and autumn due to temperature increase and remineralisation of organic matter. They also show that the competition between temperature and biological controls can be strongly affected by riverine nutrient inputs which enhance biological activity.

We present here a new set of surface water pH data determined in the North West European Shelf Seas in summer 2011. It is the first time that pH has been measured at a high spatial resolution (10 Measurements.h^{-1}) in this wide Shelf Seas area. The aim is to study the dynamics in carbonate chemistry of the Shelf Seas surface waters using pH data. The large variability in the water masses and natural conditions sampled due to the very dynamic environment met on coastal shelves constitute a clear challenge for the interpretation of the observed data. An additional difficulty is that the samples have not only been sampled at different location but also at various time of the day. The sampling time can have a strong impact on surface water pH and particularly in bloom areas (Thomas and Borges, 2012). We used a statistical approach to investigate which processes affect pH and their relative importance in explaining the observed pH

variance along the ship's transect. Our aim is to explain pH dynamics using solely underway pH, temperature, salinity, and fluorescence data. Data interpretation is supported by lower resolution surface water DIC, TA, and nutrient data, in addition to further variables (e.g. dissolved organic matter) determined only at CTD sampling stations.

5.2. Method

5.2.1. Cruise

The data used in this study have been collected in the period between 06/06/2011 and 07/07/2011 during the RRS *Discovery* research cruise D366 in Northwest European Shelf waters. The track of the ship is presented in Figure 5.1. The cruise was the first cruise of the UK Natural Environment Research Council Ocean Acidification Research Program. The four parameters of the carbonate system (DIC, TA, pCO_2 and pH) were determined with a high spatial resolution. We were able to check the quality of the data and ensure a high quality of our data set by over-constraining the carbonate system.

5.2.2. Hydrography of the Northwest European Shelf seas

The transect of cruise D366 was on the northwest European shelf, with an additional section in the Bay of Biscay (Figure 5.1). The Northwest European shelf seas are generally shallower than 250 m apart from the deep Norwegian Trench (Figure 5.2). This trench extends from the Skagerrak to the open Atlantic Ocean northeast of the Shetland Islands. In the Skagerrak Strait depth reach 700 m. The southern North Sea is shallower than 50 m and increases in depth towards the north down to approximately 150 m. The Celtic Sea and the English Channel increase in depth towards the shelf edge with the Atlantic Ocean. The Irish Sea is semi-enclosed, with a shallow eastern part (generally less than 80 m deep), and a deeper north-south trending trough as deep as 250 m. The Irish Sea communicates with the Atlantic Ocean via the Malin Sea to the northwest and the Celtic Sea to the southwest.

The North Sea is dominated by an anti-clockwise current along the edges, with Atlantic waters coming mainly from the northwest opening but also to a lesser extent from the English Channel and leaving along the Norwegian coast via the Norwegian Trench (OSPAR Commission, 2000). Tidal currents can be stronger than the residual current in many areas and cause important mixing in the water column. Additionally, the study area is influenced by important riverine freshwater inputs from the Seine and Somme rivers in the English Channel, the Thames, Sheldt, Meuse/Rhine, Ems and Elbe rivers in the Southern North Sea. The annual freshwater river input in the North Sea is on the order of 300 km^3, with one-third coming from the snow-melt waters of Norway and Sweden and the rest from major rivers (OSPAR Commission, 2000). In

addition, the vast amount of brackish waters of the adjacent Baltic Sea is the dominant fresh water source for the North Sea via the Skagerrak Strait. The northern North Sea is seasonally stratified enabling net export of carbon and nutrient to the deeper layer (Thomas et al., 2005), whereas the shallow southern North Sea is continuously mixed throughout the year receiving the majority of the riverine fresh water inputs to the North Sea.

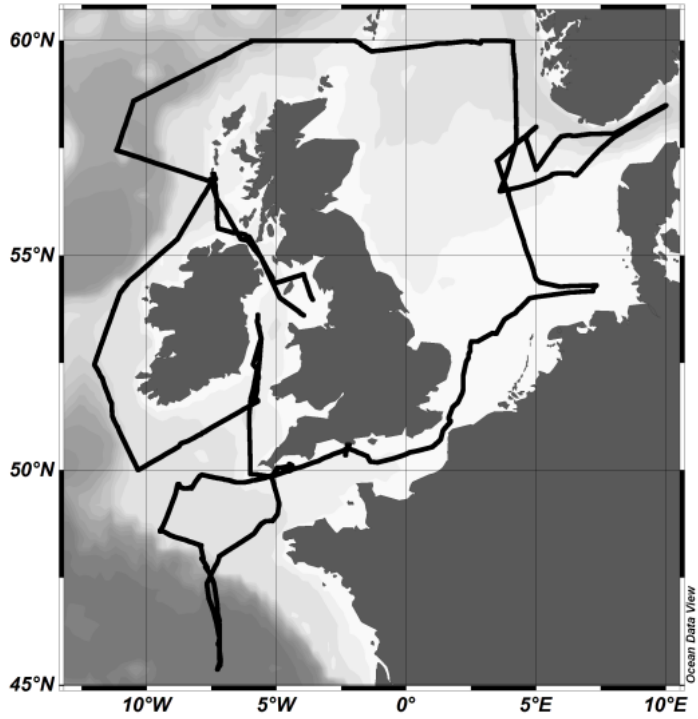

Figure 5.1: Map of the ship track during the cruise D366.

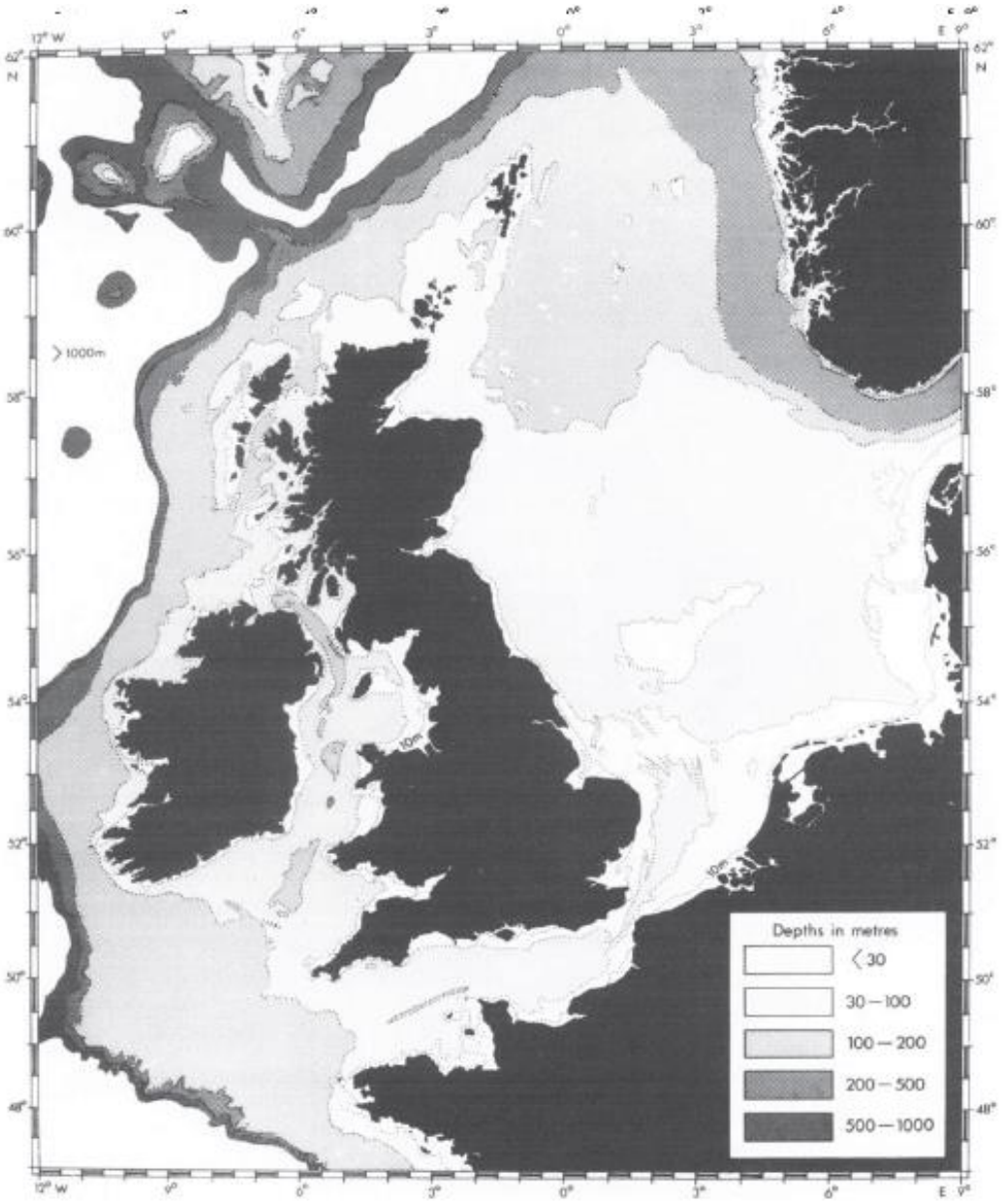

Figure 5.2: Bottom topography of the northwest European continental shelf. Map from (Pingree et al., 1978).

5.2.3 Data

5.2.3.1. Underway measurements

Surface water pH was measured continuously with an automated instrument connected to the underway water supply from the ship which has an intake at approximately 5 m depth. The automated pH system was operated continuously on the underway seawater supply in the period between 06/06/2011 and 07/07/2011. The instrument was developed in Southampton (Rérolle et al., submitted;Rérolle et al., 2013) and is based on the colorimetric method from Clayton and Byrne using Thymol Blue as pH indicator (Clayton and Byrne, 1993;Rérolle et al., 2012a;Rérolle et

al., 2012b). pH was determined on the total pH scale. Measurements were made every 6 minutes with a precision of 1 mpH. Three bottles of Tris buffer provided by Marine Physics Laboratory of Scripp's Institute of Oceanography, University of San Diego were analysed at the beginning, the middle and the end of the cruise to check the quality of the pH measurements. The indicator extinction coefficients were determined after the cruise on the instrument, for the salinity and temperature ranges observed during the cruise and pK_2 from Zhang and Byrne was used (Zhang and Byrne, 1996). Measurements were made at in situ T+0.2 °C.

pCO_2 measurements were made with the instrument *Live pCO_2* operated by Plymouth Marine Laboratory (Hardman-Mountford et al., 2008). The system functioned with a shower-head equilibrator and an infrared gas analyser (LICOR, LI-840). Measurements were referenced against standard CO_2 gases.

Continuous temperature (T), conductivity and chlorophyll-*a* fluorescence (Chl) data were obtained from the ThermoSalinoGraph (TSG) installed on the ship's underway supply.

5.2.3.2. Discrete underway water samples

Discrete seawater samples for DIC, TA and nutrients were collected every two hours from the underway supply. Discrete water samples for salinity (S) were also collected every four hours in order to calibrate the conductivity measurements. Discrete salinity samples were analysed by Jeff Benson (NOC, Southampton), using an Autosal salinometer (Guildline).

The DIC and alkalinity samples were collected using standard protocols (ref) in 250 ml glass bottles with ample rinsing and overflowing to avoid gas exchange with the air, and subsequently poisoned with a saturated mercuric chloride solution. Underway water samples were analysed for DIC and TA using a VINDTA 3C instrument at 25°C (#4, (Mintrop, 2004)) by Dorothee Bakker and Gareth Lee from UEA. Total alkalinity was determined by titration of seawater with a strong acid, whilst following the potential of a proton sensitive electrode; DIC was determined using a coulometer to determine the amount of CO_2 released following addition of phosphoric acid to the sample (Johnson et al., 1987). Measurements were calibrated using certified reference material from Scripps.

Analysis of nitrate and nitrite (total oxidised nitrogen, TON), phosphate (PO_4^{3-}) and silicate (SiO_4^{4-}) was undertaken by Mark Stinchcombe (NOC, Southampton) on a segmented flow auto-analyser (Skalar San+) following methods described by Kirkwood (Kirkwood, 1989). Samples were stored in 25 ml polycarbonate vials and kept refrigerated at approximately 4°C until nutrient analysis (within twelve hours after sampling).

5.2.3.3. CTD parameters

Dissolved oxygen (O_2) was determined by automated Winkler titration with photometric endpoint detection (Carritt and Carpenter, 1966). Dissolved organic carbon (DOC) samples were analysed by Ting Ting Shi (NOC, Southampton) using a high temperature combustion technique (Badr et al., 2003).

5.2.4. Study regions (determination of the sub-regions)

The dataset has been split into eleven regions which were defined using geographical and water masses characteristics (Figure 5.3). A MANOVA was performed with pH, T and S to determine whether the regions were statistically different (t-test, $p<0.05$). The regions 4 and 11 were relatively small and corresponded to regions where deep water had been locally brought to the surface by storm or shelf mixing. No statistical analysis has been performed with the data from these regions.

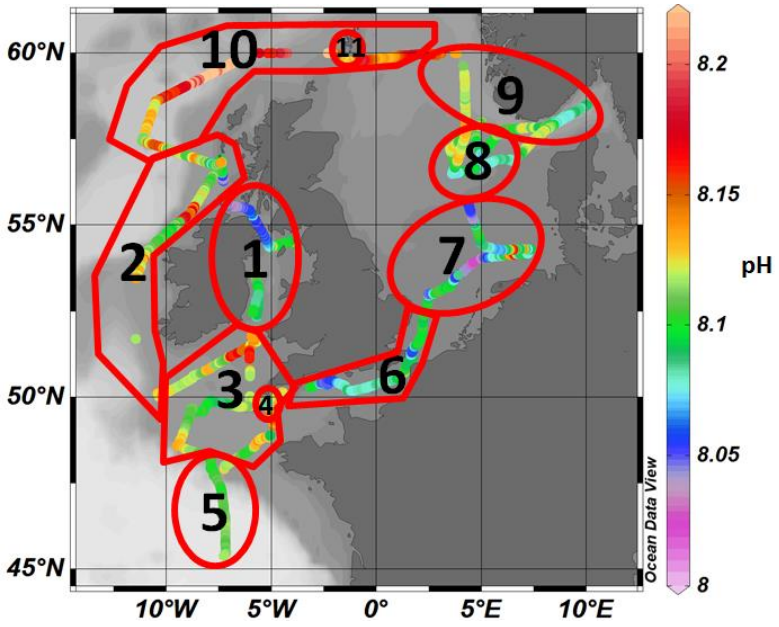

Figure 5.3: The 11 study regions defined on geographical and water mass (T-S) characteristics.

5.2.5. Statistical approach

In order to perform statistical analyses on the data, all the parameters have been transformed to obtain a normal distribution and standardised (centred and scaled to 1). Distributions of TON and PO_4^{3-} were strongly positively skewed even after transformation. The data analysis has been performed using the software Matlab®.

A stepwise multi-linear regression to relate pH data to environmental parameters has first been performed with all the data points from the surface samples of CTD stations with the following

parameters: DOC, O_2, S, T, Chl, SiO_4 and TON. The same stepwise multi-linear regression has been performed again but without O_2.

In addition, multi-linear regressions have been performed to relate the pH data in each individual region with the underway parameters S, T and Chl. And finally, stepwise multi-linear regressions have been performed with the underway variables S, T, Chl, SiO_4 and TON which were obtained at lower spatial resolution.

5.3. Results and discussion

5.3.1. Non-carbonate data distributions

Mean values and standard deviations per regions of S, T, TON, SiO_4, and Chl are presented in Table 5.1. Salinity varied between 33.2 and 35.8 during the cruise transect apart from the Skagerrak area where salinity was as low as 26.4. Lowest salinities were observed in the Celtic Sea (region 1), the southern North Sea (region 7) and the Skagerrak area (region 9). Temperature varied between 10.3 and 17.1 °C with lowest temperatures observed at the start of the cruise around Ireland (regions 1 and 2) and in region 11. Highest temperatures were observed in the southernmost part of the cruise transect in the Bay of Biscay (region 5), the southern North Sea (region 7) and the Skagerrak area (region 9). TON and SiO_4 varied between 0.1 and 5.34 µM with lowest concentrations observed south to Ireland (region 3) and in the northern part of the transect (regions 8, 9 and 10). Highest nutrients concentrations were observed in regions 1, 2 and 11. Chl levels varied between 0.12 and 1.54 µg/L. Highest levels of chlorophyll were observed in the north-west part of the transect regions 2 and 10 whereas the lowest levels were observed in regions 8 and 9.

Table 5.1: Mean values and standard deviations of S, T, TON, SiO_4 and Flc per regions.

Region	Mean S (PSU)	std S (PSU)	Mean T (°C)	std T (°C)	Mean NO_3 (µM)	std NO_3 (µM)	Mean PO_4 (µM)	std PO_4 (µM)	Mean SiO_2 (µM)	std SiO_2 (µM)	Mean Chl (µg/L)	std Chl (µg/L)
1	34.11	0.23	11.06	0.60	1.32	1.15	0.24	0.10	1.51	0.93	0.30	0.11
2	35.14	0.23	11.34	0.11	3.15	1.71	0.21	0.10	2.00	0.64	0.59	0.24
3	35.24	0.14	13.63	0.40	0.10	0.00	0.06	0.06	1.12	0.92	0.20	0.07
4	35.38	0.06	13.59	0.94	0.63	0.92	0.06	0.04	0.58	0.54	0.39	0.20
5	35.65	0.10	14.55	0.59	0.80	0.64	0.08	0.04	1.06	0.24	0.43	0.27
6	35.09	0.11	14.09	0.29	0.90	0.74	0.06	0.03	1.97	0.41	0.38	0.09
7	34.28	0.44	14.99	0.65	1.07	1.58	0.07	0.05	1.56	1.34	0.31	0.16
8	34.86	0.14	13.68	0.26	0.17	0.03	0.04	0.08	0.42	0.33	0.20	0.05
9	30.88	2.09	14.69	1.24	0.18	0.06	0.03	0.03	0.15	0.10	0.30	0.07
10	35.25	0.16	12.50	0.31	0.55	0.71	0.06	0.05	0.44	0.29	0.63	0.41
11	35.31	0.01	10.95	0.10	3.89	0.54	0.33	0.04	1.61	0.44	0.43	0.04

5.3.2. Distribution and Quality of the carbonate data

Data were corrected, to *in situ* temperature using the DIC data (Hunter, 1998). pH and DIC data are used to calculate TA. DIC and TA are not temperature dependent and can be used to calculate pH at the in situ oceanic temperature using thermodynamic relationships. A linear relationship between pH and temperature was derived from this correction and used to calculate pH at *in situ* temperature (dpH=-0.0153dT - 0.0002, Figure 5.4) where no DIC value was available. The magnitude of the correction was about 0.002 ± 0.001 pH units. Another correction of +0.004 pH units has been applied to the data to correct for the error due to the Schlieren effect (see Chapter 4.2.4.3. Deviation due to Schlieren effect).

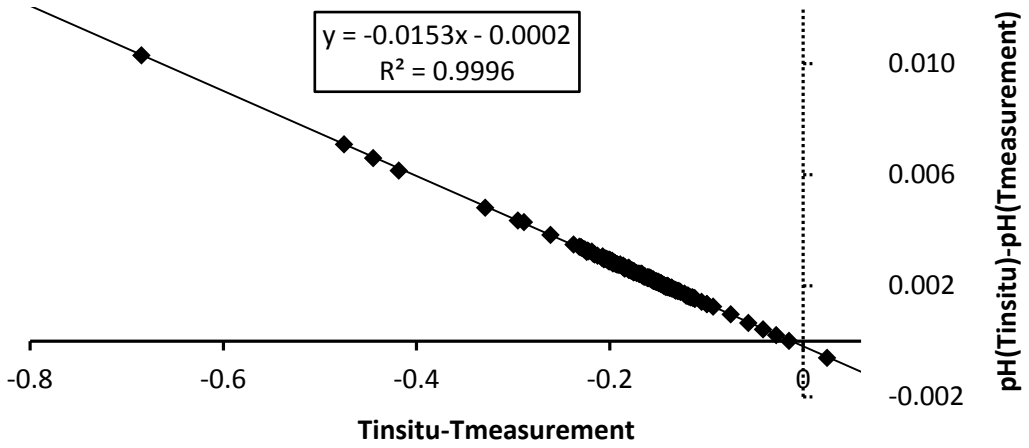

Figure 5.4: $pH_{Tinsitu}$-$pH_{Tmeasurement}$ versus T_{insitu}-$T_{measurement}$.

A comprehensive quality check and comparison between the different carbonate parameter datasets has been performed by Dr. Mariana Ribas Ribas (Ribas Ribas, 2012). A good agreement was found between all datasets. Comparison of measured pH with pH calculated from a pair of the carbonate parameters DIC, TA and pCO_2 (e.g. $pH_{DICpCO2}$) showed a mean discrepancy between 0.001 and 0.009 pH units.

Surface seawater pH along the transect ranged between 7.995 and 8.21 (Figure 5.5), with highest values in the northern North Sea where waters had enhanced Chl (up to 1.6 µg/L) concentrations and lower temperatures ($Tmean_{region10}$=12.5±0.3 °C). Lowest pH values were observed in the central North Sea in a well-mixed water column with enhanced dissolved organic carbon concentrations (up to 90 µM compared with 65 µM in the northern North Sea) and associated enhanced organic matter respiration with a consequent decrease in pH. Surface pCO_2 data varied

between 220 and 436 µatm. pH and pCO_2 variations during the cruise are shown on Figure 5.6. pH showed a typical anti –correlation with pCO_2 (Figures 5.7 and 5.8).

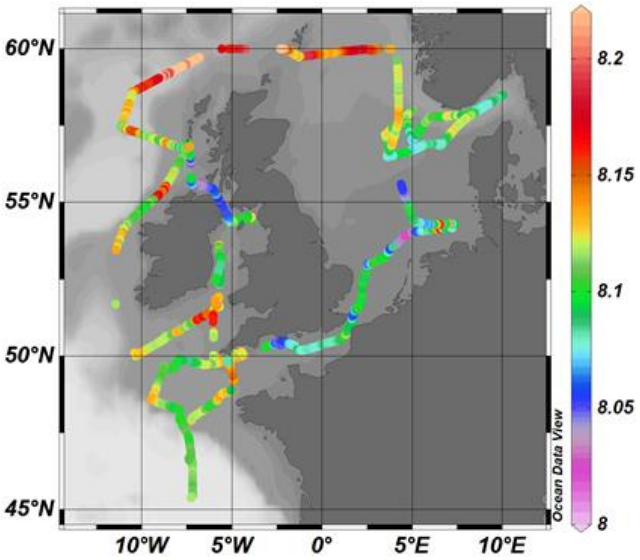

Figure 5.5: Map of surface water pH_{tot} in European shelf waters determined during research cruise D366.

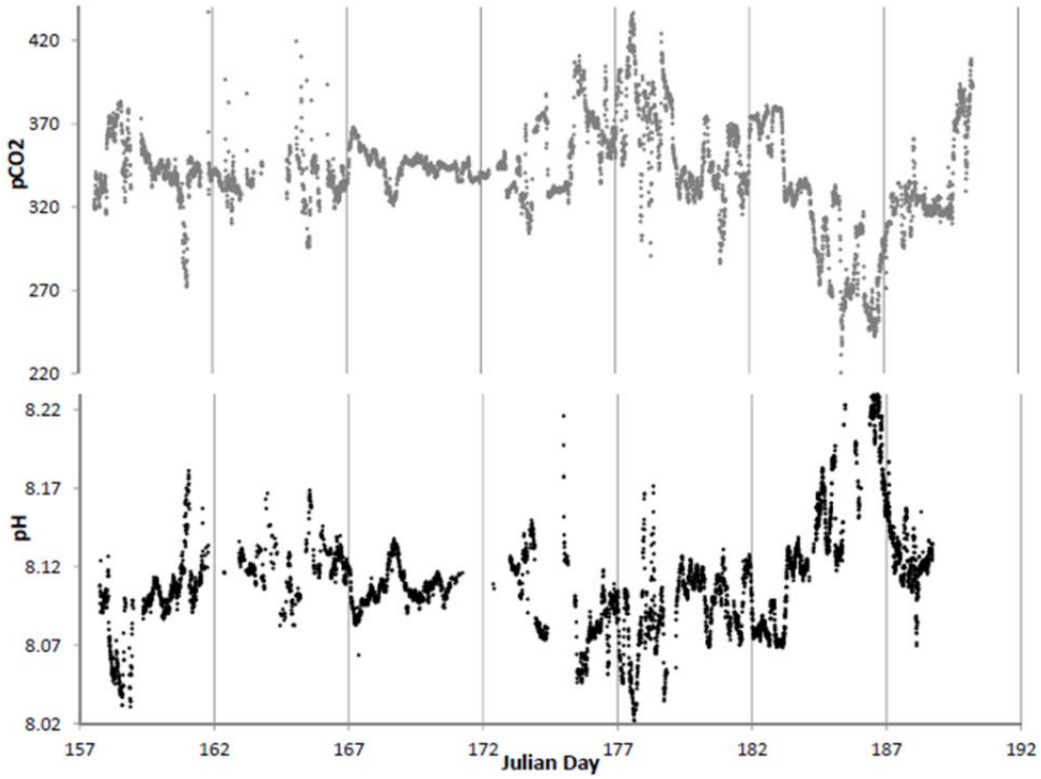

Figure 5.6: Sea surface pCO_2 and pH determined during the cruise D366.

The pH-pCO_2 variations were controlled by temperature variations, biological activity, calcification, gas exchanges and dilution processes (e.g. rain fall). The impacts of these processes

on the pH-pCO_2 relationship are illustrated in Figure 5.7A , adapted from Cullison Gray and co-workers (Cullison-Gray et al., 2011).

The pH and pCO_2 data measured in the North West European Shelf Seas in summer 2011 agreed well with the range of pH and pCO_2 results observed in Monterey Bay in summer 2007 (Figure 5.7B). The relationship between pCO_2 and hydrogen ions concentration can be simplified to $DIC \approx K_1 K_0 pCO_2/[H^+]$ with K_1 and K_0 the CO_2 solubility and first dissociation constant for carbonic acid, respectively (Cullison-Gray et al., 2011). This shows that processes changing the seawater carbonate chemistry will have opposite impacts on pH and pCO_2.

To understand how each process affects pH and pCO_2, it is easier to consider how the carbonate equilibrium constants, DIC and TA are affected. An increase in DIC or in the carbonate chemistry constants (K_1 and K_2) will result in an increase in pCO_2 and a decrease in pH. Most of the processes are illustrated with very similar pCO_2-pH curves (Cullison-Gray et al., 2011).

1. Temperature: An increase in temperature increases the carbonate equilibrium constants ($K_1$and K_2 defined as $-\log10(K_1)=-62.008+3670.7/T+9.7944\ln(T) -0.0118S+0.000116S^2$ and $-\log_{10}(K_2)=4.777+1394.7/T-0.0184S+0.000118S^2$ by (Mehrbach et al., 1973) as refitted by (Dickson and Millero, 1987)).
2. Gas exchanges: The absorption of atmospheric CO_2 by the oceans increases proportionally DIC but does not affect TA.
3. Soft tissue-pump: The photosynthetic uptake of CO_2 to form organic matter (biological production) can be expressed with the following equation (Sarmiento and Gruber, 2006):
   $106CO_2+16NO_3^-+HPO_4^{2-}+78H_2O+18H^+=C_{106}H_{175}O_{42}N_{16}P+150O_2$ **(5.1)**
   The nitrate uptake to form organic nitrogen results in an increase in TA. The formation of organic matter therefore not only decreases DIC but also increases TA proportionally to the ratio of carbon to nitrogen.
4. Carbonate pump: The biogenic formation of calcite and aragonite can be expressed with the following equation (Skirrow, 1975):
   $Ca^{2+}+CO_3^{2-}=CaCO_3$ **(5.2)**
   Calcification reduces DIC and TA with a ratio of 1:2.
5. Evaporation/precipitation: Dilution decreases DIC and TA but also the carbonate chemistry constants (K_1 and K_2). The addition of all these effects lead to a curve with smaller slope compared to the other curves (see Figure 5.7A).

Two areas have been identified (Figure 5.8) where pH and pCO_2 did not show a clear anti-correlation. The first area (in green on Figure 5.8) corresponds to the first two days of the D366 transect in the Strait of Moyle (northern part of region 1). The discrepancy between pH calculated from DIC and pCO_2 ($pH_{DICpCO2}$) and measured pH was between 0.02 and 0.05 pH units in this area. The reasons for this large discrepancy have not yet been identified. The second area (in blue on Figure 5.8) corresponds to the Skagerrak area (region 9), where salinity was lower than 30 due to outflow of low salinity waters from the Baltic Sea. Mixing of North Sea water with Baltic Sea water had an effect equivalent to a large dilution process as illustrated in green on Figure 5.7A.

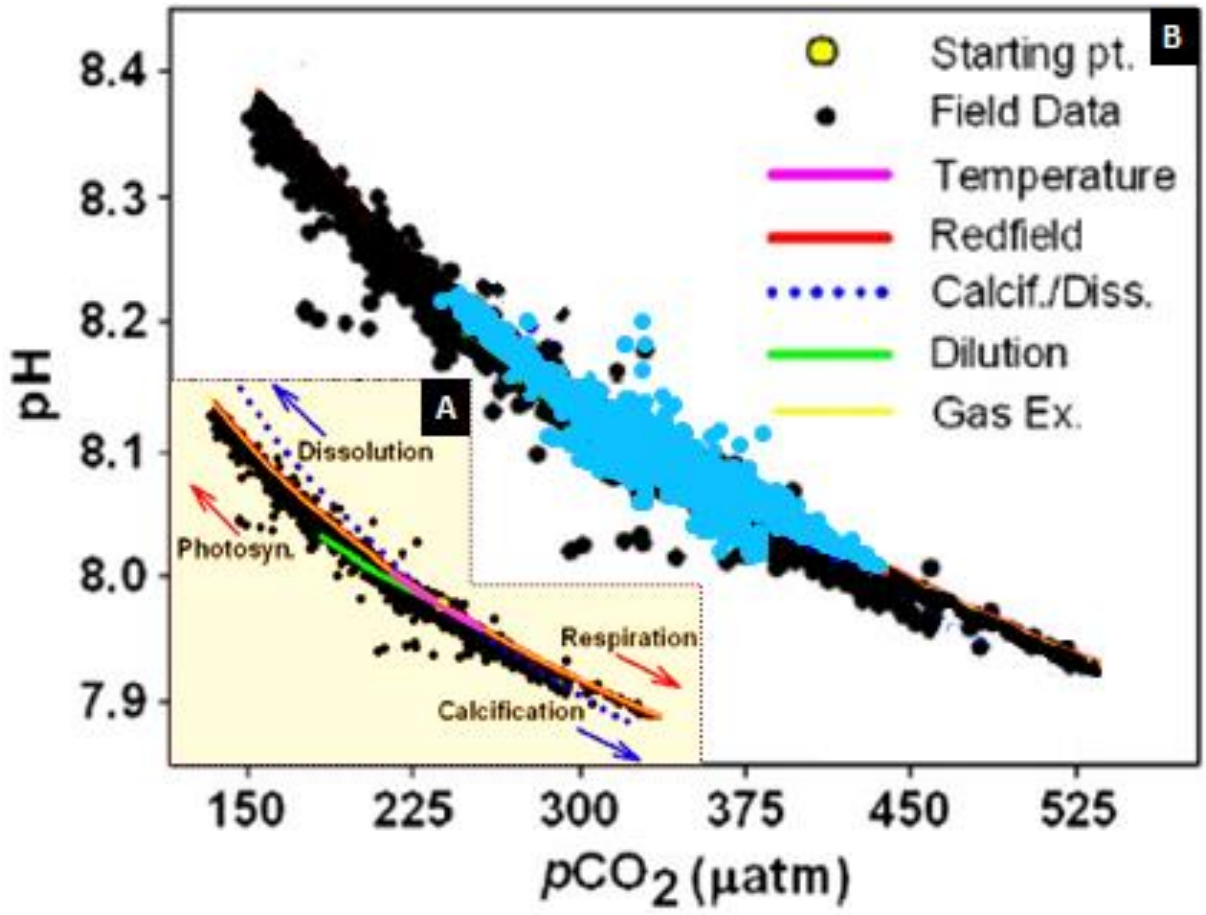

Figure 5.7: A. Impact of different modelled processes on the pH-pCO_2 relationship and B. pH versus pCO_2 data from the D366 research cruise (blue dots) plotted over data from (Cullison-Gray et al., 2011) collected in Monterey Bay on the MBARI M0 buoy in summer 2007 (black dots).

For biological production and respiration (red curve), DIC and AT were varied by the Redfield ratio 106:18 over the range AT=2243–2289 µmol kg^{-1} and DIC=1824–2094 µmol kg^{-1} (T=14.0 °C). Gas exchange (yellow curve) was calculated using a similar range for DIC, but keeping the AT constant (T=14.0 °C). For calcification and dissolution (blue filled circles), DIC and AT were varied by 1:2 over the range AT=2090–2770 µmol kg^{-1} and DIC=1950–2290 µmol kg^{-1} (T=14.0 °C). For changes in temperature (pink curve), DIC and AT were fixed at 2032 µmol kg^{-1} and 2254 µmol kg^{-1}, respectively, and temperature was varied over the range of the field data (11–16 °C). Dilution evaporation/precipitation green curve) was modelled by varying AT and DIC in a 1:1 ratio over the range AT=1985–2254 µmol kg^{-1} and DIC=1763–2032 µmol kg^{-1}. All calculations were centred on the initial conditions, S=33.7, DIC=2032 µmol kg^{-1} and AT=2254 µmol kg^{-1} (yellow filled circle). Figure adapted from (Cullison-Gray et al., 2011).

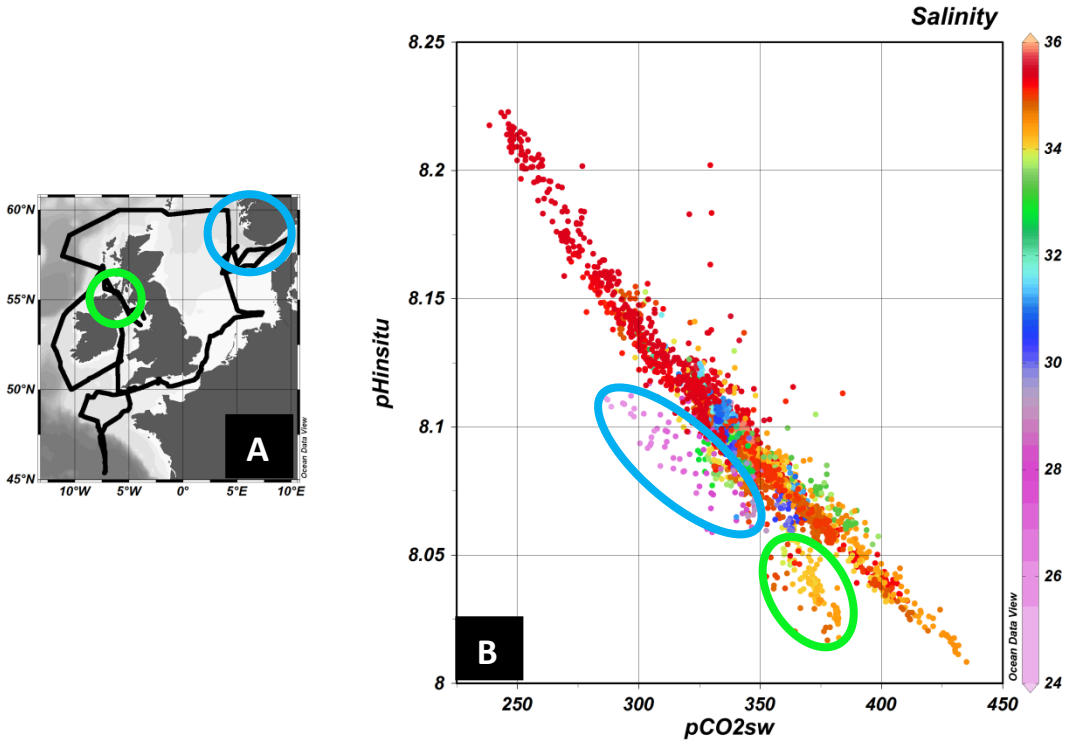

Figure 5.8: Two areas where pH and pCO_2 did not show an anti-correlation. **A.** Map of the ship track during the cruise D366 with indication of the two areas where pH and pCO_2 did not show a clear anti-correlation. **B.** pH versus pCO_2 data from the D366 research cruise with the salinity of the sample indicated in colour with indication of the two areas where pH and pCO_2 deviated from the anti-correlation curve.

5.3.3. Statistical results

5.3.3.1. Surface data from CTD station along the entire transect

The pH data appeared to be strongly correlated to dissolved oxygen for the surface samples from the CTD stations along the full transect (correlation coefficient Rho= 0.5987, p= 1.3815e-07, n=62). The stepwise multi-linear regression with DOC, O_2, S, T, Chl, SiO_4 and TON indicated that the correlation of O_2, T and S with pH was statistically significant and explained 72% of pH variance. O_2, T and S were found to explain 37%, 24% and 11%, respectively, of the variance in pH. The strong correlation with O_2 indicated that pH and O_2 were affected by similar processes and support the hypothesis that biological activity and remineralisation played a key role in the pH variations along the transect. The same stepwise multi-linear regression but without O_2 resulted in SiO_4 (18%), DOC (15%) and Chl (11%) explaining 44% of the pH distribution along the cruise transect.

5.3.3.2. Underway data divided into 11 regions

Results from the statistical analysis undertaken using the underway data are presented in Tables 5.2 and 5.3. The R^2 values express how much of the pH variance is explained by the regression. The component of the pH variance that can be attributed to each parameter is expressed in percentage. Results obtained with all the approaches show that the pH variability along the transect was mainly due to biological activity. In most of the regions, the various approaches resulted with the dominant parameters being related to the same processes. Results from the various approaches differ in the regions 6 to 8 where mixing with water from rivers and the Baltic Sea had a strong impact on the carbonate chemistry. Overall between 21 and 79 % of the pH variance can be explained using only salinity, temperature and chlorophyll. This was significantly improved when the nutrient parameters were added, resulting in 54 to 95 % of the pH variance being explained. The lowest percentages were obtained in regions where riverine inputs seem to impact the pH distribution (regions 3, 6 and 7). The low R^2 obtained in region 10 was due to the fact that the impact of primary production was not directly evidenced by correlation of chlorophyll concentration with pH (see discussion in chapter 5.3.4.2 Primary production).

Table 5.2: Results of the multi-linear regression analysis using S, T and Chl parameters with the underway data divided into 11 regions. The R^2 values express how much of the pH variance is explained by the regression.

Regions	R1	R2	R3	R5	R6	R7	R8	R9	R10
R^2	0.79	0.40	0.37	0.58	0.41	0.21	0.65	0.63	0.25
S	5.91	36.65	28.85	31.81	54.67	30.06	6.53	19.99	8.55
T	45.62	12.12	37.26	35.50	29.06	16.41	50.99	73.01	6.11
Chl	48.47	51.23	33.89	32.69	16.27	53.53	42.47	7.00	85.34
Intercept	8.080	8.107	8.112	8.111	8.078	8.080	8.094	8.111	8.161
S	0.002	-0.007	0.010	0.007	0.011	0.005	-0.001	0.005	0.002
T	0.014	0.002	0.013	0.008	-0.006	0.003	-0.011	-0.017	0.001
Chl	0.015	0.009	0.012	0.007	-0.003	0.010	0.009	0.002	0.018

Table 5.3: Results of the stepwise multi-linear regression analysis using S, T and Chl, SiO_4 and NO_x parameters with the underway data divided into 11 regions.
The R^2 values express how much of the pH variance is explained by the regression.

Regions	R1	R2	R3	R5	R6	R7	R8	R9	R10
R^2	0.94	0.94	0.54	0.61	0.81	0.61	0.78	0.74	0.79
S			40.26		72.82	33.33	13.83	17.15	14.22
T		30.24					42.82	68.49	
Chl	63.78	26.37		59.60		22.22			36.13
SiO4	36.22		59.74		27.18	19.29	43.34	14.36	
NO3		43.39		40.40		25.16			49.66
Intercept	8.083	8.083	8.111	8.111	8.072	8.086	8.096	8.109	8.163
S			0.009		0.016	0.033	0.004	0.005	-0.009
T		-0.017					-0.012	-0.019	
Chl	0.015	0.015		0.007		0.022			0.022
SiO4	-0.009		-0.013		-0.006	-0.019	0.012	0.004	
NO3		-0.025		-0.005		-0.025			-0.030

The impact of primary production on pH is highlighted by a positive correlation between pH and chlorophyll, and a negative correlation between nutrients and pH. The impact of temperature on pH is evidenced by a negative correlation between temperature and pH. The impact of freshwater inputs by rivers is evidenced by enhanced correlations between pH and salinity, but the sign of

the correlation will depend on the alkalinity (and DIC) levels in the river discharges. A positive correlation between pH and nutrients, and a negative correlation with dissolved organic matter can be additional indications of riverine inputs supplying high nutrient and DOC fluxes to coastal waters.

Biology is shown to be the dominant controlling process over pH in region 1, 2, 3, 5, 7 and 10. Temperature appears to be dominant in region 8 and 9, with still an important contribution by biology on pH in region 8. River inputs seem to have a strong impact on pH in region 6 and 7 as well as in region 3.

5.3.4. pH dynamics

5.3.4.1. Temperature

Temperature changes affect the carbonate equilibrium constants as evidenced in equations 5.1 and 5.2 (see section 5.3.2. Distribution and Quality of the carbonate data). A rise in temperature triggers a shift in the marine carbonate system resulting in a decrease in pH (Hunter, 1998) and CO_2 solubility (Zeebe and Wolf-Gladrow, 2001). The impact of temperature on the pH distribution is evidenced here in the Skagerrak area (region 9) (Figures 9A and B). In the deep trough along the Norwegian coast relatively warm waters of the Baltic Sea are discharged (evidenced by low salinity on Figure 5.9A). Temperature distributions explained about 50% of the pH variation in this region. Figure 5.9B shows the anti-correlation between temperature and pH: pH was observed to decrease as temperature increased when coming from the North Sea to the Skagerrak strait. In the English Channel (region 6), the stronger control of temperature on pH compared to primary production resulted in an anti-correlation between chlorophyll and pH (Table 5.1). The CO_2 uptake by primary production in this region was insufficient to balance the effect on pH of the increase in temperature. A localised area near Falmouth was a source of CO_2 to the atmosphere (Figure 5.9C), which was likely due to the shallow fully mixed and warm water column (evidenced by warm temperature (+2 °C) and low pH (-0.1 pH units) on Figure 5.9.D).

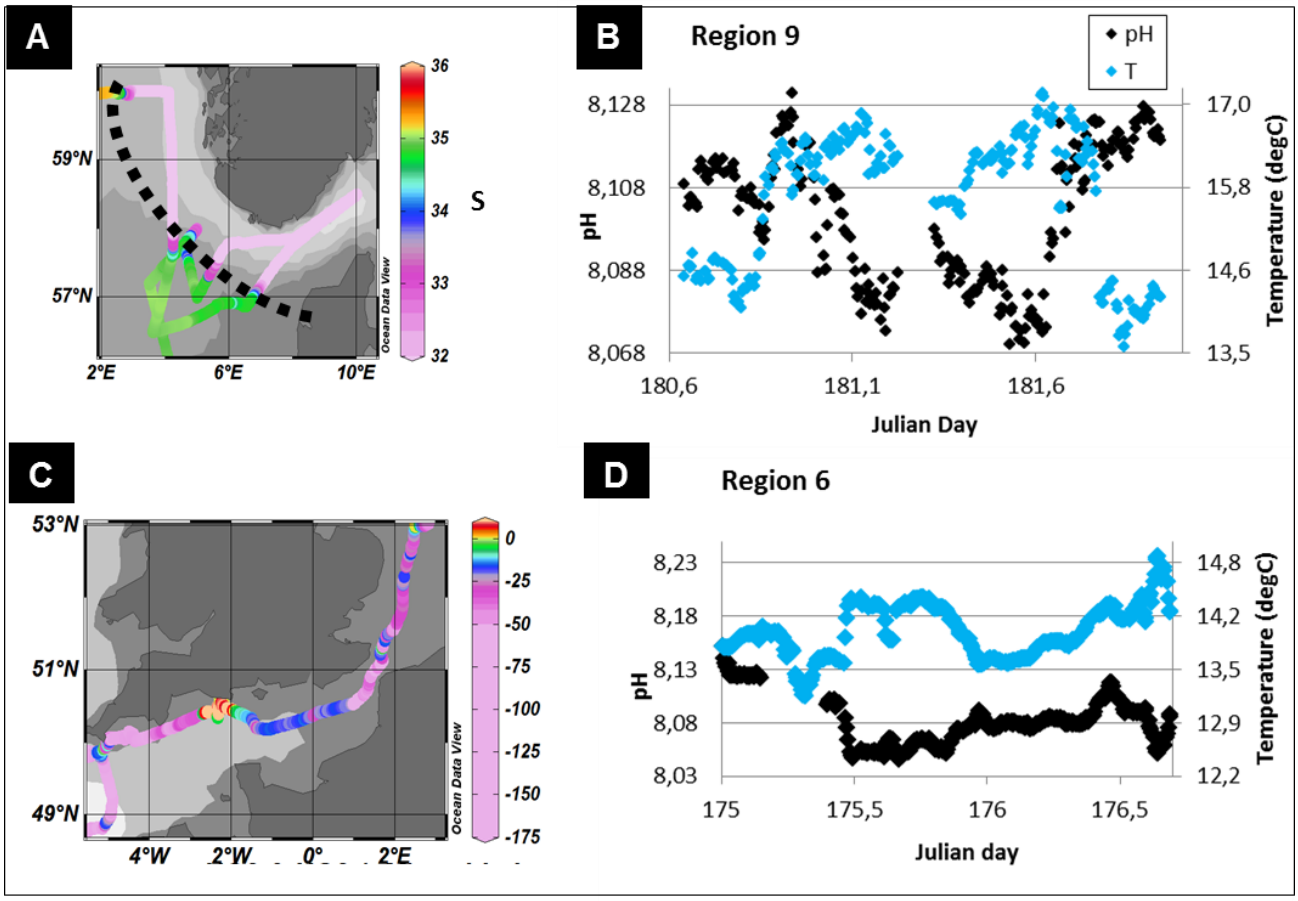

Figure 5.9: Impact of temperature on sea surface pH distribution. **A.** Map of sea surface salinity observed during the cruise D366 in the Skagerrak region (region 9). The dotted line shows the limit of region 9. **B.** Sea surface pH and temperature measured during D366 in the Skagerrak region. **C.** Map of the discrepancy between sea surface pCO_2 (pCO_{2sw}) and atmospheric pCO_2atm measured during the cruise D366 in the English Channel (region 6). **D.** Sea surface pH and temperature measured during the cruise D366 in the English Channel.

5.3.4.2. Primary production

The impact of primary production on the pH distribution is evidenced by the positive correlation between chlorophyll and pH as seen in the section of the North Atlantic Ocean west of Ireland (region 2) (Figure 5.10). However, pH is not necessarily directly correlated to the chlorophyll concentration as the stage of the phytoplankton bloom, grazing and remineralisation will strongly affect the carbonate chemistry in the bloom. For example, Watson and co-workers proposed three different linear relationships between pCO_2 and chlorophyll corresponding to the different stages of development of the phytoplankton bloom (Watson et al., 1991): the "recent history bloom" (pCO_2=358-16.8*[Chla], r^2=0.624, p<0.0001), the "peak stage" of the bloom (pCO_2=332-10.6*[Chla], r^2=0.372, p<0.0001) and the "late stage" of the bloom (pCO_2=299-6.6*[Chla], r^2=0.490, p<0.0001). This is due to the fact that carbonate chemistry changes due to

phytoplankton blooms occur at a shorter timescale than air-sea CO_2 exchanges. Furthermore, the impact of primary production is better highlighted by the anti-correlation of pH with nutrients, in particular nitrate. The northernmost part of the transect (region 10), where the highest levels of pH and chlorophyll were observed, provided a good example of this correlation. The multi-linear regression with S, T and chlorophyll highlighted the strong correlation of chlorophyll with pH over S and T but the regression was able to describe only 21% of the pH variance (Table 5.1). The addition of nitrate in the regression enabled to describe 79% of the pH variance in the region (Table 5.2). The positive correlation between pH and temperature in regions 1, 2, 3, 5, 7 and 10 provided another indication that primary production was the dominant parameter controlling the pH distribution in these regions, and not temperature. The positive correlation can be related to the fact that an increase in temperature favours primary production ($\mu=a*b^T$ with μ specific growth rate, a and b constants, (Eppley, 1972)), which has an opposite effect on pH than the temperature rise.

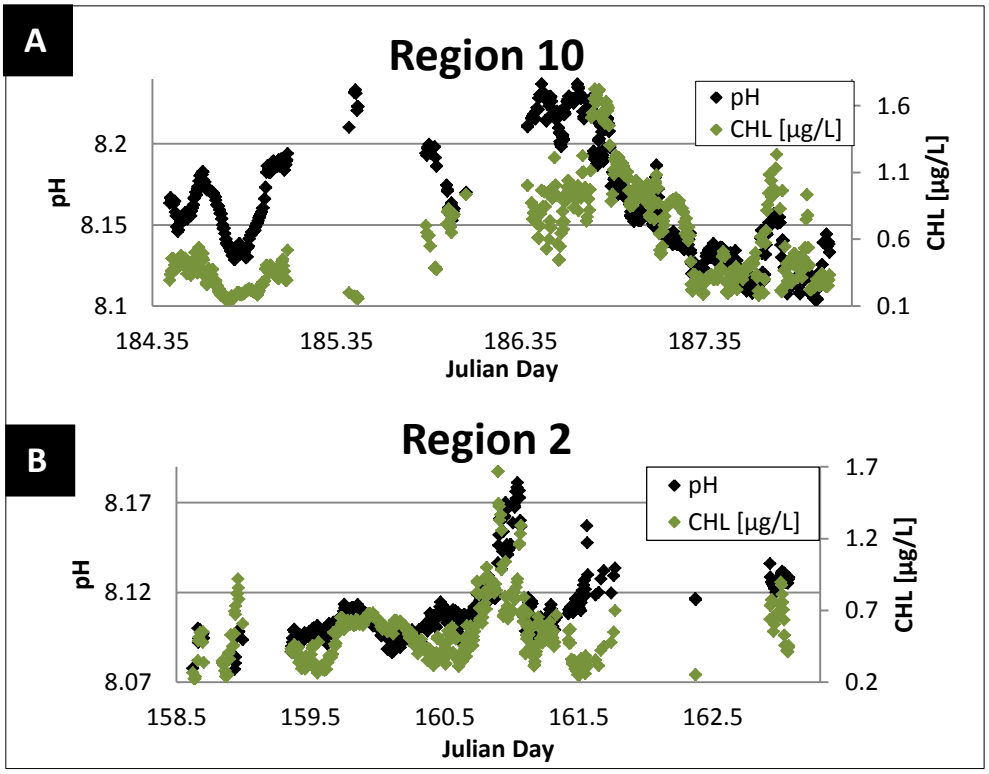

Figure 5.10: Sea surface pH and chlorophyll concentration measured during the cruise D366 in **A.** the part of North Atlantic Ocean west of Ireland (region 2) **B**. and the Skagerrak region (region 10).

5.3.4.3. Organic and inorganic river inputs: remineralisation

Rivers inputs potentially have two opposite effects on the carbonate chemistry: the addition of nutrients enhances the primary production (increase in pH) whereas the addition of organic carbon may result in a decrease in pH through remineralisation processes. However, in our observations we only note the resulting balance of the two processes. DOC distribution could explain 15% of the pH variance along the full transect. In two areas, the strait of Moyle in the Irish Sea (northern part of region 1) and Southern North Sea (region 7), the primary production was not sufficiently high to balance the remineralisation processes. Primary production in the Southern North Sea was limited by low light levels as a consequence of the fully mixed water column and the high water turbidity of the area (Simpson and Sharples, 2012). Enhanced levels of remineralisation were likely due to the observed high concentrations of dissolved organic matter (DOC, DON and DOP) and low concentrations of particulate organic matter (POC, PON and POP) (data from Ting Ting Shi) in this region. The lower salinity (and lower TA) observed in these two regions compared to surrounding regions, supports the hypothesis that the organic matter was derived from riverine inputs. Low TA resulted in lower buffering capacity and would explain that these two regions were sources of CO_2 to the atmosphere.

5.3.4.4. Mixing

Tidal and wind-driven currents are important in the Northwest European Shelf waters (Huthnance, 1997). These currents can lead to intense mixing of the water column such as tidal upwelling which brings bottom water to the surface (Simpson and Sharples, 2012). These deeper waters are typically more acidic, enriched in DIC and nutrients than the surface water due to remineralisation of the organic matter. Acidic waters brought to the surface by shelf mixing processes have been observed in two regions during the cruise. The first region was to the south of Cornwall (UK) (region 4), where the water column has probably been mixed either by strong tidal mixing (Simpson and Sharples, 2012) or storm activity. The mixing of the water column is evidenced on Figure 5.10B, where the temperature gradients show a typical stratified water column temperature profile on the 15/06/2011 (red) and a more homogenised temperature profile on the 30/06/2011 (green). This mixing resulted in more acidic surface water compared to a week prior as well as higher levels of DIC (+36 µmol/kg) and TON (+2 µM) (Figure 5.11C and D). The second region was south of the Shetland Islands (region 11) where deep water was brought to surface partly by the advection of Atlantic water through the Orkney-Shetland passage but also by intense tidal mixing around the Orkney and Shetland Isles area (Turrell, 1992) (Figure 5.12). Indeed, tidal currents are intensified in the area where the flow is constrained by topography (Pingree et al., 1978). This upwelled water was evidenced by colder temperature (-2 °C) and

enhanced DIC (+40 µmol/kg) and TON (+4 µM) concentrations compared with surrounding waters. Higher nutrient concentrations resulted in enhanced primary production but this was not sufficiently pronounced to balance the acidity of the upwelled water.

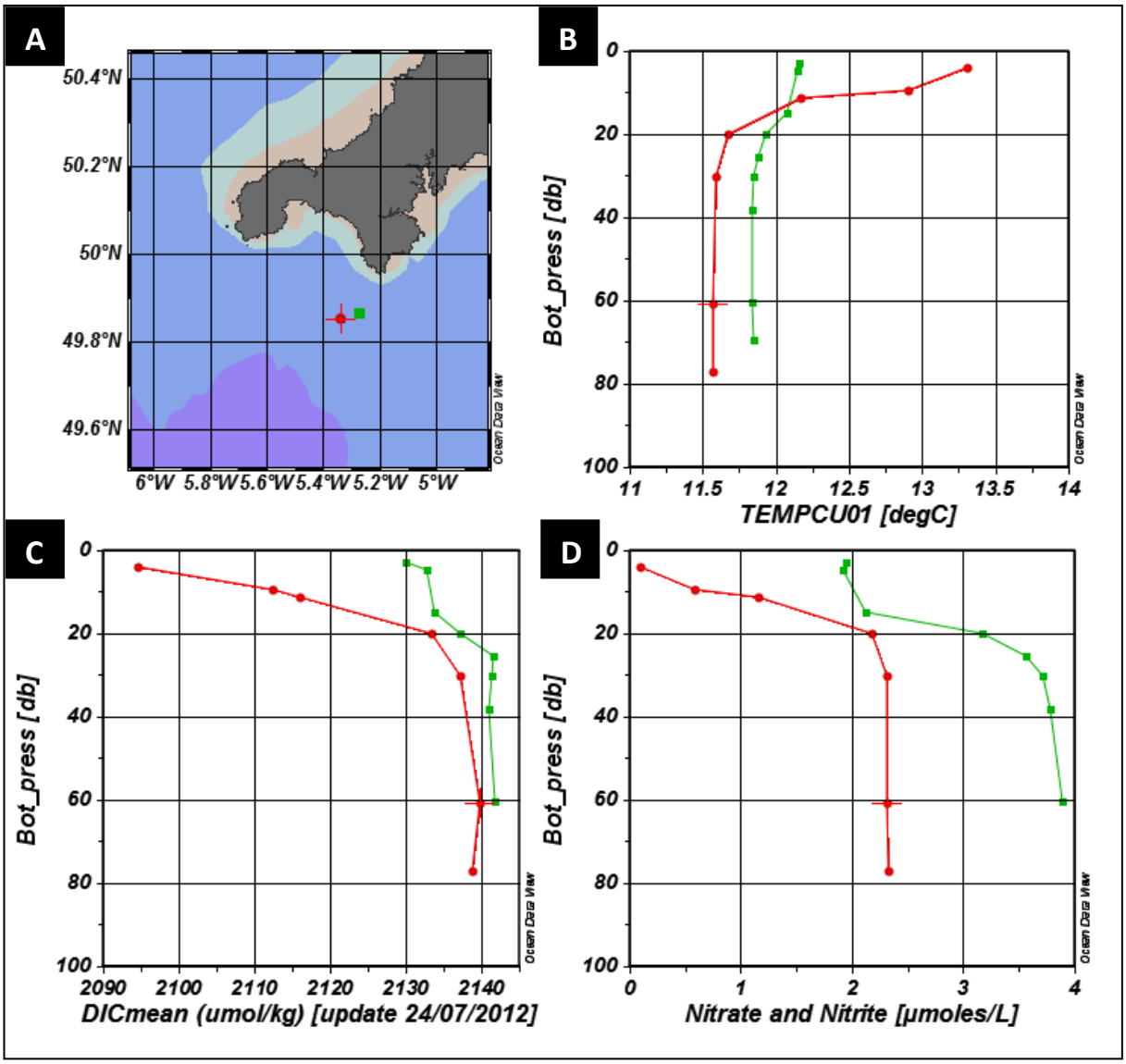

Figure 5.11: Impact of storm mixing on sea surface pH.

A. Location of station 20 sampled on the 15/06/2011 (red) and station 30 sampled on the 30/06/2011 (green) south of Cornwall (UK). **B. C and D.** Depth profiles of temperature, DIC and nitrate and nitrite at the two stations.

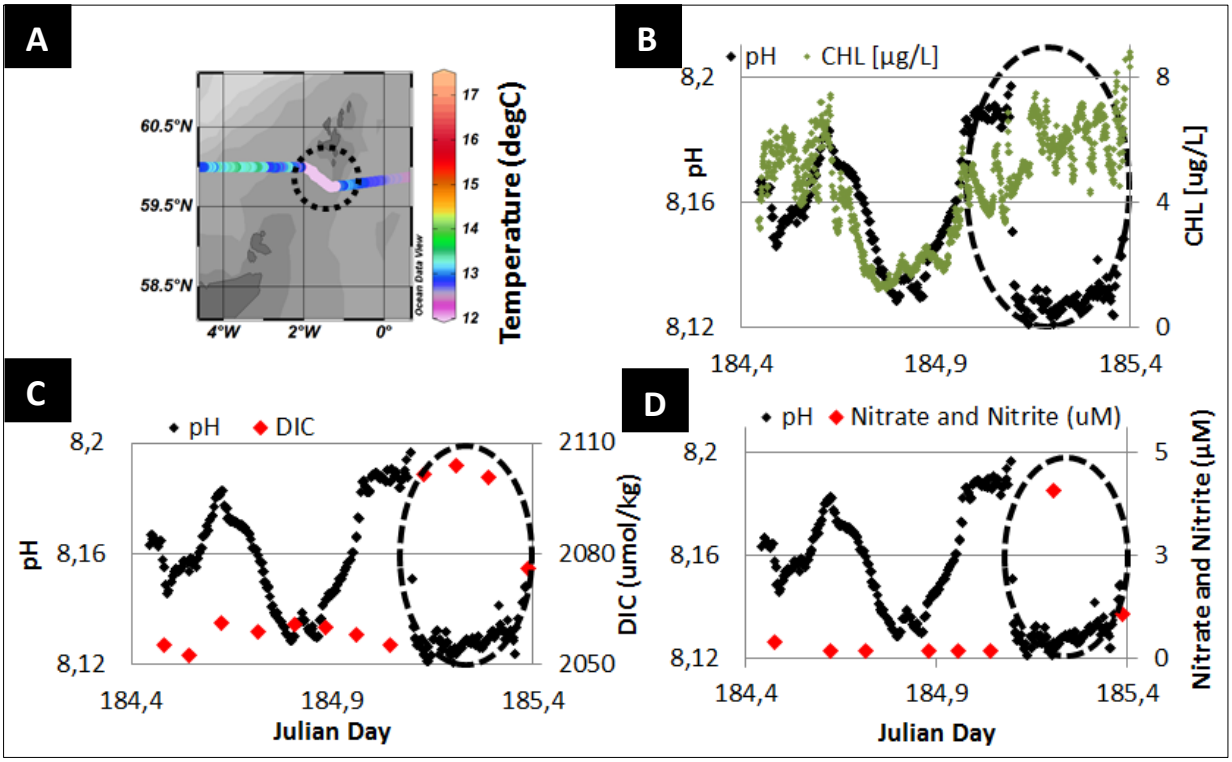

Figure 5.12: Impact of tide shelf mixing on sea surface pH.

A. Map of sea surface temperature measured during the cruise D366 south of the Orkney Islands. Sea surface pH and **B.** chlorophyll, **C.** DIC and **D.** Nitrate and nitrite concentrations.

5.4. Conclusion

We have presented a new set of surface seawater pH data determined in the Northwest European Shelf Seas in summer 2011. As a result of the high spatial and temporal resolution of the pH data along with temperature, salinity, chlorophyll and nutrients, we have been able to unravel the main processes controlling the carbonate chemistry dynamics of the shelf sea surface water. Despite the difficulties presented by this type of dataset, the statistical approach undertaken allowed us to determine the main correlations between pH and other parameters, and from these correlations we inferred the main processes involved. Unsurprisingly for this time of year, the biological activity appeared to be the main control of the pH distribution along the cruise transect. 44% of the pH distribution along the cruise transect could be explained by SiO_4 (18%), DOC (15%) and Chl (11%). The impact of primary production on pH was well evidenced by the strong anti-correlation between nutrients and pH in region 10 where the highest levels of chlorophyll and pH were observed. However, it has been shown that in some regions temperature and riverine inputs balanced or even overcame the impact of primary production. In the Skagerrak region for example, temperature distribution could explain about 50% of the pH variation. Riverine inputs were evidenced by high dissolved organic matter levels in the Strait of

Moyle and the southern North Sea leading to important remineralisation processes and low pH. DOC distribution could explain 15% of the pH variance along the full transect. Finally, the effect of upwelled water due to shelf mixing, on surface seawater pH, has also been observed in two well defined regions where pH and temperature levels were lower than in the surroundings waters whereas DIC and nutrients levels were higher. This study highlights the high variability of the *in situ* conditions in coastal shelf waters where several processes impact simultaneously the carbonate chemistry. Only dataset with high spatial and temporal coverage will enable to make more accurate estimate of the air-sea CO_2 fluxes in coastal regions. In order to quantify the main controls on carbonate chemistry, the same transect should be sampled at different seasons similarly to the work presented by Thomas and co-workers (Thomas et al., 2005).

References

Badr, E. S. A., E. P. Achterberg, A. D. Tappin, S. J. Hill, and C. B. Braungardt (2003), Determination of dissolved organic nitrogen in natural waters using high-temperature catalytic oxidation, *TrAC Trends in Analytical Chemistry*, *22*(11), 819-827.

Borges, A. V., and N. Gypens (2010), Carbonate chemistry in the coastal zone responds more strongly to eutrophication than to ocean acidification, *Limnology and Oceanography*, *55*(1), 346-353.

Borges, A. V., B. Delille, and M. Frankignoulle (2005), Budgeting sinks and sources of CO2 in the coastal ocean: Diversity of ecosystems counts, *Geophys. Res. Lett.*, *32*(14), L14601.

Canadell, J. G., C. Le Quéré, M. R. Raupach, C. B. Field, E. T. Buitenhuis, P. Ciais, T. J. Conway, N. P. Gillett, R. Houghton, and G. Marland (2007), Contributions to accelerating atmospheric CO2 growth from economic activity, carbon intensity, and efficiency of natural sinks, *Proceedings of the National Academy of Sciences*, *104*(47), 18866-18870.

Carritt, D. E., and J. Carpenter (1966), Comparison and evaluation of currently employed modifications of the Winkler method for determining dissolved oxygen in seawater; a NASCO report, *J. mar. Res*, *24*(3), 286-318.

Chen, C.-T. A., and A. V. Borges (2009), Reconciling opposing views on carbon cycling in the coastal ocean: Continental shelves as sinks and near-shore ecosystems as sources of atmospheric CO2, *Deep Sea Research Part II: Topical Studies in Oceanography*, *56*(8–10), 578-590.

Clayton, T., and R. Byrne (1993), Spectrophotometric seawater pH measurements: total hydrogen ion concentration scale calibration of m-cresol purple and at-sea results, *Deep-sea research. Part 1. Oceanographic research papers*, *40*(10), 2115-2129.

Cullison-Gray, S. E., M. D. DeGrandpre, T. S. Moore, T. R. Martz, G. E. Friederich, and K. S. Johnson (2011), Applications of in situ pH measurements for inorganic carbon calculations, *Marine Chemistry*.

Dickson, A., and F. Millero (1987), A comparison of the equilibrium constants for the dissociation of carbonic acid in seawater media, *Deep Sea Research Part A. Oceanographic Research Papers*, *34*(10), 1733-1743.

Doney, S. C., N. Mahowald, I. Lima, R. A. Feely, F. T. Mackenzie, J.-F. Lamarque, and P. J. Rasch (2007), Impact of anthropogenic atmospheric nitrogen and sulfur deposition on ocean acidification and the inorganic carbon system, *Proceedings of the National Academy of Sciences*, *104*(37), 14580-14585.

Eppley, R. W. (1972), Temperature and phytoplankton growth in the sea, *Fish. Bull*, *70*(4), 1063-1085.

Feely, R. A., C. L. Sabine, J. M. Hernandez-Ayon, D. Ianson, and B. Hales (2008), Evidence for Upwelling of Corrosive" Acidified" Water onto the Continental Shelf, *Science*, *320*(5882), 1490.

Frankignoulle, M., G. Abril, A. Borges, I. Bourge, C. Canon, B. Delille, E. Libert, and J.-M. Théate (1998), Carbon dioxide emission from European estuaries, *Science*, *282*(5388), 434-436.

Gypens, N., G. Lacroix, C. Lancelot, and A. V. Borges (2011), Seasonal and inter-annual variability of air-sea CO2 fluxes and seawater carbonate chemistry in the Southern North Sea, *Progress in Oceanography*, *88*(1-4), 59-77.

Hardman-Mountford, N. J., G. Moore, D. C. E. Bakker, A. J. Watson, U. Schuster, R. Barciela, A. Hines, G. Moncoiffé, J. Brown, and S. Dye (2008), An operational monitoring system to provide indicators of CO2-related variables in the ocean, *ICES Journal of Marine Science: Journal du Conseil*, *65*(8), 1498-1503.

Hunter, K. A. (1998), The temperature dependence of pH in surface seawater, *Deep Sea Research Part I: Oceanographic Research Papers*, *45*(11), 1919-1930.

Huthnance, J. M. (1997), North Sea interaction with the North Atlantic ocean, *Ocean Dynamics*, *49*(2), 153-162.

Johnson, K., J. Sieburth, P. Williams, and L. Brändström (1987), Coulometric total carbon dioxide analysis for marine studies: automation and calibration, *Marine Chemistry*, *21*(2), 117-133.

Kirkwood, D. (1989), Simultaneous determination of selected nutrients in sea water, *International Council for the Exploration of the Sea (ICES) CM*, *100*, 29.

Kitidis, V., et al. (2012), Seasonal dynamics of the carbonate system in the Western English Channel, *Continental Shelf Research*, *42*(0), 30-40.

Mehrbach, C., C. H. Culberson, J. E. Hawley, and R. M. Pytkowicz (1973), Measurement of the apparent dissociation constants of carbonic acid in seawater at atmospheric pressure, *Limnology and Oceanography*, 897-907.

Mintrop, L. (2004), Versatile Instrument for the Determination of Titration Alkalinity. Manual for versions 3S and 3C. Version 2.0. MARine ANalytics and DAta (MARIANDA), Kiel, Germany, 45 pp.

OSPAR Commission, L. (2000), Quality Status Report 2000, Region II Greater North Sea.

Pingree, R., P. Holligan, and G. Mardell (1978), The effects of vertical stability on phytoplankton distributions in the summer on the northwest European Shelf, *Deep Sea Research*, *25*(11), 1011-1028.

Rérolle, V. M. C., C. F. A. Floquet, M. C. Mowlem, D. P. Connelly, E. P. Achterberg, and R. R. G. J. Bellerby (2012), Seawater-pH measurements for ocean-acidification observations, *TrAC Trends in Analytical Chemistry*, *40*(0), 146-157.

Rérolle, V., Floquet, C. F., Harris, A. J., Mowlem, M. C., Bellerby, R. R., and Achterberg, E. P.: Development of a colorimetric microfluidic pH sensor for autonomous seawater measurements, Analytica Chimica Acta, In Press, 2013.

Ribas Ribas, M. (2012), D366 Underway Carbonate Chemistry Data, *D366 UW Carbonate Chemistry Data REPORT*.

Sarmiento, J. L., and N. Gruber (2006), *Ocean biogeochemical dynamics*, Princeton University Press.

Simpson, H. J., and J. Sharples (Eds.) (2012), *Introduction to the physical and biological oceanography of shelf seas*, 424 pp., Cambridge: Cambridge University Press.

Skirrow, G. (1975), The dissolved gases-carbon dioxide, *Chemical oceanography*, *2*, 1-192.

Thomas, H., and A. V. Borges (2012), Biogeochemistry of coastal seas and continental shelves – Including biogeochemistry during the International Polar Year, *Estuarine, Coastal and Shelf Science*, *100*(0), 1-2.

Thomas, H., Y. Bozec, K. Elkalay, and H. J. W. de Baar (2004), Enhanced open ocean storage of CO2 from shelf sea pumping, *Science*, *304*(5673), 1005-1008.

Thomas, H., Y. Bozec, H. J. W. de Baar, K. Elkalay, M. Frankignoulle, L. S. Schiettecatte, G. Kattner, and A. V. Borges (2005), The carbon budget of the North Sea, *Biogeosciences*, *2*(1), 87-96.

Turrell, W. (1992), New hypotheses concerning the circulation of the northern North Sea and its relation to North Sea fish stock recruitment, *ICES Journal of Marine Science: Journal du Conseil*, *49*(1), 107-123.

Volk, T., and M. Hoffert (1985), Ocean carbon pumps-Analysis of relative strengths and efficiencies in ocean-driven atmospheric CO2 changes, *Cambridge Contemporary Astrophysics*, 99-110.

Watson, A. J., C. Robinson, J. Robinson, P. J. B. Williams, and M. Fasham (1991), Spatial variability in the sink for atmospheric carbon dioxide in the North Atlantic.

Zeebe, R. E., and D. A. Wolf-Gladrow (2001), *CO2 in seawater: equilibrium, kinetics, isotopes*, Elsevier Science.

Zhang, H., and R. H. Byrne (1996), Spectrophotometric pH measurements of surface seawater at in-situ conditions: absorbance and protonation behavior of thymol blue, *Marine Chemistry*, *52*(1), 17-25.

Chapter 6: Conclusion and Future work

An automated underway pH system has been developed and successfully deployed on several cruises. The system was stable for a period of two months at sea. The level of precision (0.001 pH units) and accuracy (within 0.004 pH units) achieved were adequate for the study of the marine carbonate system and ocean acidification. The system specifications are summarised in Table 6.1.

Table 6.1: Specifications of the pH system.

	1. Continuous Underway System	2. Discrete Samples System
Pumps	2 syringe pumps Harvard	2 Solenoid Pumps Takasago
Valves	4 Lee valves	1 Lee Valve
Light	3λ LEDs	3λ LEDs
Detector	Ocean Optics HR4000 USB Spectrometer	Ocean Optics HR4000 USB Spectrometer
Temperature	+0.2 degC In situ in Sampling Chamber	Fixed controlled Temperature in bath or in Temperature Chamber connected to bath
Indicator	Thymol Blue	meta-Cresol Purple
Conditions tested	-2<T(°C)<25 26<S<36 Tested at sea	T=25°C S=35 Tested at sea
Frequency	10 measurements/hr	17 measurements/hr
Precision	0.001	0.001
Accuracy	<0.004	mCP not characterised

The first step of miniaturisation, the design and fabrication of a microfluidic PMMA chip, allowed the use of very small volumes of sample (550 uL) and indicator (12 uL) for an individual analysis. The single packaged three wavelength LED light source used for the chip was small, cheap, stable and had a relatively narrow spectrum. The use of a three wavelength LED with detection that integrates over the full width of each LED spectra indicated that low wavelength resolution detectors can be used instead of the current USB mini spectrophotometer. This was further demonstrated with measurements performed with a single photodiode and alternate flashing (time domain multiplexing) of the three wavelengths LED. Although the precision obtained was not yet sufficient for ocean acidification studies (≤0.002 pH units), the experiment showed the feasibility of such measurements. Finally, the pH measurement close to in situ temperature (+0.2 °C) in a sampling chamber not only reduced the source of error associated with the pH correction to in situ conditions, but also avoided the need for a heater. Data collected with this system on the D366 UKOA cruise were used to study the pH dynamics on the Northwest European Shelf. The quality of the data proved to be adequate for ocean acidification studies. The high spatial resolution allowed us to unravel the key processes controlling the pH distribution along the cruise transect. Primary production was found to be the main control of the pH distribution in the study region. However, the effects of temperature, rivers and acidic upwelled water were also observed to counteract the effect of primary production in parts of the study region.

Further technical improvements are still to be made to obtain a reliable in situ instrument. Below are some suggestions to improve the pH system.

6.1. Fluidics

The following part contains suggestions concerning the future design of the PMMA chip.

6.1.1. Design of the static mixer

A practical approach was chosen to design the static mixer. The aim was to obtain a homogeneous mixing on the cross-section of the cell as well as an enhanced dispersion along the length of the cell. The design of the serpentine can be improved in order to obtain similar mixing to the mixing obtained with the current design but with lower sample and indicator volumes and more importantly a faster mixing process. Increasing the measurement frequency will be important for deployment of the system on *in situ* platforms such as floats or gliders. The software COMSOL Multiphysics will form a great tool to improve the design of the microfluidic cell. The software uses the finite element method to simulate multi-physics processes for various engineering applications. The last version of the software has two specifics modules which are very useful for this design: the Microfluidic Module and Chemical Species Transport. These modules would allow the modeling of the mixing and dispersion of the indicator in the sample whilst flowing through the cell.

6.1.2. Thermistors in the flow cell

In the current system temperature is measured inside the sampling chamber very close to the absorption cell. We assume that the temperature inside the absorption cell is the same as the temperature outside of the cell. This is probably correct most of the time but not when temperature changes abruptly. It would therefore be more accurate to measure the temperature inside the flow cell. This can be achieved by inserting the thermistors in the channel, just after the absorption cell to avoid measurement disturbances. This will require only a small modification of the PMMA chip design.

6.1.3. Implementation of the group pump

To allow *in situ* deployment of the microfluidic pH system, it will be necessary to implement a syringe pump as developed by the Sensors group (NOC, Southampton). The main issue with the pump developed by the Sensors group is that the 2 plungers of this pump (the one for the sample, and the one for the indicator) are activated simultaneously and cannot be decoupled; whereas on the pH system only one pump is injecting at a time. The following sections describe two potential solutions to this issue.

6.1.3.1. Valves addition and flow diversion

The first approach would necessitate a minimum design alteration. The idea is to implement additional valves on the chip in order to divert the flow when it should not be injected into the flow cell. For the sample, the valve could divert the sample flow directly to waste; whereas for the indicator, the valve could send the indicator back to its storage compartment and avoid wasting it.

6.1.3.2. Change the measurement strategy

The second approach would require a revision of the entire measurement strategy. The idea would be to achieve a higher mixing ratio and use a 10 cm absorption cell. Dispersion would not be important anymore; a high mixing ratio could be achieved with the current 1:10 pump by diluting the indicator in one of the syringes. This would be done by withdrawing indicator as well as some sample in the syringe normally dedicated to the indicator only. Alternating indicator and sample when withdrawing the plunger will allow user defined dilution. This may also allow mixing but this will need development / investigation. Finally the diluted indicator will be mixed with further sample at 1:10 ratio (as currently done with the pump employed by the Sensor group) when injecting it to the cell simultaneously with the sample in the second syringe.

6.2. Optics

A key component that is not suitable for in situ deployment in the optical set up is the Ocean Optics USB mini spectrophotometer. This spectrophotometer could be replaced by a solid state spectrophotometer (Hamamatsu C10988MA-01) or a single photodiode (PD).

6.2.1. Hamamatsu mini spectrometer

The spectrophotometer (C10988MA-01) measures only (27.6 x 13 x 16.8 mm) and can be easily integrated into an electronic board. The spectral resolution of the instrument is 14 nm but the integration of the whole LED peak signal (FWHM 15-30 nm) showed that the wavelength resolution was not an issue when using these LEDs (see section 4.2.4.1. Deviation due to the polychromatic light source). This detector also appears to be more stable than the Ocean Optics USB spectrophotometer: a test in the laboratory allowed us to obtain a pH precision of 0.0005 pH units, n = 3). The influence of temperature on the detector sensitivity needs to be quantified.

6.2.2. PhotoDiode

The use of a single photodiode with flashing LEDs was proven feasible (see section 4.4. Replacement of the spectrometer with a photodiode). Better quality electronics and a mechanically stable set up avoiding any movements of the optical fibres would improve the set-up with a single photodiode.

6.3. Inter-calibration (Bergen, Seattle)

The quality of the pH system measurements have been checked using various approaches: measurements of certified Tris buffer, measurement of certified seawater for DIC and TA, comparison of measured pH against calculated pH from pCO_2, DIC and TA during the UKOA cruise. All showed that our measurements were of high quality.

An inter-comparison experiment with other pH systems could be very informative. Richard Bellerby and Emmanuelle Roberto-Regianni have developed a colorimetric pH system in Bergen (Bellerby et al., 2002). The NOAA PMEL group in Seattle uses a SAMi-pH system and likely the new Honeywell ISFET system (Martz et al., 2010) as well. A side-by-side comparison exercise would reinforce the credibility of these systems for ocean acidification studies.

References

Bellerby, R. G. J., A. Olsen, T. Johannessen, and P. Croot (2002), A high precision spectrophotometric method for on-line shipboard seawater pH measurements: The automated marine pH sensor (AMpS), *Talanta*, *56*(1), 61-69.

Martz, T. R., J. G. Connery, and K. S. Johnson (2010), Testing the Honeywell DurafetŽ for seawater pH applications, *Limnol. Oceanogr. Methods*, *8*, 172-184.

Appendix

Appendix 1: Electronics

A1a. Valves driver circuit

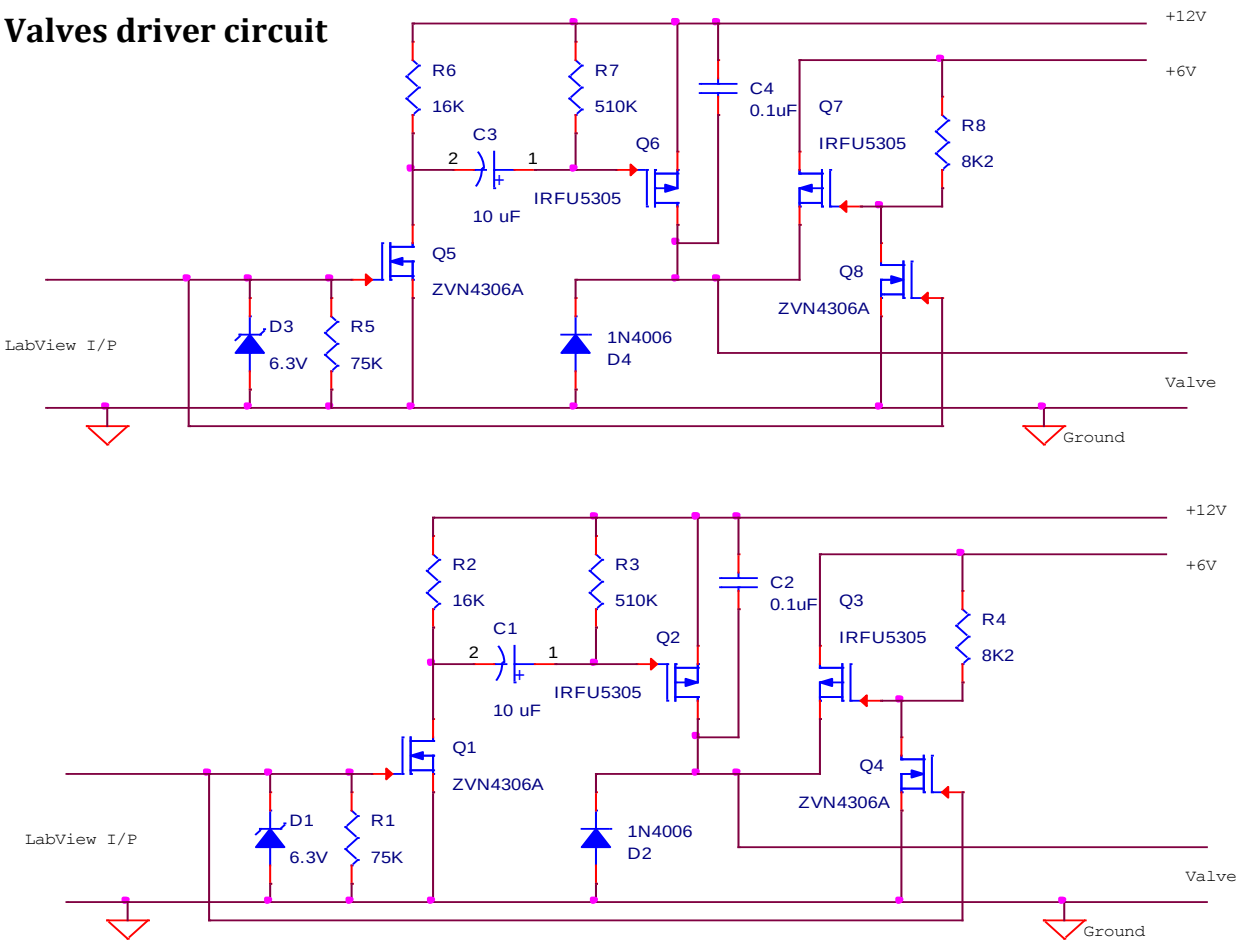

Title <Title>		
Size A	Document Number <Doc>	Rev <Rev Code>
Date: Monday, May 09, 2011	Sheet 1 of 1	

A1b. Thermistors driver circuit

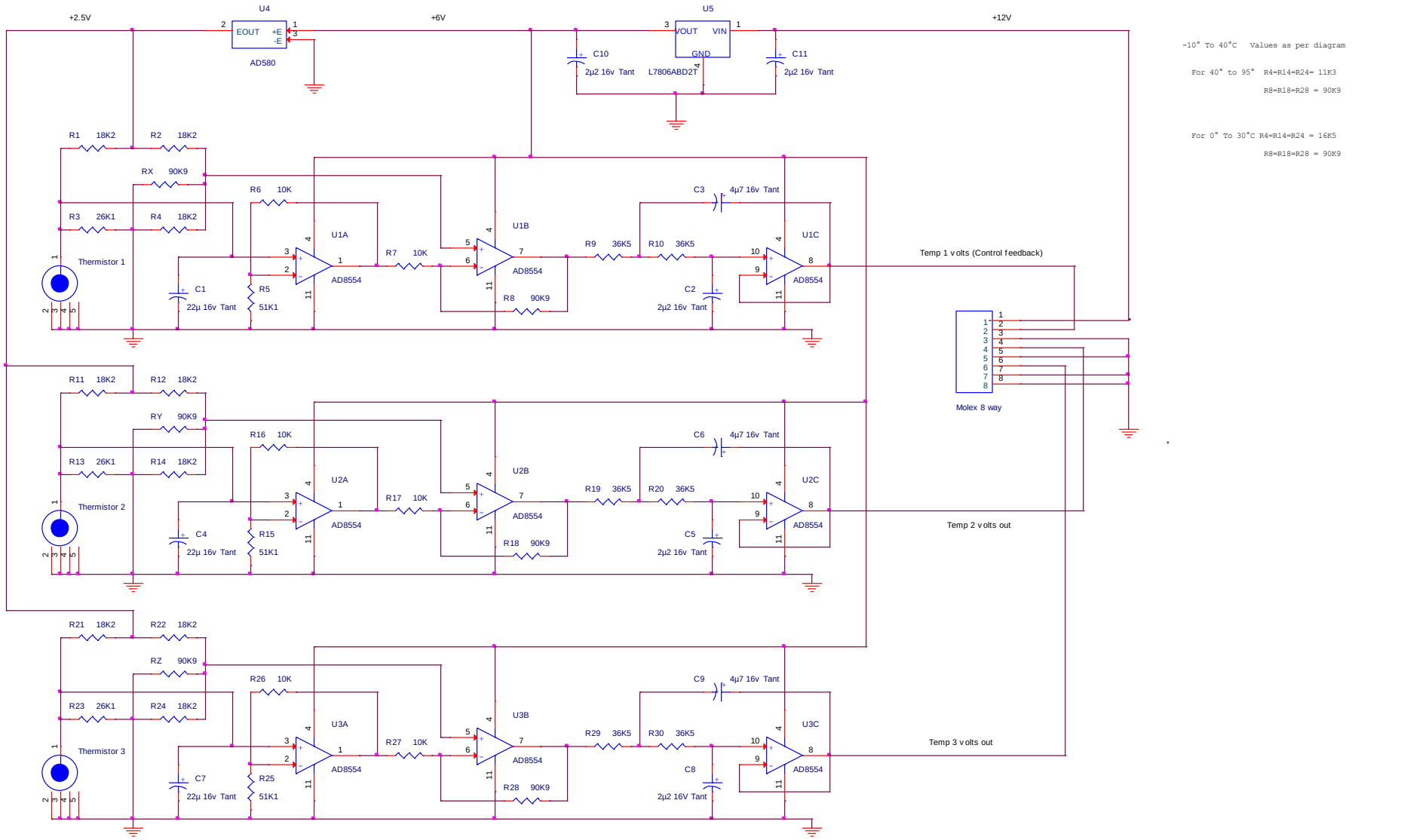

Title	Thermistor Temperature Probe		
Size A3	Document Number # 47	Andy Harris USL	Rev
Date: Wednesday, June 01, 2011	Sheet 1 of 1		

A1c. LED constant current driver circuit

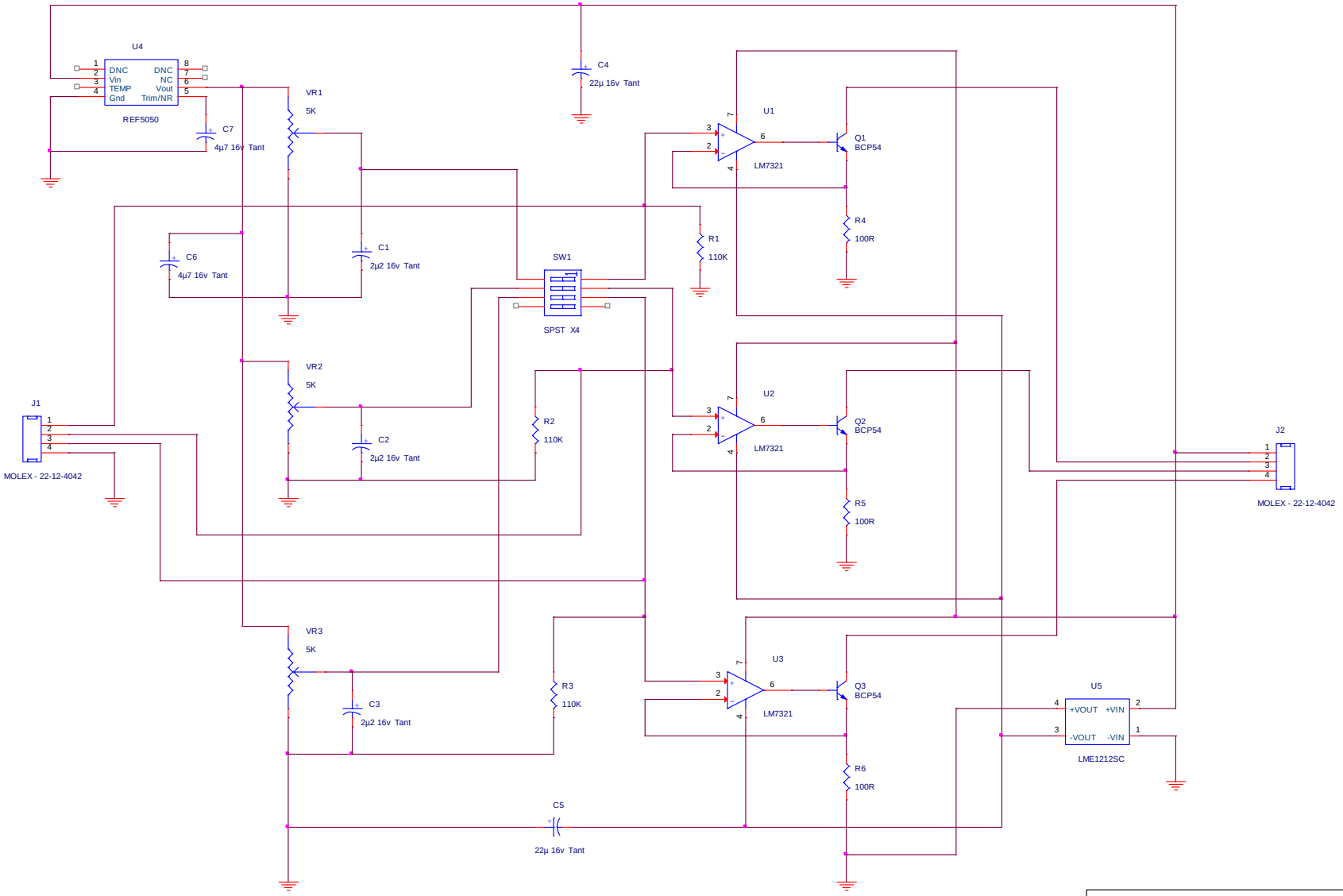

Title	LED Constant Current Driver	
Size A3	Document Number #48 Andy Harris USL	Rev
Date: Wednesday, November 17, 2010	Sheet 1 of 1	

Appendix 2: CAD Drawings

A2a. Underway Sampling Chamber

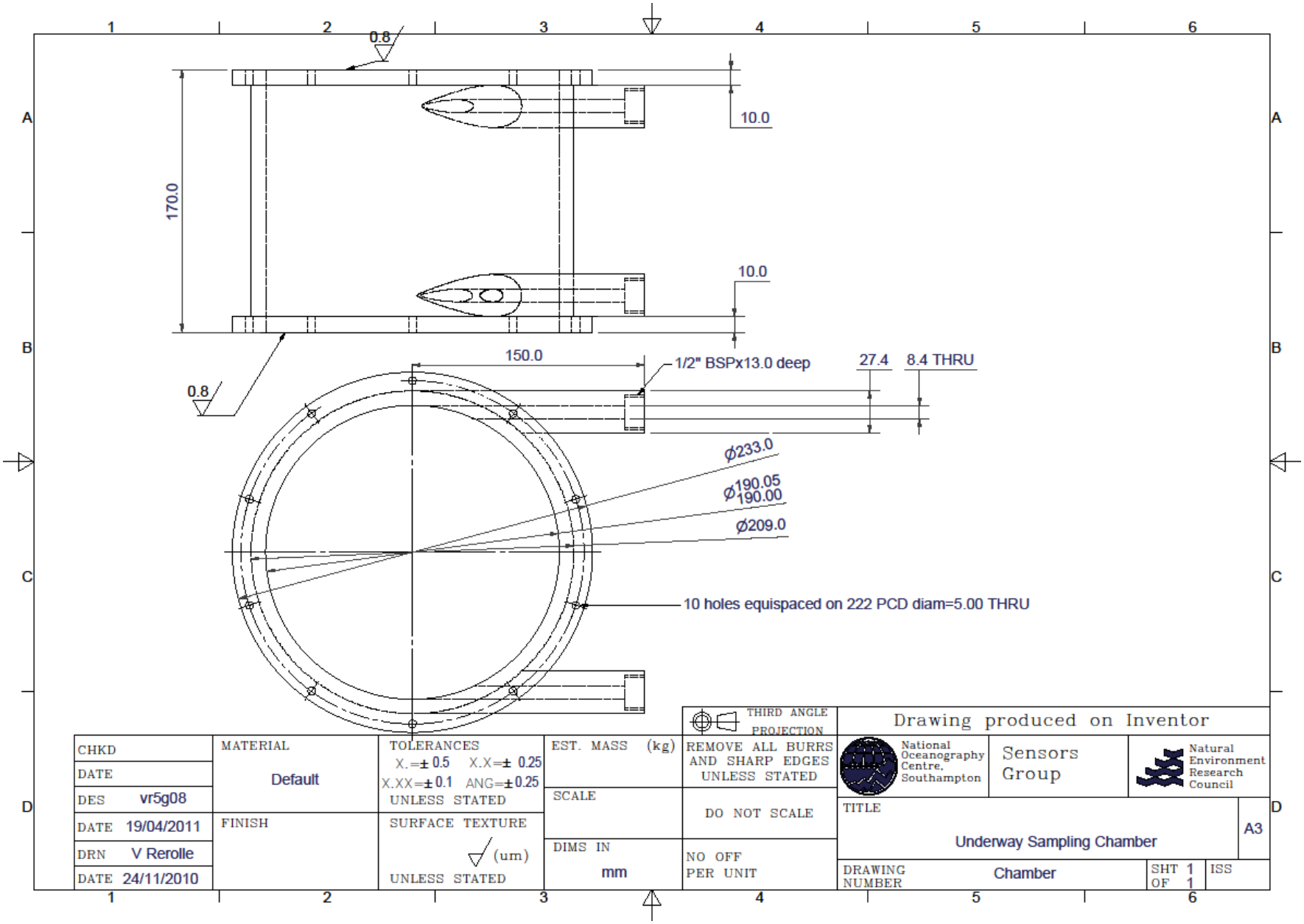

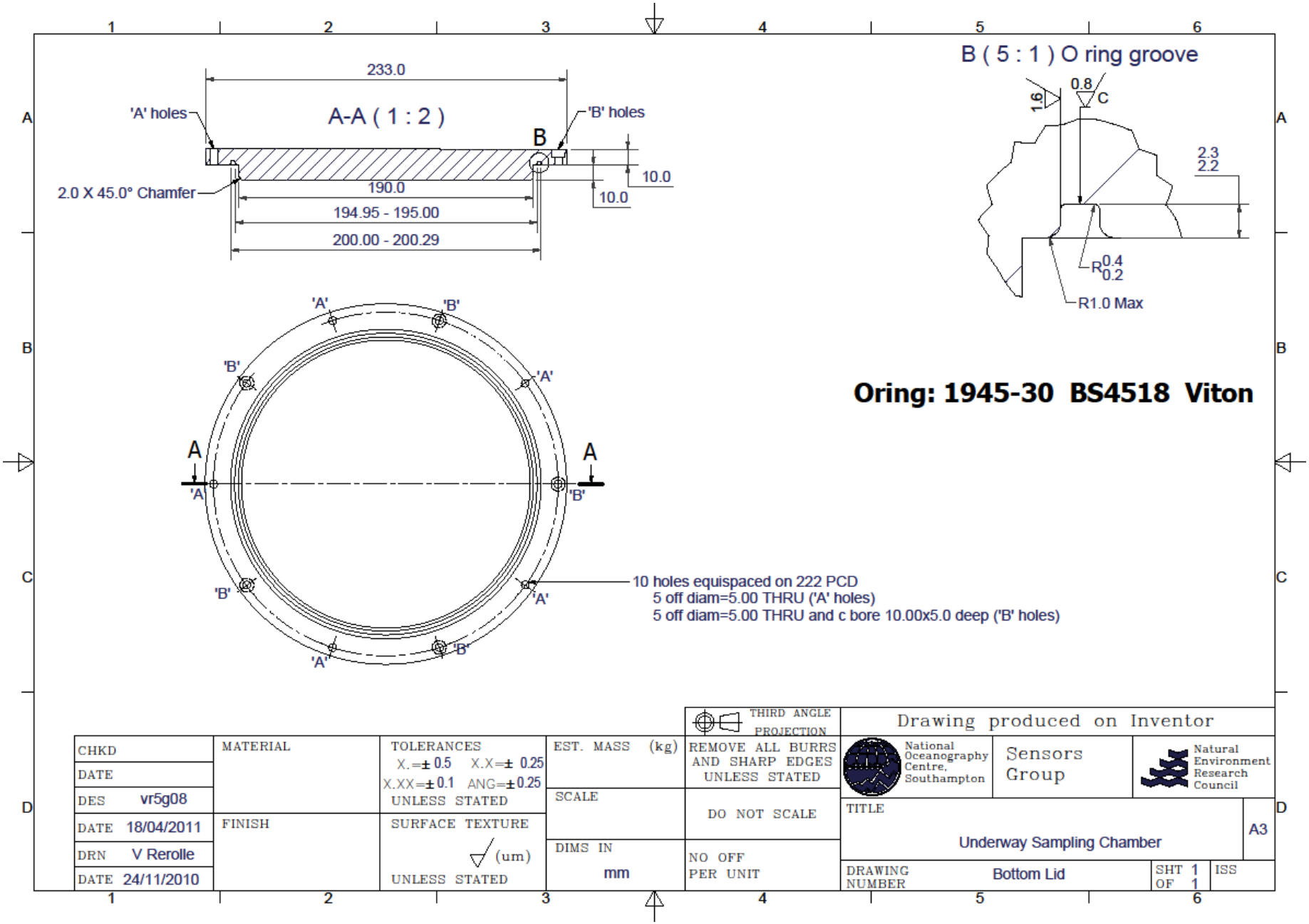
A-A (1 : 2)
233.0
'A' holes
'B' holes
B
2.0 X 45.0° Chamfer
190.0
194.95 - 195.00
200.00 - 200.29
10.0
10.0
B (5 : 1) O ring groove
0.8
C
1.6
2.3
2.2
R0.4
0.2
R1.0 Max
'A'
'B'
A
10 holes equispaced on 222 PCD
5 off diam=5.00 THRU ('A' holes)
5 off diam=5.00 THRU and c bore 10.00x5.0 deep ('B' holes)
Oring: 1945-30 BS4518 Viton
THIRD ANGLE PROJECTION
Drawing produced on Inventor
CHKD
DATE
DES vr5g08
DATE 18/04/2011
DRN V Rerolle
DATE 24/11/2010
MATERIAL
FINISH
TOLERANCES
X.=± 0.5 X.X=± 0.25
X.XX=± 0.1 ANG=± 0.25
UNLESS STATED
SURFACE TEXTURE
(um)
UNLESS STATED
EST. MASS (kg)
SCALE
DIMS IN mm
REMOVE ALL BURRS AND SHARP EDGES UNLESS STATED
DO NOT SCALE
NO OFF PER UNIT
National Oceanography Centre, Southampton
Sensors Group
Natural Environment Research Council
TITLE
Underway Sampling Chamber
A3
DRAWING NUMBER
Bottom Lid
SHT 1 OF 1
ISS

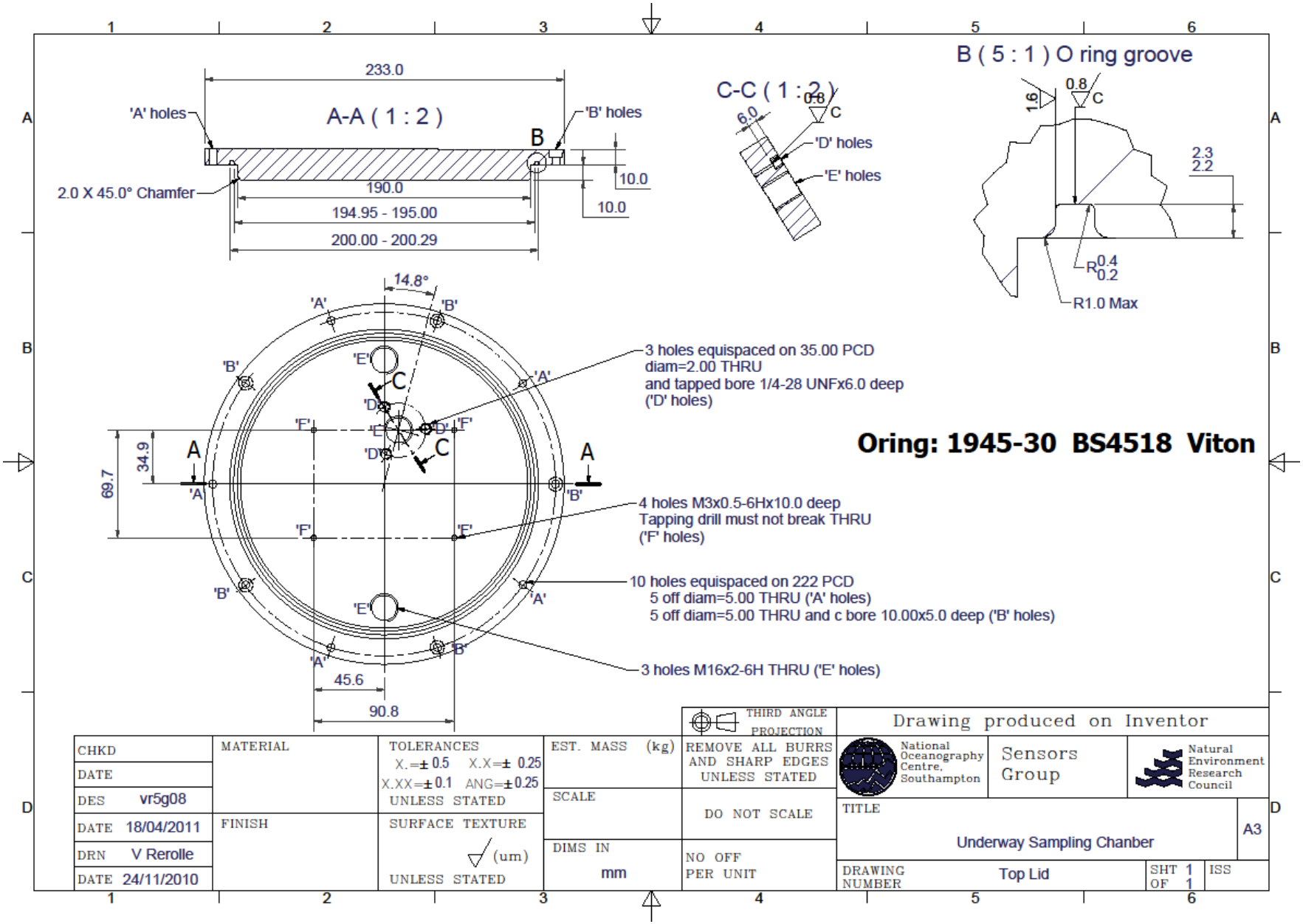
A-A (1 : 2)
233.0
'A' holes
'B' holes
2.0 X 45.0° Chamfer
190.0
194.95 - 195.00
200.00 - 200.29
10.0
10.0
C-C (1 : 2)
6.0
0.8
C
'D' holes
'E' holes
B (5 : 1) O ring groove
1.6
0.8
C
2.3
2.2
R 0.4 0.2
R1.0 Max
14.8°
3 holes equispaced on 35.00 PCD
diam=2.00 THRU
and tapped bore 1/4-28 UNFx6.0 deep
('D' holes)
Oring: 1945-30 BS4518 Viton
4 holes M3x0.5-6Hx10.0 deep
Tapping drill must not break THRU
('F' holes)
10 holes equispaced on 222 PCD
5 off diam=5.00 THRU ('A' holes)
5 off diam=5.00 THRU and c bore 10.00x5.0 deep ('B' holes)
3 holes M16x2-6H THRU ('E' holes)
34.9
69.7
45.6
90.8
THIRD ANGLE PROJECTION
Drawing produced on Inventor
CHKD
DATE
DES vr5g08
DATE 18/04/2011
DRN V Rerolle
DATE 24/11/2010
MATERIAL
FINISH
TOLERANCES
X.=± 0.5 X.X=± 0.25
X.XX=± 0.1 ANG=± 0.25
UNLESS STATED
SURFACE TEXTURE
(um)
UNLESS STATED
EST. MASS (kg)
SCALE
DIMS IN mm
REMOVE ALL BURRS AND SHARP EDGES UNLESS STATED
DO NOT SCALE
NO OFF PER UNIT
National Oceanography Centre, Southampton
Sensors Group
Natural Environment Research Council
TITLE
Underway Sampling Chanber
A3
DRAWING NUMBER
Top Lid
SHT 1 OF 1
ISS

A2b. Valves Pot

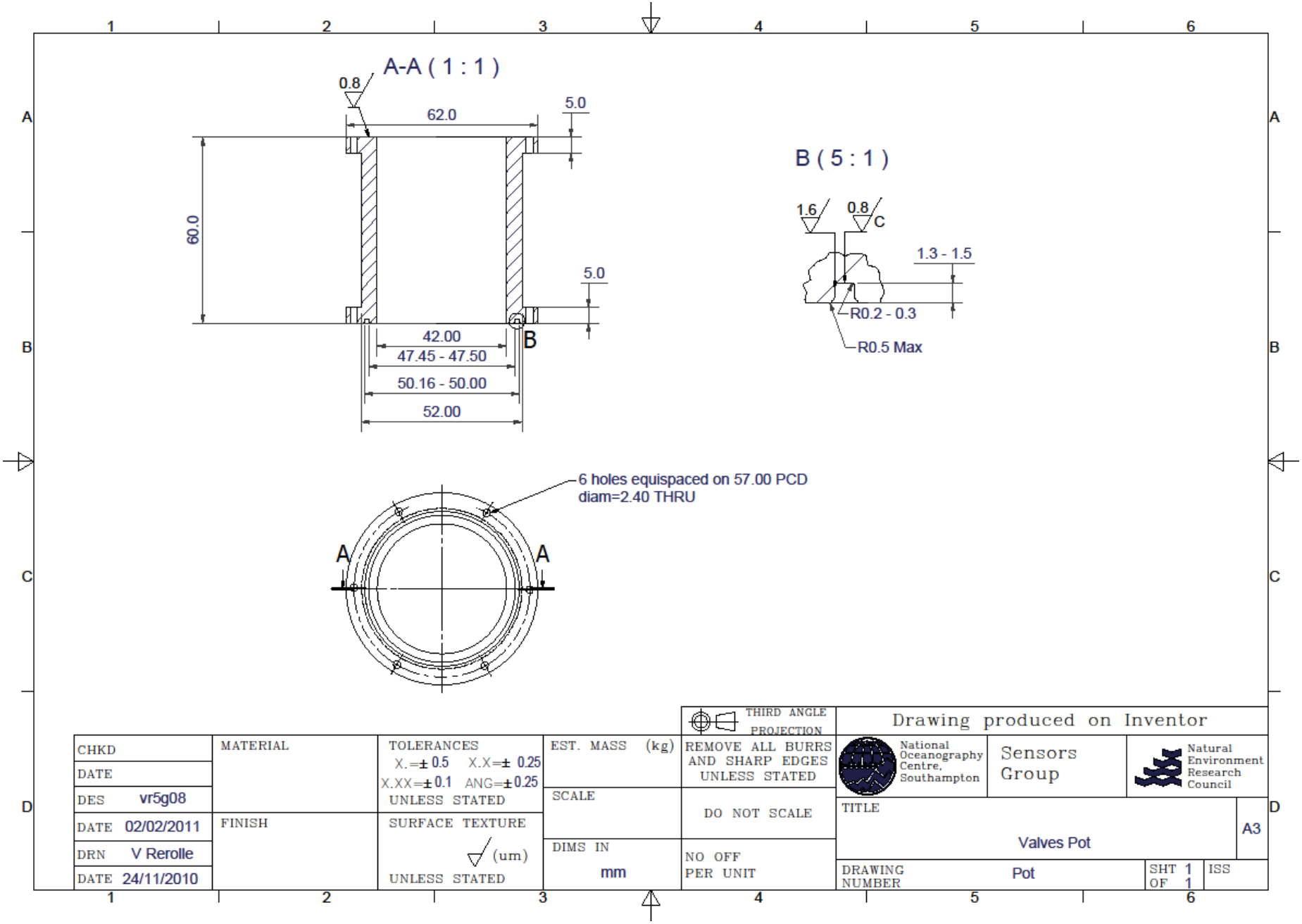

CHKD	MATERIAL	TOLERANCES X.=± 0.5 X.X=± 0.25 X.XX=± 0.1 ANG=± 0.25 UNLESS STATED	EST. MASS (kg)	THIRD ANGLE PROJECTION	Drawing produced on Inventor	
DATE				REMOVE ALL BURRS AND SHARP EDGES UNLESS STATED	National Oceanography Centre, Southampton	Sensors Group / Natural Environment Research Council
DES vr5g08			SCALE	DO NOT SCALE	TITLE: Valves Pot	A3
DATE 02/02/2011	FINISH	SURFACE TEXTURE (um)	DIMS IN mm	NO OFF PER UNIT	DRAWING NUMBER: Pot	SHT 1 OF 1 / ISS
DRN V Rerolle						
DATE 24/11/2010		UNLESS STATED				

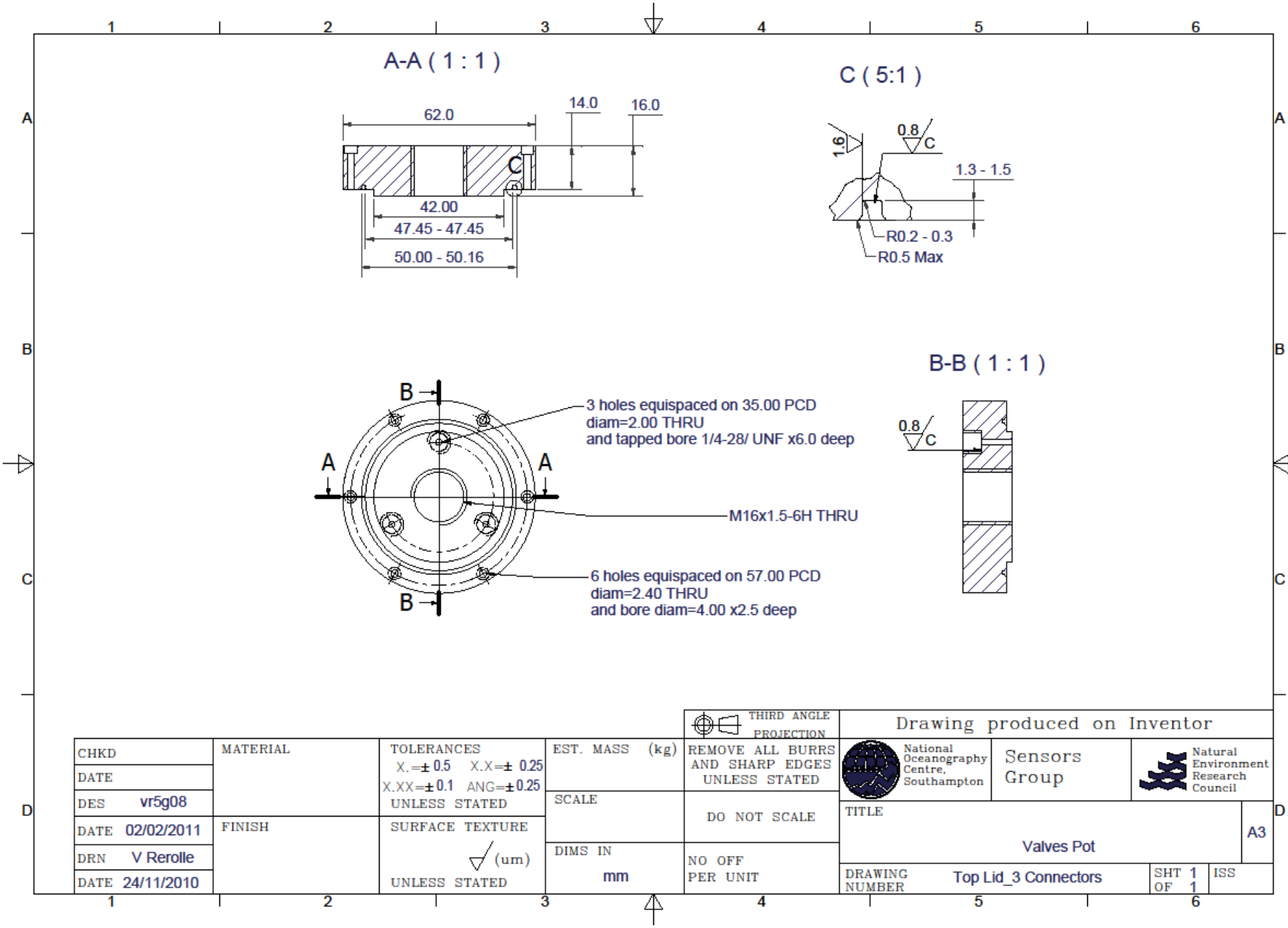
A-A (1 : 1)
62.0
14.0
16.0
C
42.00
47.45 - 47.45
50.00 - 50.16
C (5:1)
1.6
0.8
C
1.3 - 1.5
R0.2 - 0.3
R0.5 Max
B-B (1 : 1)
0.8
C
B
A
A
B
3 holes equispaced on 35.00 PCD
diam=2.00 THRU
and tapped bore 1/4-28/ UNF x6.0 deep
M16x1.5-6H THRU
6 holes equispaced on 57.00 PCD
diam=2.40 THRU
and bore diam=4.00 x2.5 deep
THIRD ANGLE PROJECTION
Drawing produced on Inventor
CHKD
DATE
DES vr5g08
DATE 02/02/2011
DRN V Rerolle
DATE 24/11/2010
MATERIAL
FINISH
TOLERANCES
X.=± 0.5 X.X=± 0.25
X.XX=± 0.1 ANG=± 0.25
UNLESS STATED
SURFACE TEXTURE
(um)
UNLESS STATED
EST. MASS (kg)
SCALE
DIMS IN
mm
REMOVE ALL BURRS AND SHARP EDGES UNLESS STATED
DO NOT SCALE
NO OFF PER UNIT
National Oceanography Centre, Southampton
Sensors Group
Natural Environment Research Council
TITLE
Valves Pot
A3
DRAWING NUMBER
Top Lid_3 Connectors
SHT 1 OF 1
ISS

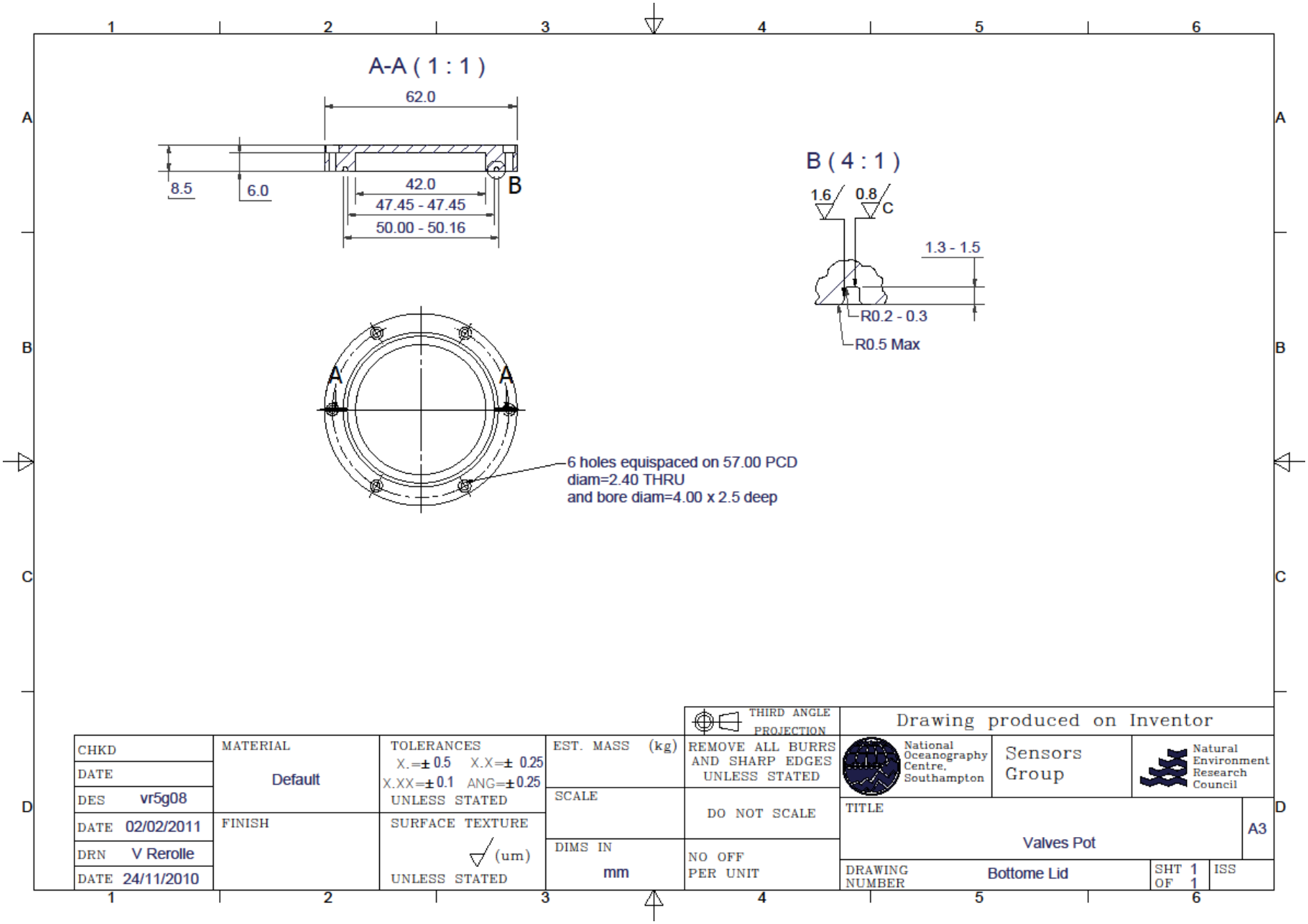
A-A (1 : 1)
62.0
8.5
6.0
42.0
47.45 - 47.45
50.00 - 50.16
B
B (4 : 1)
1.6
0.8
C
1.3 - 1.5
R0.2 - 0.3
R0.5 Max
A
A
6 holes equispaced on 57.00 PCD
diam=2.40 THRU
and bore diam=4.00 x 2.5 deep
CHKD
DATE
DES vr5g08
DATE 02/02/2011
DRN V Rerolle
DATE 24/11/2010
MATERIAL
Default
FINISH
TOLERANCES
X.=± 0.5 X.X=± 0.25
X.XX=± 0.1 ANG=± 0.25
UNLESS STATED
SURFACE TEXTURE
(um)
UNLESS STATED
EST. MASS (kg)
SCALE
DIMS IN
mm
THIRD ANGLE PROJECTION
REMOVE ALL BURRS AND SHARP EDGES UNLESS STATED
DO NOT SCALE
NO OFF PER UNIT
Drawing produced on Inventor
National Oceanography Centre, Southampton
Sensors Group
Natural Environment Research Council
TITLE
Valves Pot
A3
DRAWING NUMBER
Bottome Lid
SHT 1 OF 1
ISS

A2c. Temperature Control Chamber

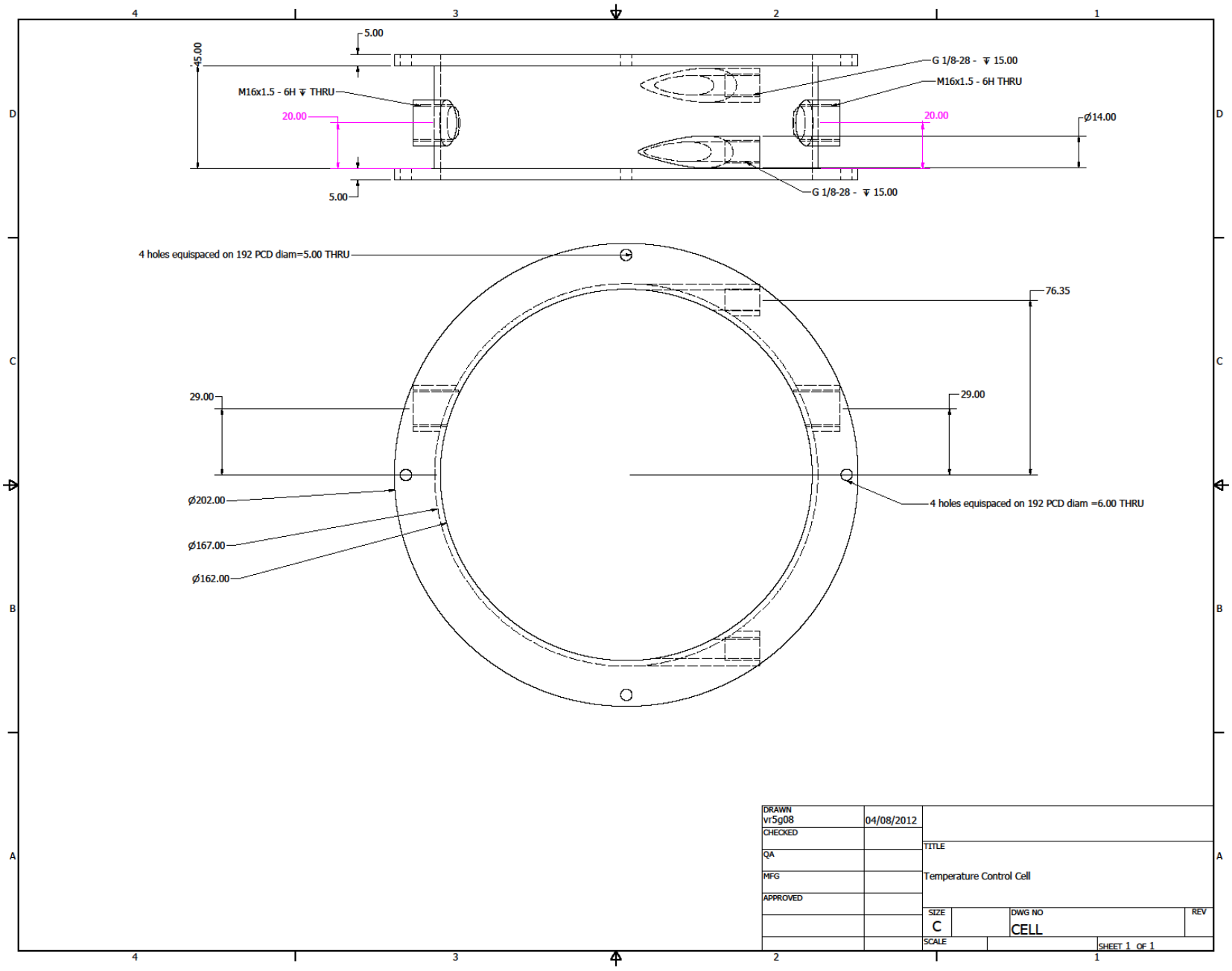

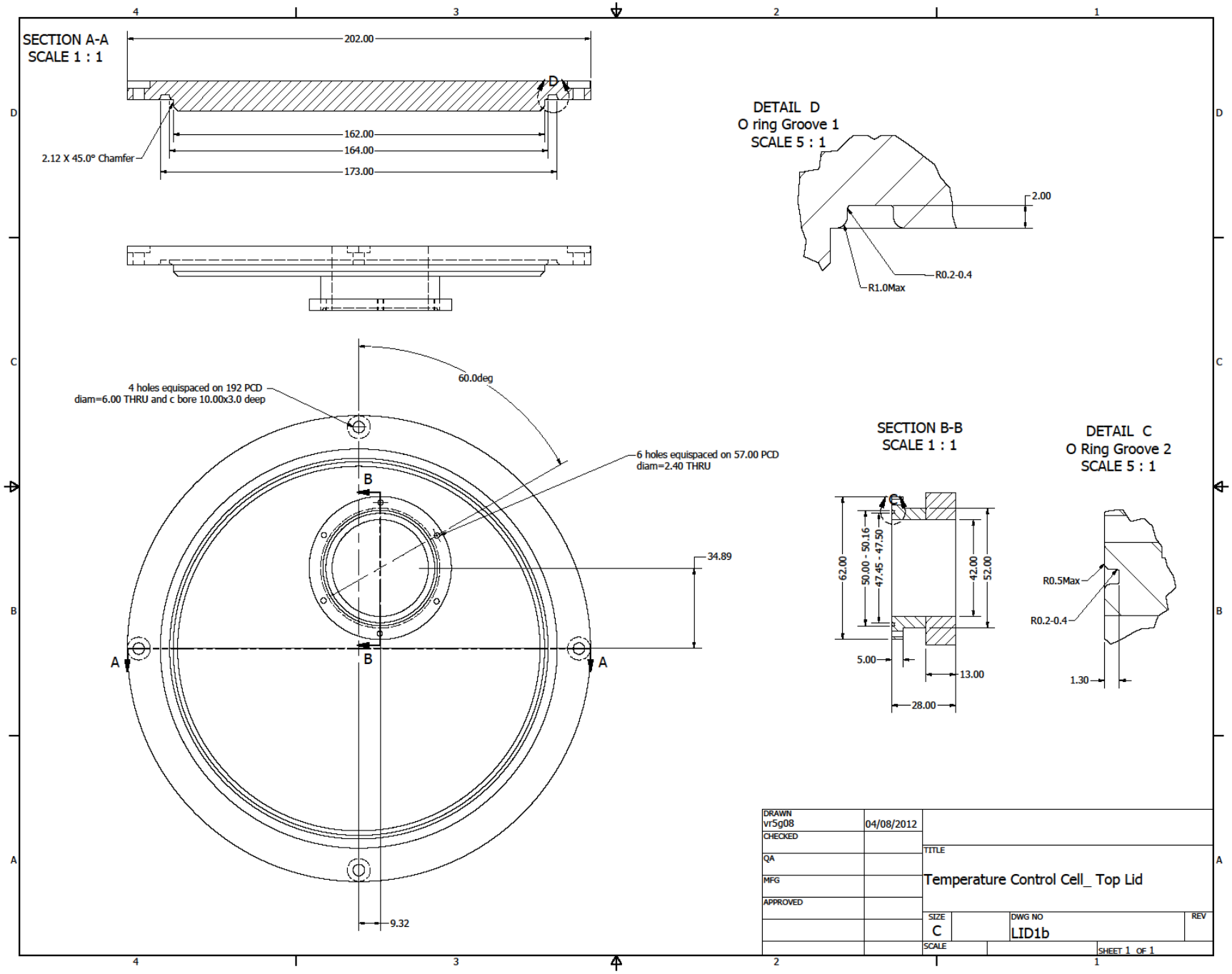
SECTION A-A
SCALE 1 : 1
202.00
D
162.00
164.00
173.00
2.12 X 45.0° Chamfer
DETAIL D
O ring Groove 1
SCALE 5 : 1
2.00
R0.2-0.4
R1.0Max
4 holes equispaced on 192 PCD
diam=6.00 THRU and c bore 10.00x3.0 deep
60.0deg
6 holes equispaced on 57.00 PCD
diam=2.40 THRU
34.89
B
A
9.32
SECTION B-B
SCALE 1 : 1
62.00
50.00 - 50.16
47.45 - 47.50
42.00
52.00
5.00
13.00
28.00
DETAIL C
O Ring Groove 2
SCALE 5 : 1
R0.5Max
R0.2-0.4
1.30
DRAWN
vr5g08
04/08/2012
CHECKED
QA
MFG
APPROVED
TITLE
Temperature Control Cell_ Top Lid
SIZE
C
DWG NO
LID1b
REV
SCALE
SHEET 1 OF 1

SECTION A-A
SCALE 1 : 1

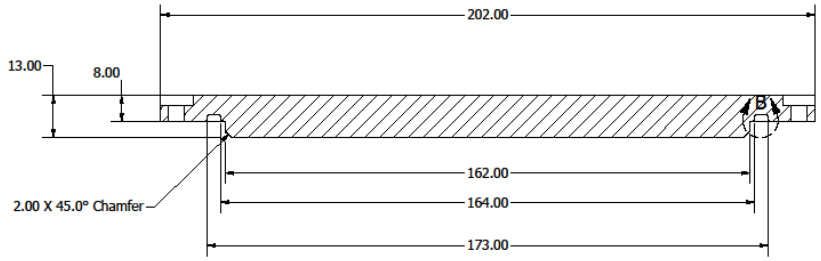

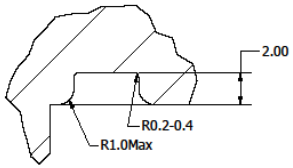

DETAIL B
SCALE 5 : 1

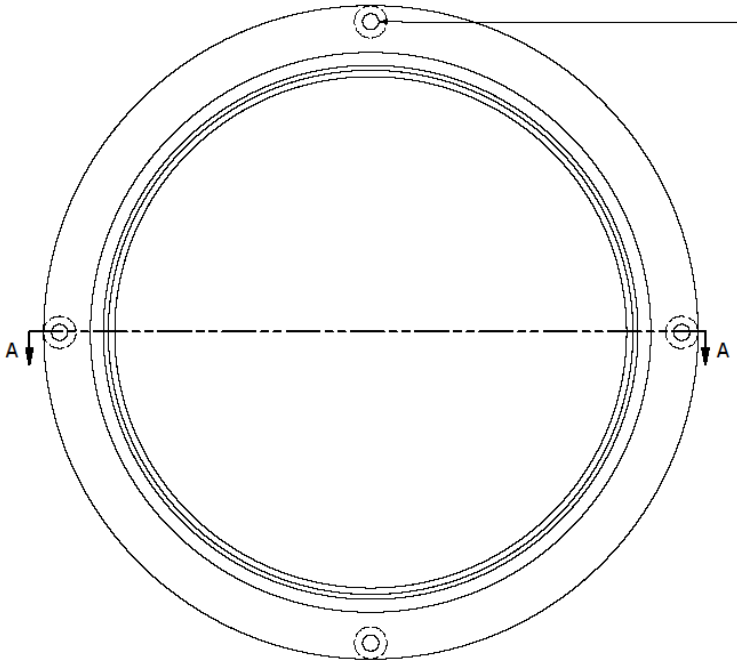

DRAWN vr5g08	04/08/2012	
CHECKED		TITLE
QA		Temperature Cell_ Bottom Lid
MFG		
APPROVED		SIZE C / DWG NO LID2 / REV
		SCALE / SHEET 1 OF 1